

博士論文

Particle-irradiation effects on  
pairing and vortex states  
in iron-based superconductors

(鉄系超伝導体の  
対状態および磁束状態に対する粒子線照射効果)

田縁 俊光

# Acknowledgement

The research work presented in this thesis involved the contribution of many people. Firstly, I would like to express my gratitude to my thesis supervisor, Prof. Tsuyoshi Tamegai, for his constant advice and guidance. Learning physics and various experimental techniques from him was a wonderful experience. I gratefully acknowledge his sharp insights, willingness for numerous discussions and also thank him for a critical reading of this thesis. I am deeply grateful to Dr. Yasuyuki Nakajima and Dr. Sunseng Pyon for their helpful advices and guidances. They also provide crystals for this work. This work has been extensively improved by their helps.

I am grateful to Dr. Leonardo Civalé for providing a chance to do an experimental work at Los Alamos National Laboratory (LANL) and for the nice hospitality at Los Alamos. It has been a pleasure learning and discussing the subject from him. I would like to thank the kind support from Dr. Oscar Ayala-Valenzuela for technical help, and from Dr. Boris Maiorov for fruitful discussion at the institute.

I am indebted to Dr. Hisashi Kitamura for his invaluable assistance in the irradiation work. I wish to acknowledge the staff of National Institute of Radiological Sciences - Heavy Ion Medical Accelerator in Chiba (NIRS-HIMAC) for their helpful cooperation. I would like to thank Dr. Satoru Okayasu for the irradiation work in Japan Atomic Energy Agency (JAEA). I would like to thank Dr. Yasuyuki Kanai and Dr. Tadashi Kambara for the kind support of the irradiation in RIKEN. I would like to thank Dr. Francesco Laviano and Prof. Gianluca Ghigo for their work in Istituto Nazionale Fisica Nucleare Laboratori Nazionali del Sud (INFN-LNS). I am grateful to Dr. Kunihiro Kihou, Dr. Shigeyuki Ishida, and Dr. Hiroshi Eisaki for providing samples and information of crystal growth. I wish to acknowledge the fruitful discussion with Prof. Hiroshi Kontani.

I gratefully acknowledge the financial support of Grant-in-Aid for Japan Society for the Promotion of Sciences (JSPS) Fellows and the support for international technological interaction by TEPCO Memorial Foundation.

I am deeply indebted to all members of Prof. Tamegai's laboratory at the University of Tokyo, Dr. Yuji Tsuchiya, Mr. Yue Sun, Mr. Hiroshi Inoue, Mr. Shinya Tada, Mr. Fumiaki Ohtake, Mr. Hiroki Akiyama, Mr. Tatsuhiro Yamada, Mr. Akinori Mine, and others, for their helpful assistances and stimulating discussions. I express my gratitude to the staffs in the school of engineering in the University of Tokyo for official and technical support.

Finally, I would have not reached this far without the constant support, love, and encouragement of my parents, sisters, and other relatives.

# Contents

<b>Acknowledgement</b>	<b>1</b>
<b>List of Tables</b>	<b>3</b>
<b>List of Figures</b>	<b>4</b>
<b>1 Introduction</b>	<b>11</b>
<b>2 Iron-based superconductors</b>	<b>14</b>
2.1 Crystal structure . . . . .	14
2.2 Electronic structure . . . . .	16
2.3 Superconducting properties . . . . .	18
2.4 Superconducting pairing mechanism . . . . .	22
2.4.1 Angle-resolved photoemission spectroscopy . . . . .	22
2.4.2 Inelastic neutron scattering . . . . .	23
2.4.3 Scanning-tunneling microscopy . . . . .	24
2.4.4 Impurity effects on the superconducting transition temperature by chemical substitution . . . . .	24
2.4.5 Summary and the motivation of our study . . . . .	28
<b>3 Vortex matter in high-temperature superconductors</b>	<b>30</b>
3.1 Vortex structure and vortex-line energy . . . . .	30
3.2 Bean's Critical state model . . . . .	31
3.3 Weak-collective pinning . . . . .	35
3.4 Sparse strong-point pinning . . . . .	40
3.5 Flux-pinning mechanism . . . . .	41
3.6 Flux creep in Anderson-Kim model . . . . .	42
3.7 Collective creep and vortex-glass theory . . . . .	43
3.8 Vortices in as-grown $\text{YBa}_2\text{Cu}_3\text{O}_{7-\delta}$ and iron-based superconductors . . . . .	45
3.9 Pinning by columnar defects and Bose-glass theory . . . . .	50
3.10 Summary and the motivation of our study . . . . .	54
<b>4 Experimental Details</b>	<b>56</b>
4.1 Single crystal growth . . . . .	56
4.2 Electron probe micro probe analyses . . . . .	58
4.3 Heavy-ion irradiation . . . . .	59
4.4 Proton irradiation and <i>in-situ</i> resistivity measurement . . . . .	60
4.5 Magnetization measurement . . . . .	60

<b>5</b>	<b>Pair-breaking effects in <math>\text{Ba}_{1-x}\text{K}_x\text{Fe}_2\text{As}_2</math></b>	<b>63</b>
5.1	Introduction . . . . .	63
5.2	Results . . . . .	65
5.2.1	Resistivity in as-grown sample . . . . .	65
5.2.2	Evolution of resistivity by proton irradiation . . . . .	66
5.2.3	The relation between $T_c$ and $\Delta\rho_0$ . . . . .	68
5.3	Discussion . . . . .	69
5.4	Summary . . . . .	73
<b>6</b>	<b>Proton irradiation effects on vortex pinning and dynamics</b>	<b>74</b>
6.1	Introduction . . . . .	74
6.2	Optimally Co-doped $\text{BaFe}_2\text{As}_2$ . . . . .	75
6.2.1	Enhancement of screening current density . . . . .	76
6.2.2	Quantitative analyses in vortex dynamics . . . . .	76
6.2.3	Summary . . . . .	82
6.3	Optimally K-doped $\text{BaFe}_2\text{As}_2$ . . . . .	82
6.3.1	Pristine $\text{Ba}_{0.6}\text{K}_{0.4}\text{Fe}_2\text{As}_2$ . . . . .	84
6.3.2	$\text{H}^+$ -irradiated $\text{Ba}_{0.6}\text{K}_{0.4}\text{Fe}_2\text{As}_2$ . . . . .	86
6.3.3	Discussion . . . . .	87
6.3.4	Summary . . . . .	92
<b>7</b>	<b>Vortex pinning and dynamics in heavy-ion irradiated <math>\text{Ba}(\text{Fe}_{1-x}\text{Co}_x)_2\text{As}_2</math></b>	<b>93</b>
7.1	Introduction . . . . .	93
7.2	Screening current density and vortex dynamics under $H  \text{CDs}$ . . . . .	94
7.2.1	200-MeV Au irradiation . . . . .	94
7.2.2	2-GeV Au irradiation . . . . .	95
7.2.3	Discussion . . . . .	96
7.3	Lock-in phenomena in $\text{Ba}(\text{Fe}_{0.93}\text{Co}_{0.07})_2\text{As}_2$ . . . . .	98
7.3.1	The orientation of irreversible magnetization . . . . .	99
7.3.2	The modulus of irreversible magnetization . . . . .	100
7.3.3	Lock-in transition . . . . .	100
7.3.4	Conclusion . . . . .	104
<b>8</b>	<b>Summary and Conclusions</b>	<b>105</b>
	<b>List of Publications</b>	<b>107</b>
	<b>References</b>	<b>112</b>



# List of Tables

3.1	Parameters used to model the temperature dependence of $J_c(T)$ and $S(T) = d \ln M / d \ln(t)$ . (Source of table: [1]) . . . . .	50
6.1	Parameters obtained from extended Maley's method and inverse of plateau value in $S(T)$ . . . . .	79

# List of Figures

2.1	(a) The schematic view of the crystal structure for several kinds of IBSs. (b) The common structure of FeAs plane and its spin structure. (Source of figure: [2])	15
2.2	$T_c$ as a function of the bond angle $\alpha$ in As-Fe-As (so-called Lee plot). The vertical lines indicates the angle of $\alpha = 109.47^\circ$ at the regular tetrahedron of FeAs <sub>4</sub> . (Source of figure: [3])	15
2.3	Valence-band photoemission spectra in IBSs of LaFeAsO <sub>1-x</sub> F <sub>x</sub> ( $x = 0, 0.06$ ) and LaFePO <sub>0.94</sub> F <sub>0.06</sub> and their comparison with band-structure calculation. Vertical bars mark main features observed in the spectra. The inset presents the near- $E_F$ spectra. (Source of figure: [4])	16
2.4	The FSs in (a) electron-doped BaFe <sub>2</sub> As <sub>2</sub> and (b) hole-doped BaFe <sub>2</sub> As <sub>2</sub> , calculated by the density-functional theory. (Source of figure: [5])	17
2.5	A comparison of the pairing state from spin-fluctuation exchange in (a) cuprates and (b) IBSs. (Source of figure: [6])	17
2.6	Temperature dependence of resistivity with several doping levels from $x = 0$ to $x = x_{\text{opt}}$ in (a) Ba(Fe <sub>1-x</sub> Co <sub>x</sub> ) <sub>2</sub> As <sub>2</sub> , (b) BaFe <sub>2</sub> (As <sub>1-x</sub> P <sub>x</sub> ) <sub>2</sub> , and (c) Ba <sub>1-x</sub> K <sub>x</sub> Fe <sub>2</sub> As <sub>2</sub> . For Co-doped and P-doped systems, the samples were annealed with BaAs. (Source of figure: [7])	18
2.7	Temperature dependence of resistivity with several doping levels from $x = 0$ to $x = x_{\text{opt}}$ in (a) Ba(Fe <sub>1-x</sub> Co <sub>x</sub> ) <sub>2</sub> As <sub>2</sub> , (b) BaFe <sub>2</sub> (As <sub>1-x</sub> P <sub>x</sub> ) <sub>2</sub> , and (c) Ba <sub>1-x</sub> K <sub>x</sub> Fe <sub>2</sub> As <sub>2</sub> . For Co-doped and P-doped systems, the samples were annealed with BaAs. (Source of figure: [7])	19
2.8	Upper critical field $H_{c2}$ under applied field perpendicular and parallel to the FeAs plane. The anisotropy parameter $\gamma = H_{c2}^\perp/H_{c2}^\parallel$ is shown in lower inset. (Source of figure: [8])	20
2.9	The temperature dependence of the superfluid density in Ba <sub>0.45</sub> K <sub>0.55</sub> Fe <sub>2</sub> As <sub>2</sub> . The flat region at low temperature indicates the fully-opened superconducting gap. Inset: The exponential behavior of $\delta\lambda_{ab}(T)/\lambda_{ab}(0)$ at low temperature. $T$ -linear dependence expected in clean $d$ -wave superconductors are also represented by the broken line. (Source of figure: [9])	21
2.10	The normalized-field dependence of the electronic thermal conductivity at low temperature limit in doped BaFe <sub>2</sub> As <sub>2</sub> . The behavior expected in fully-gapped superconductors is observed in (a), while the presence of line node is suggested in (b). (Source of figure: [2])	21
2.11	Electronic phase diagram in electron-doping Ba(Fe <sub>1-x</sub> Co <sub>x</sub> ) <sub>2</sub> As <sub>2</sub> , isovalent doping BaFe <sub>2</sub> (As <sub>1-x</sub> P <sub>x</sub> ) <sub>2</sub> , and hole-doping (Ba <sub>1-x</sub> K <sub>x</sub> )Fe <sub>2</sub> As <sub>2</sub> . (Source of figure: [10])	21

2.12	The angular dependence of the superconducting gap in each FS determined by the laser-ARPES measurement in $\text{BaFe}_2(\text{As}_{0.65}\text{P}_{0.35})_2$ . Inset: the definition of the angle $\theta$ in FS. (Source of figure: [11]) . . . . .	23
2.13	The angular dependence of the superconducting gap in each FS determined by the laser-ARPES measurement in $\text{Ba}_{0.6}\text{K}_{0.4}\text{Fe}_2\text{As}_2$ . Inset: the definition of the angle $\theta$ in FS. (Source of figure: [11]) . . . . .	23
2.14	The imaginary part of the spin susceptibility in $\text{Ba}(\text{Fe}_{0.925}\text{Co}_{0.075})_2\text{As}_2$ at the superconducting state ( $T = 4$ K) and the normal state ( $T = 60, 280$ K). (Source of figure: [12]) . . . . .	24
2.15	The calculated imaginary part of the spin susceptibility in the $s_{+-}$ -wave superconducting state (blue line) and the normal state (red broken line). (Source of figure: [13]) . . . . .	24
2.16	The magnetic-field induced change in QPI intensities. $\mathbf{q}_2 = (\pi, 0)$ and $\mathbf{q}_2 = (\pi, 0)$ are the $\mathbf{q}$ vector connecting hole-electron FSs and hole-hole FSs, respectively. (Source of figure: [14]) . . . . .	25
2.17	The robustness of $T_c$ with an introduction of nonmagnetic impurities in the case of $s_{\pm}$ -wave state and $s_{++}$ -wave state. (Source of figure: [15]) . . . . .	26
2.18	The temperature dependence of $\rho$ in $\text{Ba}_{0.5}\text{K}_{0.5}\text{Fe}_{2-2x}\text{M}_{2x}\text{As}_2$ ( $M = \text{Mn, Ru, Co, Ni, Cu, and Zn}$ ). (Source of figure: [16]) . . . . .	26
2.19	The suppression of $T_c$ as a function of the residual resistivity $\rho_0$ in chemically substituted $\text{Ba}_{0.5}\text{K}_{0.5}\text{Fe}_{2-2x}\text{M}_{2x}\text{As}_2$ ( $M = \text{Mn, Ru, Co, Ni, Cu, and Zn}$ ). (Source of figure: [16]) . . . . .	26
2.20	The temperature dependence of resistivity in single crystal of $\text{YBa}_2\text{Cu}_3\text{O}_{7-\delta}$ with 2.5-MeV electron irradiation. (Source of figure: [17]) . . . . .	27
2.21	The decrease of $T_c$ as a function of the resistivity just above $T_c$ , $\rho(T_c)$ . (Source of figure: [17]) . . . . .	27
2.22	The temperature dependence of resistivity in single crystal of $\text{Ba}(\text{Fe}_{1-x}\text{Co}_x)_2\text{As}_2$ with 3-MeV proton irradiation. (Source of figure: [18]) . . . . .	28
2.23	The reduced temperature $T_c/T_{c0}$ as a function of the normalized relaxation rate $g$ in 3-MeV proton irradiated $\text{Ba}(\text{Fe}_{1-x}\text{Co}_x)_2\text{As}_2$ single crystals. $g_c$ is the critical value of $g$ for $s_{\pm}$ -wave state. (Source of figure: [18]) . . . . .	28
3.1	The structure of isolated vortex in a superconductor with $\kappa \approx 8$ . The superconducting order parameter $\Psi$ is suppressed at the vortex core $r \approx 0$ , and the local magnetic field $h$ is screened outside the core $r \rightarrow 0$ . (Source of figure: [19]) . . .	31
3.2	(a) The magnetic induction profile $B(x)$ under the relatively small applied field $H(< H_{\text{sf}})$ . Outside the sample, $B = H$ , while inside the sample a straight lines with $dB/dx = 0$ or a constant slope. Subsequent increase in $H$ produces the profile of $B(x)$ under (b) $H = H_{\text{sf}} = 4\pi J_c d/c$ and (c) $H > H_{\text{sf}}$ . The field sweeping after reaching to (c) produces $B(x)$ of (e) under zero field (the remanent state) via the state of (d). (f) The relation among the average $\bar{B}$ , $H$ , and $4\pi M$ . .	32
3.3	The hysteresis loop of a dirty superconductor according to the Bean's model. (Source of figure: [20]) . . . . .	34
3.4	The rooftop pattern of $B$ in three-dimensional Bean's model. The volume of the rooftop pattern is related to $M$ . . . . .	35

3.5	The field dependence of the critical current density $J_c$ in the framework of the weak-collective pinning theory. For low field, the interaction between the vortices is irrelevant and $j_c$ does not depend on the magnetic field. Within the small-bundle pinning regime, the critical current density decreases exponentially. Finally, in the large-bundle pinning regime, the field dependence of $j_c$ turns algebraic, with $j_c \propto B^{-3}$ . (Source of figure: [21]) . . . . .	41
3.6	Magnetic hysteresis loops in $\text{YBa}_2\text{Cu}_3\text{O}_{7-\delta}$ at several temperatures. (Source of figure: [22]) . . . . .	46
3.7	Field dependence of the persistent current density at several temperatures obtained from magnetization loops with the help of Bean's critical state model. Inset: the temperature dependence of the persistent current density at $H = 3$ T. (Source of figure: [23]) . . . . .	46
3.8	The field dependence of the critical current density at $T = 75$ K in $\text{YBa}_2\text{Cu}_3\text{O}_{7-\delta}$ . (Source of figure: [22]) . . . . .	47
3.9	Field dependence of (a) the screening current density $J$ , (b) the relaxation rate $S$ , and (c) the glassy exponent $\mu$ at $T = 40$ K in $\text{YBa}_2\text{Cu}_3\text{O}_{7-\delta}$ . (Source of figure: [23]) . . . . .	48
3.10	The vortex-bundle regime in each $H$ and $J$ region. (Source of figure: [23]) . . . .	48
3.11	The temperature dependence of the screening current density $J$ at $H = 1$ T in $\text{YBa}_2\text{Cu}_3\text{O}_{7-\delta}$ . The open and closed symbols are before and after proton irradiation with a dose of $1 \times 10^{16}$ ions/cm <sup>2</sup> . Lines are fits to Eq. (3.71). (Source of figure: [1]) . . . . .	49
3.12	The temperature dependence of the normalized relaxation rate $S$ at $H = 1$ T in $\text{YBa}_2\text{Cu}_3\text{O}_{7-\delta}$ . The open and closed symbols are before and after proton irradiation with a dose of $1 \times 10^{16}$ ions/cm <sup>2</sup> . Lines are fits to Eq. (3.72). (Source of figure: [1]) . . . . .	49
3.13	Maley's plot under $H = 1$ T parallel to $c$ -axis in $\text{YBa}_2\text{Cu}_3\text{O}_{7-\delta}$ . (Source of figure: [1]) . . . . .	49
3.14	The vortex phase diagram in $\text{Ba}(\text{Fe}_{0.92}\text{Co}_{0.08})_2\text{As}_2$ determined by the vortex creep measurement. (Source of figure: [24]) . . . . .	51
3.15	The temperature dependence of the screening current density $J$ under several magnetic fields in 1-GeV Au-irradiated $\text{YBa}_2\text{Cu}_3\text{O}_{7-\delta}$ with a matching field $B_\phi = 2.4$ T. Inset: the derivation $d \ln J/dT$ as a function of temperature. The arrows are correspondent to the drop in $J(T)$ . (Source of figure: [25]) . . . . .	53
3.16	The temperature dependence of the normalized relaxation rate $S$ under several magnetic fields in 1-GeV Au-irradiated $\text{YBa}_2\text{Cu}_3\text{O}_{7-\delta}$ with a matching field $B_\phi = 2.4$ T. The peak temperature in $S(T)$ coincides with the temperature of the drop in $J(T)$ . (Source of figure: [25]) . . . . .	53
3.17	The vortex phase diagram in 1-GeV Au-irradiated $\text{YBa}_2\text{Cu}_3\text{O}_{7-\delta}$ with a matching field $B_\phi = 2.4$ T. Inset: the similar plot in different matching fields of $B_\phi = 1.1$ T and 4.7 T. (Source of figure: [25]) . . . . .	54
3.18	Angular dependence of the magnetization in 309-MeV Au-irradiated $\text{YBa}_2\text{Cu}_3\text{O}_{7-\delta}$ with a matching field $B_\phi = 1$ T. The CDs are introduced with an angle of $30^\circ$ from $c$ -axis. The plateau feature is observed around field parallel to CDs. (Source of figure: [26]) . . . . .	55

3.19	The plateau width $2\varphi_L$ as a function of $1/H$ in 309-MeV Au-irradiated $\text{YBa}_2\text{Cu}_3\text{O}_{7-\delta}$ with a matching field $B_\phi = 1$ T. The CDs are introduced with an angle of $30^\circ$ from $c$ -axis. The solid lines are the linear fit to each data of the fixed temperature. (Source of figure: [26]) . . . . .	55
4.1	(a) The schematic view of the assembly for Co-doped $\text{BaFe}_2\text{As}_2$ single crystal growth. (b) The heating procedure in $\text{Ba}(\text{Fe}_{1-x}\text{Co}_x)_2\text{As}_2$ single-crystal growth. .	57
4.2	(a) The schematic view of the assembly for K-doped $\text{BaFe}_2\text{As}_2$ single crystal growth. (b) The heating procedure in $\text{Ba}_{1-x}\text{K}_x\text{Fe}_2\text{As}_2$ single-crystal growth for $x = 0.23$ and $0.42$ . . . . .	59
4.3	The obtained single crystals of $\text{Ba}_{0.58}\text{K}_{0.42}\text{Fe}_2\text{As}_2$ . The scale is mm. The mirror surface is $ab$ -plane. . . . .	59
4.4	The heating procedure in $\text{Ba}_{0.31}\text{K}_{0.69}\text{Fe}_2\text{As}_2$ single crystal growth. . . . .	59
4.5	The schematic view of the sample holder the overall system for proton irradiation. .	61
5.1	(a) Temperature dependence of the resistivity in $\text{Ba}_{1-x}\text{K}_x\text{Fe}_2\text{As}_2$ ( $x = 0.23, 0.42$ , and $0.69$ ). Inset: the resistivity as a function of $T^2$ . (b) Temperature dependence of zero-field-cooled (ZFC) and field-cooled (FC) Meissner signal under $H = 5$ Oe in $\text{Ba}_{1-x}\text{K}_x\text{Fe}_2\text{As}_2$ ( $x = 0.23, 0.42$ , and $0.69$ ). . . . .	65
5.2	Temperature dependence of the resistivity in $\text{Ba}_{1-x}\text{K}_x\text{Fe}_2\text{As}_2$ ( $x = 0.23, 0.42$ , and $0.69$ ) with doses of $0, 0.52, 1.0, 1.6, 2.1, 3.1, 4.8, 6.8$ , and $9.2 \times 10^{16}$ ions/cm <sup>2</sup> . Broken lines represent fitting lines of $\rho = \rho_0 + AT^2$ . . . . .	67
5.3	Dose dependence of (a) $\Delta\rho_0 \equiv \rho_0^i - \rho_0^0$ and (b) $T_c$ in $\text{Ba}_{1-x}\text{K}_x\text{Fe}_2\text{As}_2$ ( $x = 0.23, 0.42$ , and $0.69$ ). (c) The definition of $T_c$ and $T_c^{\text{onset}}$ . Dashed lines are the linear fit above and in the middle of the resistive transition. . . . .	68
5.4	(a) A magneto-optical image at $33$ K under $H = 5$ Oe taken after removing silver paste and gold wire from the crystal of $\text{Ba}_{0.6}\text{K}_{0.4}\text{Fe}_2\text{As}_2$ shown in panel (b). . . .	69
5.5	$T_c$ as a function of $\Delta\rho_0$ in $\text{Ba}_{1-x}\text{K}_x\text{Fe}_2\text{As}_2$ ( $x = 0.23, 0.42$ , and $0.69$ ). Inset: The vertical axis is changed to $T_c/T_{c0}$ . . . . .	70
5.6	$T_c/T_{c0}$ as a function of a normalized scattering rate $g = \hbar/2\pi k_B T_{c0} \tau$ in $\text{Ba}_{1-x}\text{K}_x\text{Fe}_2\text{As}_2$ ( $x = 0.23, 0.42$ , and $0.69$ ) evaluated by (a) the five-orbital model $g^{\text{5orb}} = 0.88z\Delta\rho_0/T_{c0}$ and (b) the London penetration depth $g^\lambda = \hbar\Delta\rho_0/\pi k_B T_{c0} \mu_0 \lambda^2$ . These data are linearly extrapolated to obtain critical values of $g$ as shown by dotted lines. Dashed lines indicate the critical scattering rate $g_c^\pm \simeq 0.3$ by simple estimation for $s_\pm$ -wave scenario. . . . .	71
6.1	Field dependence of $J_s$ in (a) pristine and (b) $\text{H}^+$ irradiated $\text{Ba}(\text{Fe}_{0.93}\text{Co}_{0.07})_2\text{As}_2$ at several temperatures. Dotted line on $\bullet$ ( $2$ K) shows power-law decay of (a) $H^{-0.5}$ and (b) $H^{-0.3}$ , respectively. Vertical line indicates the field where we discuss the vortex dynamics, $H = 5$ kOe. . . . .	77
6.2	Inverse current-density dependence of effective pinning energy $U^*$ in (a) pristine and (b) $\text{H}^+$ irradiated $\text{Ba}(\text{Fe}_{0.93}\text{Co}_{0.07})_2\text{As}_2$ . Inset: Temperature dependence of normalized relaxation rate $S$ . Solid line indicates fitting by Eq. (3.72). . . . .	78
6.3	Current density ( $J$ ) dependence of the vortex pinning energy ( $U$ ) in (a) pristine and (b) $\text{H}^+$ -irradiated $\text{Ba}(\text{Fe}_{0.93}\text{Co}_{0.07})_2\text{As}_2$ constructed by extended Maley's method. Solid line indicates power-law fitting in large $J$ region. . . . .	80

6.4	Temperature dependence of $J_s$ ( $\bullet$ ), model function of $J_c$ before and after creep with the parameters in Table 6.1(solid line), $\delta T_c$ - and $\delta l$ -pinning (dashed line) and $J_c$ reconstructed by GIS (+) in (a)pristine and (b) $H^+$ -irradiated $\text{Ba}(\text{Fe}_{0.93}\text{Co}_{0.07})_2\text{As}_2$ .	81
6.5	Temperature dependence of the magnetization under $H = 5$ Oe along $c$ -axis in pristine and $H^+$ -irradiated $\text{Ba}_{0.6}\text{K}_{0.4}\text{Fe}_2\text{As}_2$ .	84
6.6	Magnetization loops under $H  c$ in pristine $\text{Ba}_{0.6}\text{K}_{0.4}\text{Fe}_2\text{As}_2$ at several temperature.	84
6.7	(a) Field dependence of in-plane screening current density $J$ under $H  c$ at several temperature and (b) the normalized relaxation rate $S$ at 5, 10, and 15 K under $H  c$ in pristine $\text{Ba}_{0.6}\text{K}_{0.4}\text{Fe}_2\text{As}_2$ .	85
6.8	(a) Temperature dependence of in-plane screening current density $J$ at $H = 0$ , 10, 20, and 30 kOe and (b) the normalized relaxation rate $S$ at $H = 10$ , 20, and 30 kOe under $H  c$ in pristine $\text{Ba}_{0.6}\text{K}_{0.4}\text{Fe}_2\text{As}_2$ .	85
6.9	Magnetization loops under $H  c$ in $H^+$ -irradiated $\text{Ba}_{0.6}\text{K}_{0.4}\text{Fe}_2\text{As}_2$ at several temperature.	88
6.10	(a) Field dependence of in-plane screening current density $J$ under $H  c$ at several temperature and (b) the normalized relaxation rate $S$ at 5, 10, and 25 K under $H  c$ in $H^+$ -irradiated $\text{Ba}_{0.6}\text{K}_{0.4}\text{Fe}_2\text{As}_2$ .	89
6.11	(a) Temperature dependence of in-plane screening current density $J$ at $H = 0$ , 10, 20, and 30 kOe and (b) the normalized relaxation rate $S$ at $H = 10$ , 20, and 30 kOe under $H  c$ in $H^+$ -irradiated $\text{Ba}_{0.6}\text{K}_{0.4}\text{Fe}_2\text{As}_2$ .	89
6.12	(a) A log-log plot of Fig. 6.7(a) and (b) that of Fig. 6.10(a). The broken lines indicates $J \propto H^{-\alpha}$ with (a) $\alpha = 1/2$ and (b) $\alpha = 1/3$ .	90
7.1	Field dependence of screening current $J_s$ at several temperatures in 200-MeV Au-irradiated $\text{Ba}(\text{Fe}_{0.93}\text{Co}_{0.07})_2\text{As}_2$ .	95
7.2	Field dependence of the normalized relaxation rate $S$ at $T = 5$ K and $0 \leq H \leq 30$ kOe in 200-MeV Au-irradiated $\text{Ba}(\text{Fe}_{0.93}\text{Co}_{0.07})_2\text{As}_2$ with $B_\phi = 0$ (unirradiated), 10, and 20 kG.	95
7.3	Temperature dependence of screening current $J_s$ at several $H = 2, 4, 10$ , and 15 kOe in 200-MeV Au irradiated $\text{Ba}(\text{Fe}_{0.93}\text{Co}_{0.07})_2\text{As}_2$ .	95
7.4	Temperature dependence of the normalized relaxation rate $S$ at $H = 0, 2, 4$ , and 10 kOe in 200-MeV Au irradiated $\text{Ba}(\text{Fe}_{0.93}\text{Co}_{0.07})_2\text{As}_2$ .	95
7.5	Field dependence of screening current $J_s$ at several temperatures in 2-GeV Au irradiated $\text{Ba}(\text{Fe}_{0.93}\text{Co}_{0.07})_2\text{As}_2$ .	96
7.6	Field dependence of the normalized relaxation rate $S$ at $T = 2, 5$ , and 15 Ks in 2-GeV Au irradiated $\text{Ba}(\text{Fe}_{0.93}\text{Co}_{0.07})_2\text{As}_2$ .	96
7.7	Temperature dependence of screening current $J_s$ at several $H = 2, 4, 10$ , and 15 kOe in 2-GeV Au irradiated $\text{Ba}(\text{Fe}_{0.93}\text{Co}_{0.07})_2\text{As}_2$ .	97
7.8	Temperature dependence of the normalized relaxation rate $S$ at $H = 0, 2, 4$ , and 10 kOe in 2-GeV Au irradiated $\text{Ba}(\text{Fe}_{0.93}\text{Co}_{0.07})_2\text{As}_2$ .	97
7.9	(a) Longitudinal and transverse magnetization curves $4\pi M_l$ and $4\pi M_t$ at 5 K, $\theta = 45^\circ$ . (b) $\theta$ dependence of $\alpha$ between irreversible magnetization vector $\mathbf{M}_{\text{irr}}$ and the sample normal $\tilde{n}$ . Solid line indicates the fit to $\alpha(\theta)$ according to Ref. [27]. Inset: definition of angles of $\theta$ and $\alpha$ .	99
7.10	Field dependence of (a) $4\pi M_{l,\text{irr}}$ , (b) $4\pi M_{t,\text{irr}}$ , and (c) $4\pi M_{\text{irr}}$ at each angle.	101

7.11	(a) $\theta$ dependence of $4\pi M_{\text{irr}}$ at each field. All points are taken from Fig. 7.10(c).	
	(b) Blow-up of (a) around $\theta = 0^\circ$ at selected field. Broken lines are guides to the eye for the lock-in transition. . . . .	103
7.12	Inverse-field dependence of lock-in angle $\theta_L$ , defined by a half of the width of the plateau in Fig. 7.11. Broken line is the linear fit according to Eq. (7.1). . . . .	103

# Chapter 1

## Introduction

The discovery of iron-based superconductors (IBSs) [28] demonstrates that cuprate superconductors are not the only high-temperature superconductors, and opens the door to develop new high-temperature superconducting materials. In the IBS system, there are many kinds of materials, and even now, new IBS compounds are being discovered one after another. Although the superconducting transition temperature  $T_c$  does not exceed liquid nitrogen temperature 77 K as in the case of cuprates, the highest  $T_c$  of 55 K is recorded just a few months after the discovery [29], which made us interested in IBSs from scientific and engineering points of view. All compounds belonging to IBSs have an alternating stacking structure of conducting FeAs layers and blocking layers. It is also common in IBSs that the Fermi surfaces (FSs) are mainly composed of Fe 3*d* electrons. In addition, we point out that most of the superconductivity appear accompanied by the suppression of anti-ferromagnetic (AF) order and structural transition with doping to parent compound. Among many types of compounds, BaFe<sub>2</sub>As<sub>2</sub> (so-called "122") system [30] is the most notable since very large single crystals are readily available. This is why this system has been the platform for fundamental studies. It is noted that, in 122 system, we can obtain not only the large crystals but also all types of doping, namely, electron doping of Co or Ni substitution to Fe site, hole doping of K to Ba site, and isovalent doping of P to As site. However, despite intensive efforts, a lot of superconducting properties have remained incompletely understood. In particular, the pairing mechanism does not gain a consensus. One of the candidates for pairing, proposed just after the discovery of IBSs, is the spin-fluctuation mechanism [31, 32], as in cuprates. This seems quite natural since the superconductivity appears in the vicinity of AF ordered phase. On the other hand, it is also natural to view that the



superconducting dome appears with suppression of the structural transition. The corresponding theory is the orbital-fluctuation mechanism [15, 33]. Since these two mechanisms can be discriminated by the sign-reversal of superconducting order parameter (OP) between the disconnected FSs, several experimental approaches are attempted to determine the relative phase of the OP between FSs, such as inelastic neutron scattering, scanning tunneling microscopy under high-magnetic field, and impurity effect by means of chemical substitutions (Chapter 2). With a determination of the OP in IBSs with a help of those probes, we can properly understand how such high-temperature superconductivity emerges in IBSs.

Meanwhile, IBSs are expected for application aspects due to its high  $T_c$  and high critical current density  $J_c$  second to cuprates [34]. Additionally, IBSs have an advantage over cuprates in the property of small anisotropy [35], which can help to prepare high-performance superconducting wires [36]. Taking future applications into account, it is quite important to understand the vortex pinning properties and vortex dynamics to achieve high performance of transport current. From the scientific point of view, it is interesting to approach the intriguing phenomena of vortices, as in the case of cuprates [21]. This is not accounted for low-temperature superconductors, and intensive studies are carried out, forming new field of “vortex matter” physics. Understanding of vortex states under strong fluctuations has progressed in the study of cuprates. However, it is not clear if those vortex behaviors are universal in high-temperature superconductors or unique in cuprates. By investigating vortex properties in IBSs, we can achieve a comprehensive understanding of the vortex physics.

In order to achieve these two purposes, we investigate the change of the superconductivity in response to the introduction of disorder. In other words, it is required to reveal the effects of defects in IBSs, where the defects work as scattering centers or vortex pinning centers. The simplest way to introduce disorders is the chemical substitutions. Actually, the impurity effect or pinning properties have been examined with this method. However, the chemical substitution involves critical issues. For example, chemical substitutions have side effects such as doping of additional electrons or holes, changing the topology of FSs, and so on. In most cases, it is extremely difficult to distinguish the pure impurity scattering effect from another. Even if we could find a substitutions without such problems, chemical instability would occur at a large amount of substitution. It means that it is difficult to prepare highly substituted compounds due to the solubility limit. Moreover, even if this problem were overcome, the concomitant variations

of physical quantities due to sample piece dependence could not completely be eliminated. In fact, the temperature dependent resistivity in the chemically substituted samples does not show the parallel shift to that in non-substituted one, which indicates that the pure introduction of scattering centers is not properly realized. By contrast, the particle irradiation is the powerful tool to solve these problems. By means of the irradiation, we can introduce disorder in a stepwise fashion with desired amounts in a given sample, which completely removes the sample dependency. Besides, with a suitable choice of ions and their energy, the morphology of the defects are controllable. Actually, it is known in cuprates that random point defects are created by light particles such as electrons, protons, and  $\alpha$ -particles, whereas swift heavy ions such as gold and lead form tracks correlated along the velocity vector of particles.

In order to clarify the effects of disorders in IBSs, we study the change of superconductivity by particle irradiation in electron- and hole-doped  $\text{BaFe}_2\text{As}_2$  in the present work. This thesis is organized as following. In chapter 2, we briefly review the second class of high-temperature superconductors of IBSs. In chapter 3, we introduce the vortex pinning and dynamics in high-temperature superconductors under dc magnetic field after referring the vortices in the conventional superconductors. In chapter 4, the details of crystal-growth method and a brief review of the measurement techniques are described, where the particle irradiation, the marked approach in this study, is included. The first topic, the pair-breaking effect in IBSs, is discussed in chapter 5. Subsequently, the vortex pinning and dynamics with the introduction of point defects and columnar defects created by the irradiation are discussed in chapters 6 and 7, respectively. Finally we summarize the work in this thesis and give conclusions.

## Chapter 2

# Iron-based superconductors

### 2.1 Crystal structure

The iron-based superconductors (IBSs) have a layered structure with alternatively stacks of conducting layers and blocking layers, which is schematically shown in Fig. 2.1. The material variety of this class is very large. The first discovered IBSs are  $LnFeAsO$  (so-called 1111) system, where  $Ln$  is lanthanide such as La, Pr, Sm, Nd, and so on. The undoped sample does not show the superconductivity, while it appears in the sample with substitution of fluorine for oxygen, or with oxygen deficiency. The highest transition temperature ( $T_c$ ) reaches 56 K in  $Ln = \text{Sm}$  or  $\text{Nd}$ . However, there is a serious problem in 1111 system of the difficulty to obtain large single crystals. Another class of  $AEFe_2As_2$  (122) system solves this problem. Single crystals with mm-size are easily grown by self-flux method. Besides, many different kinds of superconducting materials are available. Even if we concentrate on  $AE = \text{Ba}$ , we can get all types of doped systems of hole, electron, and isovalent doping with substitution of K for Ba, Co for Fe, and P for As, respectively. The highest  $T_c$  in these materials are 38, 25, and 31 K, respectively. Although they are not as high as 1111 system, the advantage of large single crystals are widely utilized in fundamental studies.

It is noteworthy that the local structure of  $\text{FeAs}_4$  tetrahedron strongly affects to  $T_c$ . The so-called "Lee plot", shown in Fig. 2.2, suggests that the highest  $T_c$  is realized when  $\text{FeAs}_4$  is the regular tetrahedron [3].

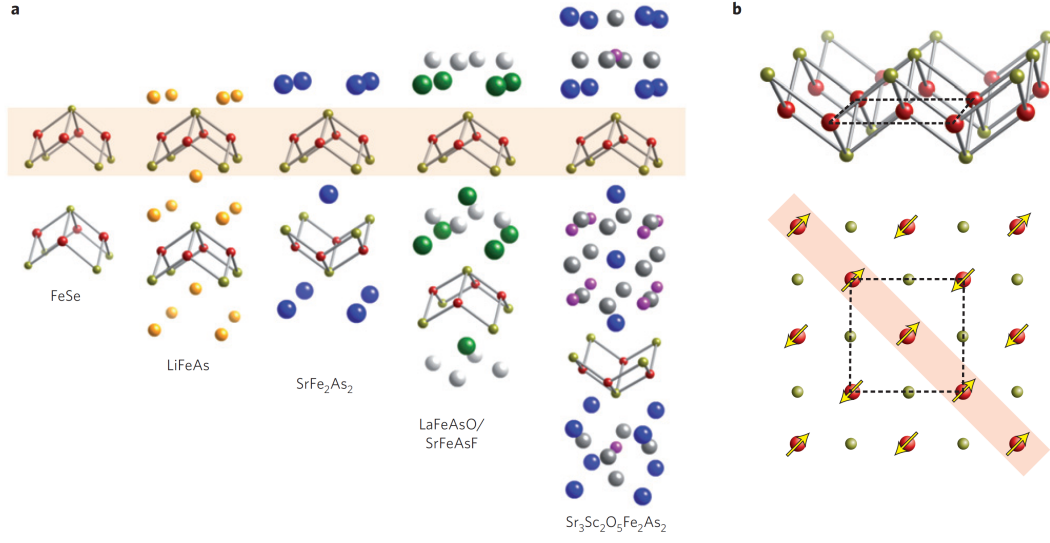


Figure 2.1: (a) The schematic view of the crystal structure for several kinds of IBSs. (b) The common structure of FeAs plane and its spin structure. (Source of figure: [2])

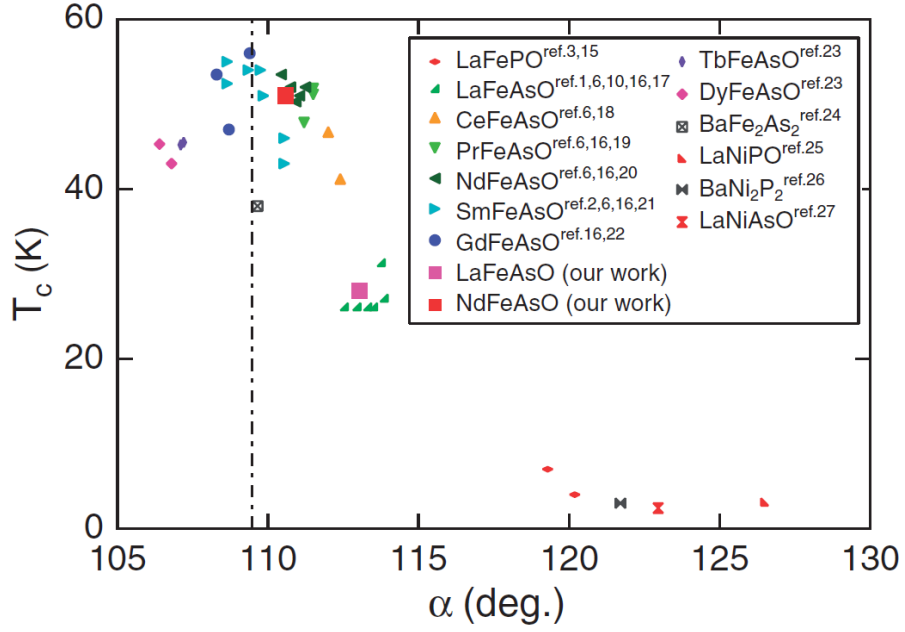


Figure 2.2:  $T_c$  as a function of the bond angle  $\alpha$  in As-Fe-As (so-called Lee plot). The vertical line indicates the angle of  $\alpha = 109.47^\circ$  at the regular tetrahedron of FeAs<sub>4</sub>. (Source of figure: [3])

## 2.2 Electronic structure

The parent compound of IBSs is a semimetal, which is in contrast to a Mott insulator in cuprates. According to the theoretical calculation and valence-band photoemission spectra, the Fermi surfaces (FSs) in IBSs are predominantly constructed by Fe 3*d*-electrons, as shown in Fig. 2.3. This situation is very similar to the CuO<sub>2</sub> layer in cuprates. However, the striking difference can be seen between cuprates and IBSs, namely, the multi-band nature and disconnected FSs. Figure 2.4 is the FSs in electron-doped and hole-doped BaFe<sub>2</sub>As<sub>2</sub> obtained by the density-functional calculation. Although the details of the structure depend on the doping level, the hole FSs and electron FSs exist at the zone center and the zone corner, respectively, in the case of BaFe<sub>2</sub>As<sub>2</sub>. This trend is applicable for most of the IBS compounds. Due to this FSs, the parent compound has a nesting vector, showing the magnetic order at low temperatures.

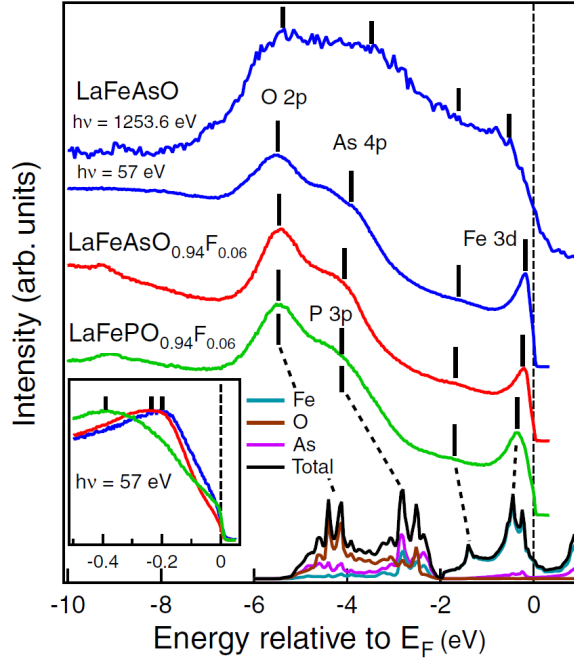
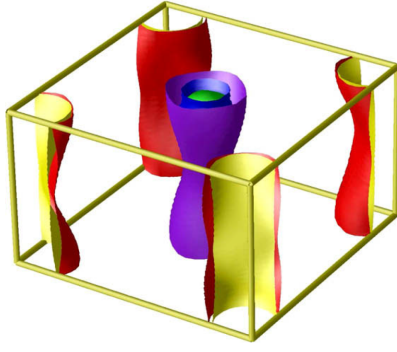
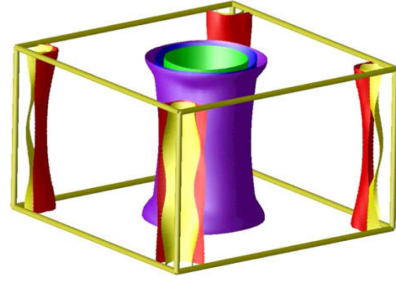


Figure 2.3: Valence-band photoemission spectra in IBSs of LaFeAsO<sub>1-x</sub>F<sub>x</sub> ( $x = 0, 0.06$ ) and LaFePO<sub>0.94</sub>F<sub>0.06</sub> and their comparison with band-structure calculation. Vertical bars mark main features observed in the spectra. The inset presents the near- $E_F$  spectra. (Source of figure: [4])

The nesting vector, which is the origin of spin-fluctuations, is shown in Fig. 2.5(a) and (b) for cuprates and IBSs, respectively. In the cuprates the FS is large, and antiferromagnetic  $Q = (\pi, \pi)$  connects points on the same FS. Since the spin-mediated interaction is positive



**Fig. 2.** The Fermi surface of the nonmagnetic  $\text{BaFe}_2\text{As}_2$  for 10% e-doping (Co doping, virtual crystal approximation) [4].



**Fig. 4.** The Fermi surface of  $\text{BaFe}_2\text{As}_2$  for 20% h-doping (corresponding to  $\text{Ba}_{1.6}\text{K}_{0.4}\text{Fe}_2\text{As}_2$ , calculated as 40% Cs doping in the virtual crystal approximation) [4]. Note that, had we use the calculated As positions instead of the experimental ones, the FS would have been much more 3D.

Figure 2.4: The FSs in (a) electron-doped  $\text{BaFe}_2\text{As}_2$  and (b) hole-doped  $\text{BaFe}_2\text{As}_2$ , calculated by the density-functional theory. (Source of figure: [5])

(repulsive), the gap must change sign between FS points separated by  $Q$ . Consequently, the gap changes the sign twice along the FS. This implies a  $d$ -wave gap symmetry. In IBSs, scattering by  $Q$  moves electrons from one FS to another. In this situation, the gap must change sign between different FSs but to first approximation remains a constant on a given FS. By symmetry, such a gap is an  $s$ -wave gap. It is called  $s_{\pm}$  because it changes sign between different FSs. However, another pairing interaction is proposed, namely, the orbital fluctuations. We review these pairing mechanisms later.

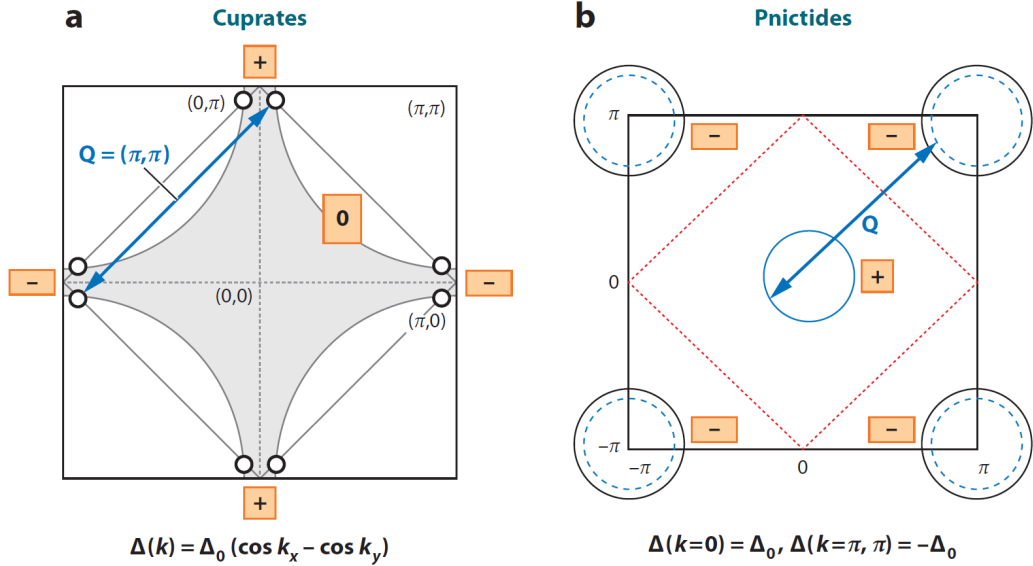


Figure 2.5: A comparison of the pairing state from spin-fluctuation exchange in (a) cuprates and (b) IBSs. (Source of figure: [6])

## 2.3 Superconducting properties

In this section, we briefly review the normal and superconducting properties in IBSs. The resistivity is one of the most fundamental characterization. Figures 2.6(a), 2.6(b) and 2.6(c) shows the temperature dependence of resistivity  $\rho$  in Co-doped, P-doped, and K-doped  $\text{BaFe}_2\text{As}_2$ , respectively. In the parent compound of  $\text{BaFe}_2\text{As}_2$ , the structural and anti-ferromagnetic transition is observed at  $T_S = T_{\text{AF}} = 143$  K. With increasing doping level, these transitions are dragged down to lower temperatures with a slight separation each other, and the superconducting transition appears. The optimal doping level for the superconducting transition can be seen at a further doping level, where  $T_s$  and  $T_{\text{AF}}$  reach 0 K. The electronic phase diagram for these compounds are shown in Figs. 2.7(d), 2.7(e) and 2.7(f), respectively. In general, these are quite similar to each other. However, we can see some differences, such as the suppression rate of  $T_s$  with doping, the optimal doping level, and the  $x$  at which the superconductivity disappears. It is noteworthy that the residual resistivity (RR) is largely different among different doping systems, as shown in Figs. 2.7(a), 2.7(b), and 2.7(c). In Co-doped system, RR at the optimal level is  $\sim 100 \mu\Omega\text{cm}$ , while much smaller RR is observed in P-doped and K-doped systems with  $\sim 10 \mu\Omega\text{cm}$  and  $\sim 1 \mu\Omega\text{cm}$ , respectively. These trends correspond to how the doping atoms are close to Fe sites, i.e., the doping at Fe site leads to a large RR, whereas the doping at blocking layer does not.

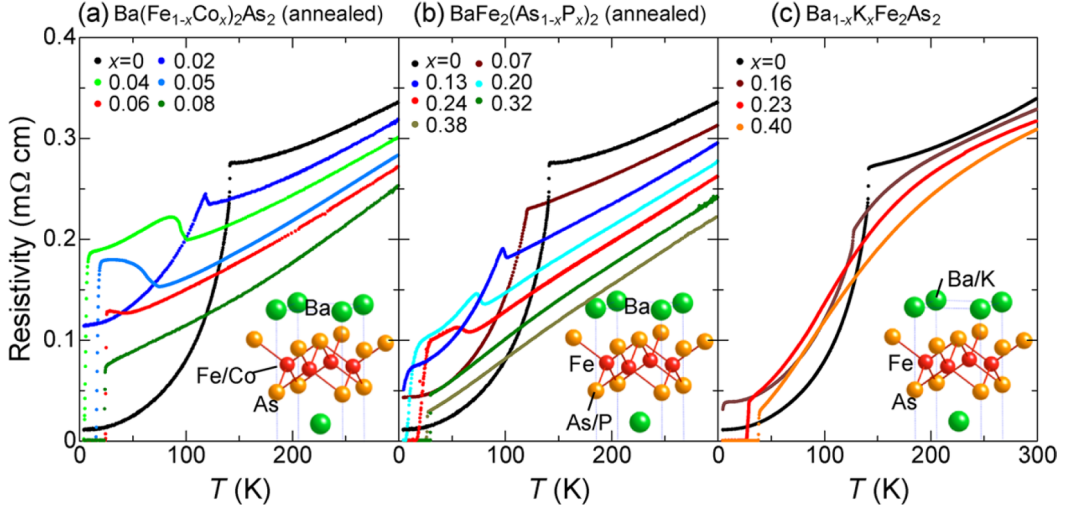


Figure 2.6: Temperature dependence of resistivity with several doping levels from  $x = 0$  to  $x = x_{\text{opt}}$  in (a)  $\text{Ba}(\text{Fe}_{1-x}\text{Co}_x)_2\text{As}_2$ , (b)  $\text{BaFe}_2(\text{As}_{1-x}\text{P}_x)_2$ , and (c)  $\text{Ba}_{1-x}\text{K}_x\text{Fe}_2\text{As}_2$ . For Co-doped and P-doped systems, the samples were annealed with BaAs. (Source of figure: [7])

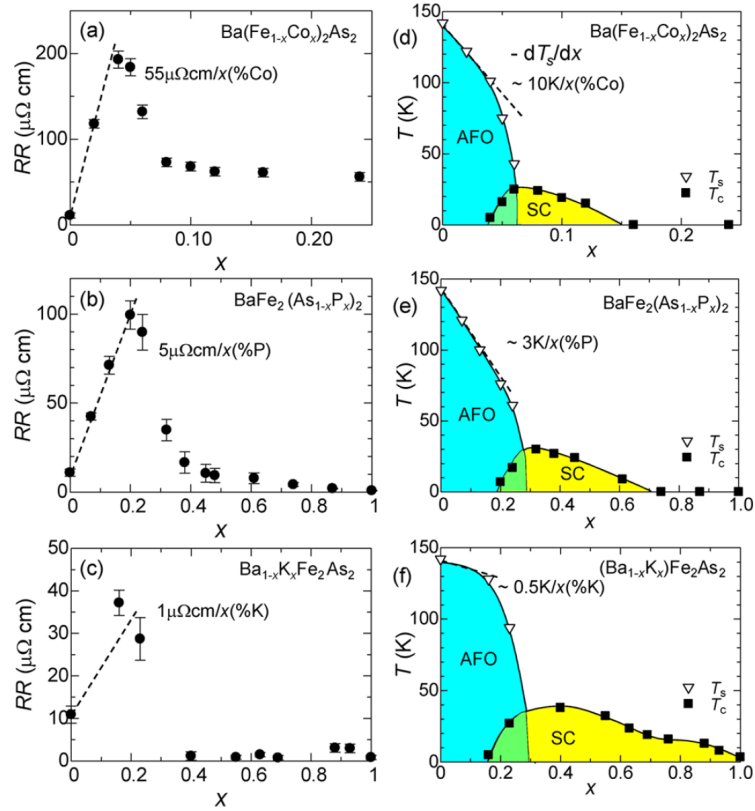


Figure 2.7: Temperature dependence of resistivity with several doping levels from  $x = 0$  to  $x = x_{\text{opt}}$  in (a)  $\text{Ba}(\text{Fe}_{1-x}\text{Co}_x)_2\text{As}_2$ , (b)  $\text{BaFe}_2(\text{As}_{1-x}\text{P}_x)_2$ , and (c)  $\text{Ba}_{1-x}\text{K}_x\text{Fe}_2\text{As}_2$ . For Co-doped and P-doped systems, the samples were annealed with BaAs. (Source of figure: [7])

In contrast to quasi two-dimensional superconductivity, where the out-of-plane electron mass is much heavier than the in-plane one, IBSs show an almost isotropic upper critical field ( $H_{c2}$ ) at low temperatures. The results in  $(\text{Ba},\text{K})\text{Fe}_2\text{As}_2$  are represented in the main panel of Fig. 2.8. In the lower inset of Fig. 2.8, the anisotropy is explicitly shown as the anisotropy parameter  $\gamma = H_{c2}^{\perp}/H_{c2}^{\parallel}$ , where  $H_{c2}^{\perp}$  and  $H_{c2}^{\parallel}$  are  $H_{c2}$  under out-of-plane  $H$  and in-plane  $H$ , respectively. We can see almost isotropic behavior of  $H_{c2}$ , namely,  $\gamma \simeq 1$  at low temperatures and at most  $\gamma \simeq 2$  around  $T_c$ , which is in sharp contrast to cuprates, such as  $\gamma = 5 - 7$  in  $\text{YBa}_2\text{Cu}_3\text{O}_{7-\delta}$  and  $\gamma = 50 - 200$  in  $\text{Bi}_2\text{Sr}_2\text{CaCu}_2\text{O}_{8+\delta}$ .

The probe for the low-energy quasiparticle excitation determines whether the superconducting gap is fully opened or nodal. The existence of nodes in the superconducting gap affects the thermodynamic properties at low temperatures, such as the specific heat and the thermal conductivity. Besides, it is important to know the node in the superconducting gap, since the information of the nodal structure helps to determine the superconducting-pairing mechanism.



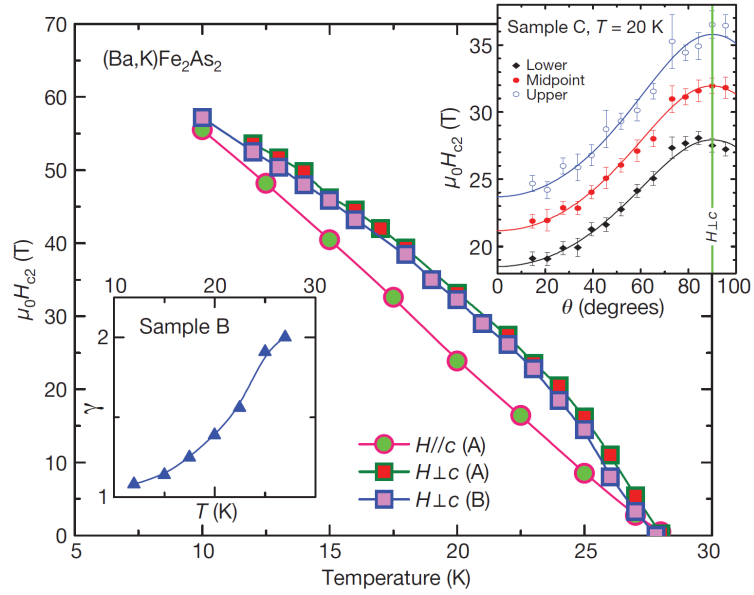


Figure 2.8: Upper critical field  $H_{c2}$  under applied field perpendicular and parallel to the FeAs plane. The anisotropy parameter  $\gamma = H_{c2}^{\perp}/H_{c2}^{\parallel}$  is shown in lower inset. (Source of figure: [8])

One of such probes is the penetration depth  $\lambda$ , which is related to the superfluid density  $n_s$  via  $n_s = (mc^2/4\pi e^2)\lambda^{-2}$ . The temperature dependence of  $\lambda$  in the low temperature limit gives the exponential behavior in the optimal doping levels of  $(\text{Ba,K})\text{Fe}_2\text{As}_2$  (Fig. 2.9) and  $\text{Ba}(\text{Fe,Co})_2\text{As}_2$ , although some exceptions are observed in the overdoped samples of K-doped and Co-doped systems and a wide range of  $\text{BaFe}_2(\text{As,P})_2$  [37]. The exponential behavior corresponds to the fully gapped state, while the  $T$ -linear decrease is attributed to the presence of the line nodes, such as  $d$ -wave state. The specific heat and the thermal transport at low temperature also support these gap structure [38, 39, 40]. Such nonuniversal behaviors, as can be sketched in Fig. 2.10, imply that the line nodes are not symmetry-imposed but the accidental one. For example, the loop nodes are suggested in angular-dependent thermal-conductivity measurements in  $\text{BaFe}_2(\text{As,P})_2$  [41], while the octet line nodes are observed in the end member of  $\text{KFe}_2\text{As}_2$  [42]. In addition, the recent electron irradiation in  $\text{BaFe}_2(\text{As,P})_2$  implies the disappearance of the nodal behaviors [43]. The nodal or nodeless gap structure is represented in the phase diagram of  $\text{BaFe}_2\text{As}_2$  with Co-doping, K-doping, and P-doping are shown in Fig. 2.11 [10].

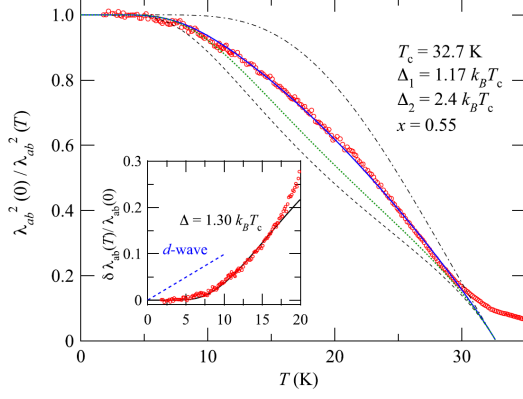


Figure 2.9: The temperature dependence of the superfluid density in  $\text{Ba}_{0.45}\text{K}_{0.55}\text{Fe}_2\text{As}_2$ . The flat region at low temperature indicates the fully-opened superconducting gap. Inset: The exponential behavior of  $\delta\lambda_{ab}(T)/\lambda_{ab}(0)$  at low temperature.  $T$ -linear dependence expected in clean  $d$ -wave superconductors are also represented by the broken line. (Source of figure: [9])

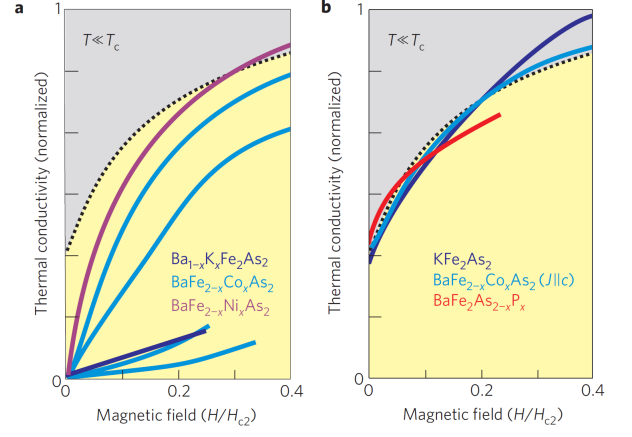


Figure 2.10: The normalized-field dependence of the electronic thermal conductivity at low temperature limit in doped  $\text{BaFe}_2\text{As}_2$ . The behavior expected in fully-gapped superconductors is observed in (a), while the presence of line node is suggested in (b). (Source of figure: [2])

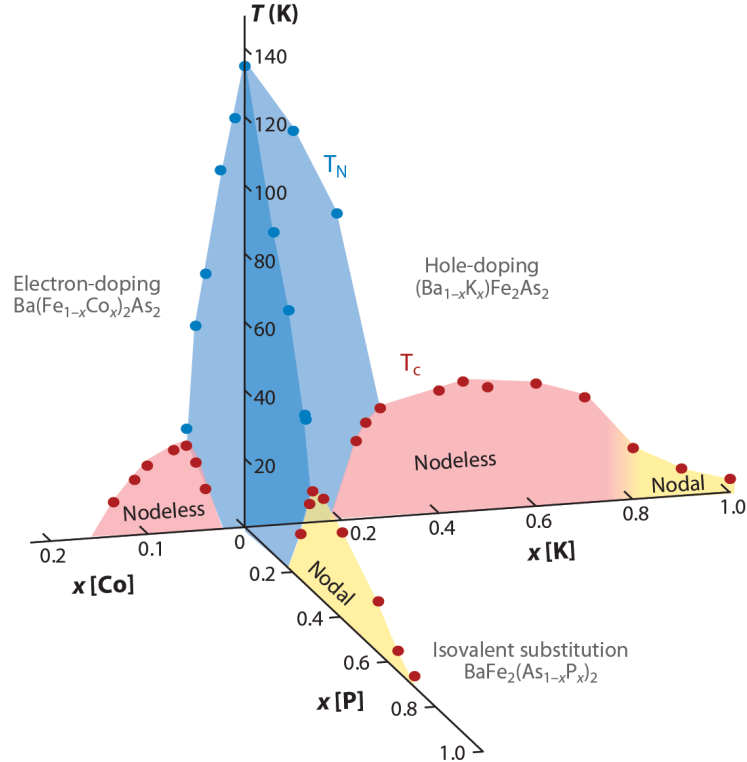


Figure 2.11: Electronic phase diagram in electron-doping  $\text{Ba}(\text{Fe}_{1-x}\text{Co}_x)_2\text{As}_2$ , isovalent doping  $\text{BaFe}_2(\text{As}_{1-x}\text{P}_x)_2$ , and hole-doping  $(\text{Ba}_{1-x}\text{K}_x)\text{Fe}_2\text{As}_2$ . (Source of figure: [10])

## 2.4 Superconducting pairing mechanism

The parent compound undergoes the paramagnetic to anti-ferromagnetic transition concomitantly with tetragonal to orthorhombic transition upon cooling. The superconducting dome appears near the critical concentration of doping where the anti-ferromagnetic transition is completely suppressed, which implies the close relationship between the magnetic correlation and the superconductivity. This is very similar to the cuprate superconductors.

In fact, the superconductivity in cuprates is thought to be mediated by anti-ferromagnetic fluctuations. If the same mechanism is dominant also in IBSs originating from nesting between hole and electron pockets,  $s$ -wave but the anti-phase superconducting gap between these FSs are realized. This gapped state is the so-called  $s_{\pm}$ -wave state. On the other hand, another intriguing mechanism is proposed, where the orbital fluctuations are the glue of the pairing. In this case, the sign-reversal is absent, and  $s_{++}$ -wave state should be realized. In the following, we will see some experimental approaches to examine the superconducting gap structure.

### 2.4.1 Angle-resolved photoemission spectroscopy

In the spin-fluctuation mechanism, the superconducting gap is closely related to the spin susceptibility. The calculated susceptibility indicates that the dominant contribution is given by the pair scattering between the disconnected FSs having the same orbital character (intraorbital pairing). In this case, the gap  $\Delta$  is anticipated to be highly sensitive to the orbital character. In this point of view, the angle-resolved photoemission spectroscopy (ARPES) is a powerful tool since this can directly measure the momentum-resolved information at the FSs. Especially, the polarized laser-ARPES can distinguish the orbital character on each FS. According to ARPES observation, the magnitude of the superconducting gap is independent of the FSs, which is inconsistent with the orbital-dependent superconducting-gap magnitude predicted by the spin-fluctuation scenario. For example, the orbital character  $3Z^2 - R^2$  in 122 system does not have a contribution in the electron FS at the zone corner, which leads to the suppression of intra-orbital pairing between the disconnected FSs and  $\Delta$  derived from  $3Z^2 - R^2$  orbital should be very small. According to the band calculation, the  $3Z^2 - R^2$  orbital dominates the outer hole FS around  $k_z \sim \pi$  in  $\text{BaFe}_2(\text{As}_{1-x}\text{P}_x)_2$ , which is confirmed by the polarized laser ARPES. Taking it into account, the fact that the superconducting gap size is similar among the FSs having

various orbital character (Figs. 2.12 and 2.13), including the FS with  $3Z^2 - R^2$  orbital, shows the mechanism of the superconducting pairing is not accountable only by the spin fluctuations.

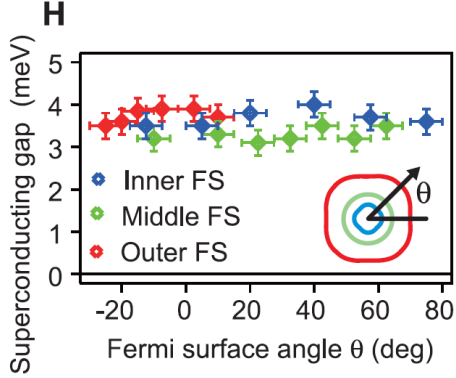


Figure 2.12: The angular dependence of the superconducting gap in each FS determined by the laser-ARPES measurement in BaFe<sub>2</sub>(As<sub>0.65</sub>P<sub>0.35</sub>)<sub>2</sub>. Inset: the definition of the angle  $\theta$  in FS. (Source of figure: [11])

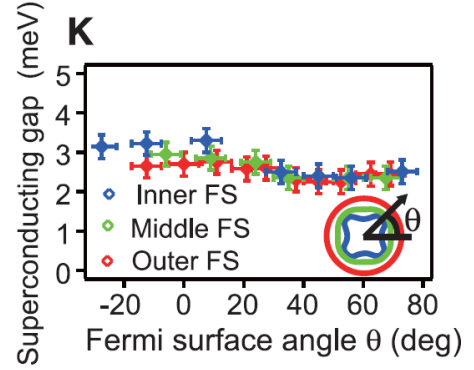


Figure 2.13: The angular dependence of the superconducting gap in each FS determined by the laser-ARPES measurement in Ba<sub>0.6</sub>K<sub>0.4</sub>Fe<sub>2</sub>As<sub>2</sub>. Inset: the definition of the angle  $\theta$  in FS. (Source of figure: [11])

#### 2.4.2 Inelastic neutron scattering

The observation of the spin resonance peak in the inelastic neutron scattering (INS) indicates that the magnetic pairing mechanism is involved in the heavy-fermion and cuprate superconductors [44, 45, 46, 47, 48, 49]. In IBSs several groups observed the hump structure in the spin susceptibility [50, 51, 12], which is assigned to the resonance peak. Figure 2.14 shows the example in the Ba(Fe,Co)<sub>2</sub>As<sub>2</sub> at the normal and the superconducting states. They concluded that this peak at the superconducting state is the evidence for the sign-reversal in the superconducting gap function. However, it is pointed out that the observed peak structure is too broad to be assigned to the resonance peak and is doubtful that the resonance condition is satisfied. In fact, Onari *et al.* has theoretically shown the prominent hump structure in  $s_{++}$ -wave state [13], where the quasiparticle damping is related to this hump structure. They also calculated for  $s_{\pm}$ -wave state, where the peak is much sharper as indicated in Fig. 2.15. Consequently the broad spectral peak in INS can be well reproduced under the assumption of  $s_{++}$ -wave state, rather than  $s_{\pm}$ -wave state.

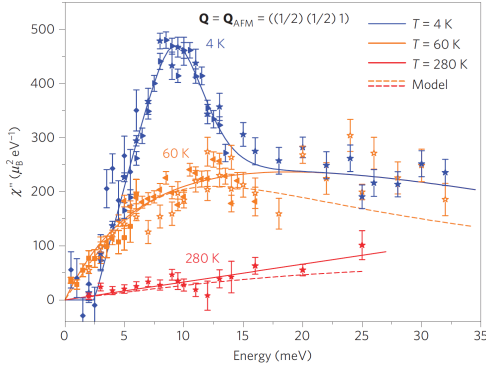


Figure 2.14: The imaginary part of the spin susceptibility in Ba(Fe<sub>0.925</sub>Co<sub>0.075</sub>)<sub>2</sub>As<sub>2</sub> at the superconducting state ( $T = 4$  K) and the normal state ( $T = 60, 280$  K). (Source of figure: [12])

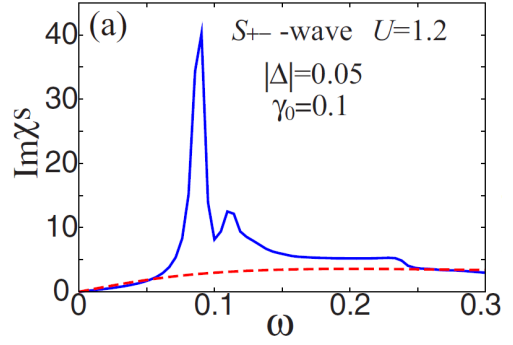


Figure 2.15: The calculated imaginary part of the spin susceptibility in the  $s_{+-}$ -wave superconducting state (blue line) and the normal state (red broken line). (Source of figure: [13])

### 2.4.3 Scanning-tunneling microscopy

The scanning-tunneling microscopy (STM) technique is utilized as the phase-sensitive probe, since the quasiparticle interference (QPI) pattern under the magnetic field gives an information of the relative sign of the superconducting gap. In fact, this technique achieved a great success in cuprates to confirm the  $d_{x^2-y^2}$ -wave state [52, 53]. Similar measurements and analyses are applied to Fe(Te,Se) [14], in which an electrically neutral surface can be obtained among IBSs. At the specific  $\mathbf{q}$  of  $\mathbf{q}_2 = (\pi, 0)$  connected between hole and electron disconnected FSs, the QPI signals are suppressed at high magnetic fields, which is in contrast to the increase of intensities at  $\mathbf{q}_3 = (\pi, \pi)$ , as shown in Fig. 2.16. This result seems to be a strong evidence for the realization of  $s_{\pm}$ -wave state. However, the model adopted for analysis is similar to that used in cuprates, which might have a problem if the multiband or multiorbital nature is important. In fact, it is suggested that the suppression of QPI signal is possibly realized in the framework of  $s_{++}$ -wave state [54]. Further theoretical studies are necessary for understanding the results of STM.

### 2.4.4 Impurity effects on the superconducting transition temperature by chemical substitution

Historically, the impurity effect has played a role to determine the superconducting gap structure. If the isotropic gap is opened in the single band (classic  $s$ -wave state), the impurity effect on the superconductivity is strongly dependent on the magnetism of the impurity. If the impurities are

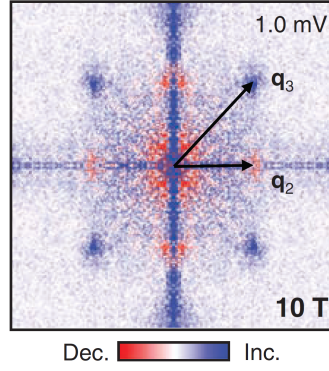


Figure 2.16: The magnetic-field induced change in QPI intensities.  $\mathbf{q}_2 = (\pi, 0)$  and  $\mathbf{q}_3 = (\pi, 0)$  are the  $\mathbf{q}$  vector connecting hole-electron FSs and hole-hole FSs, respectively. (Source of figure: [14])

non-magnetic, the Anderson's theorem manifests that  $T_c$  is invariant with non-magnetic impurity concentration  $n_{\text{imp}}$  as far as  $n_{\text{imp}}$  is small enough not to induce the localization. By contrast, the magnetic impurities immediately suppress the superconductivity in accordance with Abrikosov-Gor'kov (AG) theory. In AG theory, the relation between  $T_c$  and the pair-scattering rate by impurities,  $\tau$ , is described as

$$\ln \frac{T_c}{T_{c0}} = \psi\left(\frac{1}{2}\right) - \psi\left(\frac{1}{2} + \frac{\alpha}{2\pi k T_c}\right), \quad (2.1)$$

where  $T_{c0}$  is  $T_c$  without pair-breaking effect,  $\alpha = \hbar/2\tau$  is the pair-breaking parameter,  $\psi(x)$  is digamma function. When  $\alpha$  reaches the critical value of  $2\alpha_c = \Delta_0 \equiv 1.76kT_c$ , the superconductivity is disappeared, where  $\Delta_0$  is the superconducting gap at zero temperature. Equation (2.1) gives the universal relation between  $T_c/T_{c0}$  and  $2\alpha/\Delta_0$ . On the contrary,  $d$ -wave state is very fragile not only to magnetic but also to non-magnetic impurity. This is because the scattering by means of non-magnetic impurities is qualitatively explained as averaging the superconducting gap. Then, the question of the nonmagnetic-impurity effect on the multiband superconductors arises, which is the case in IBSs. For simplicity, we consider two bands. The relative amplitude and the phase of the superconducting gap function can be different between these two bands. It is easy to understand in the absence of the phase difference, where the conventional Anderson's theory is expected to hold. However, the anti-phase state of  $s_{\pm}$ -wave is realized, both gaps are expected to go toward zero due to the averaging role for gaps by the impurity scattering. Such an intuitive inspection of the contrast between  $s_{++}$  and  $s_{\pm}$  states is confirmed based on the

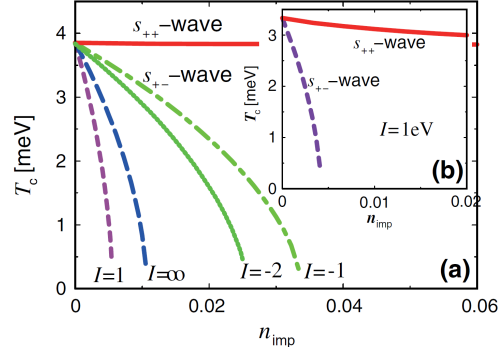


Figure 2.17: The robustness of  $T_c$  with an introduction of nonmagnetic impurities in the case of  $s_{\pm}$ -wave state and  $s_{++}$ -wave state. (Source of figure: [15])

5-orbital model [15, 33, 55, 56], as depicted in Fig. 2.17, which correctly treats the multiorbital effect. In chapter 5, we discuss which state is plausible in IBSs.

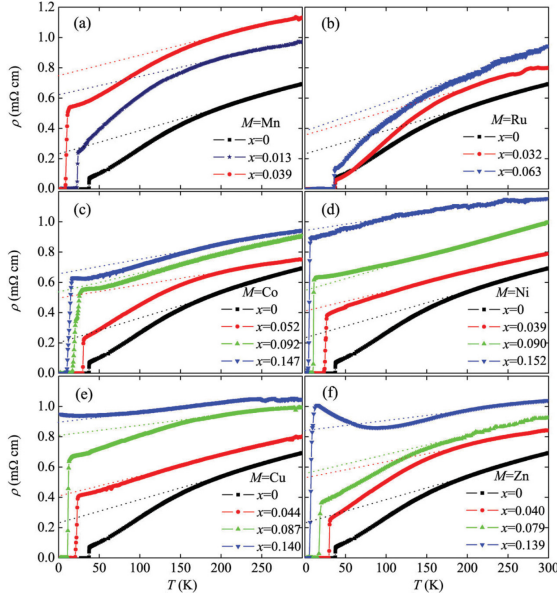


Figure 2.18: The temperature dependence of  $\rho$  in  $\text{Ba}_{0.5}\text{K}_{0.5}\text{Fe}_{2-2x}\text{M}_{2x}\text{As}_2$  ( $M = \text{Mn, Ru, Co, Ni, Cu, and Zn}$ ). (Source of figure: [16])

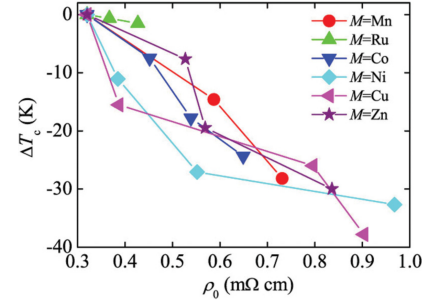


Figure 2.19: The suppression of  $T_c$  as a function of the residual resistivity  $\rho_0$  in chemically substituted  $\text{Ba}_{0.5}\text{K}_{0.5}\text{Fe}_{2-2x}\text{M}_{2x}\text{As}_2$  ( $M = \text{Mn, Ru, Co, Ni, Cu, and Zn}$ ). (Source of figure: [16])

First experimental results were obtained in the polycrystalline sample. For example, Sato *et al.* measured the temperature dependence of the resistivity  $\rho(T)$  in the  $\text{LnFeAs}(\text{O},\text{F})$  polycrystal with several concentrations of impurities, where  $\text{Ln}$  is La or Nd [57]. They finally concluded the inconsistency of the robustness of  $T_c$  with  $s_{\pm}$ -wave state. Although those experiments are

carefully performed, the magnitude of the impurity-scattering rate is difficult to extract from the overall resistance due to ambiguity of the resistivity ratio of intragrain to intergrain. Therefore the study in the single crystals are quite important to get a quantitative agreement. Such a study in the single crystals is reported in  $\text{Ba}(\text{Fe},\text{Co})_2\text{As}_2$  and  $(\text{Ba},\text{K})\text{Fe}_2\text{As}_2$  with chemical substitutions such as Zn [58, 16]. Fig. 2.18 shows  $\rho(T)$  of the chemically substituted  $(\text{Ba},\text{K})\text{Fe}_2\text{As}_2$ . To evaluate the impurity scattering rate, the suppression of  $T_c$  as a function of the residual resistivity  $\rho_0$  is plotted in Fig. 2.19. Regardless of impurity atoms,  $T_c$  is fully suppressed at  $\rho_0 = 1 \text{ m}\Omega\text{cm}$ , although there is a problem in the determination of  $\rho_0$  since the evolution of  $\rho$  is not parallel with the introduction of impurities.

The peculiar way to introduce point defects is performed by particle irradiation. The *in situ* resistive measurements has an advantage to irradiate just after the irradiation at low temperature [59, 60, 17, 61]. The example in  $\text{YBa}_2\text{Cu}_3\text{O}_{7-\delta}$  are shown in Fig. 2.20. The monotonic increase of  $\rho$  is detected with increasing amounts of defects. It is noted that at higher doses of irradiation  $\rho$  at low temperatures shows an upturn, attributable to Kondo effect or localization. For a quantitative analyses,  $T_c$  is plotted against the increase of  $\rho$ . The results are consistently explained by *d*-wave with localization, as shown in Fig. 2.21.

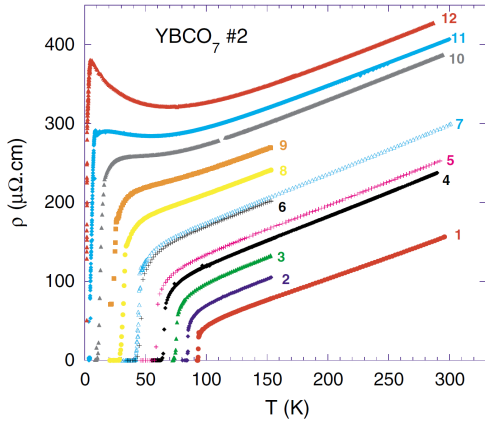


Figure 2.20: The temperature dependence of resistivity in single crystal of  $\text{YBa}_2\text{Cu}_3\text{O}_{7-\delta}$  with 2.5-MeV electron irradiation. (Source of figure: [17])

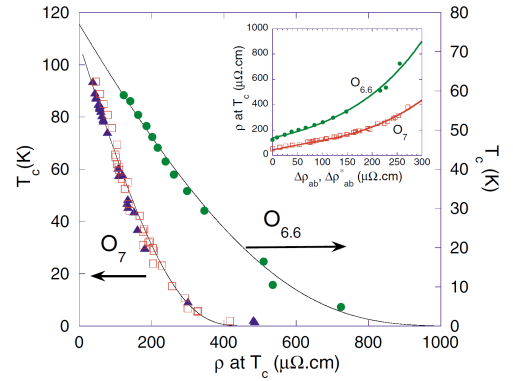


Figure 2.21: The decrease of  $T_c$  as a function of the resistivity just above  $T_c$ ,  $\rho(T_c)$ . (Source of figure: [17])

Similar techniques have been utilized in IBSs such as  $\text{NdFeAsO}$  [62] and  $\text{Ba}(\text{Fe}_{1-x}\text{Co}_x)_2\text{As}_2$  [18]. In  $\text{NdFeAsO}$ , the data processing is difficult due to Kondo effect or localization. On the other hand, in  $\text{Ba}(\text{Fe}_{1-x}\text{Co}_x)_2\text{As}_2$ , the low- $T$  upturn is not identified, where the results manifest that



$s_{\pm}$ -wave state is unlikely.

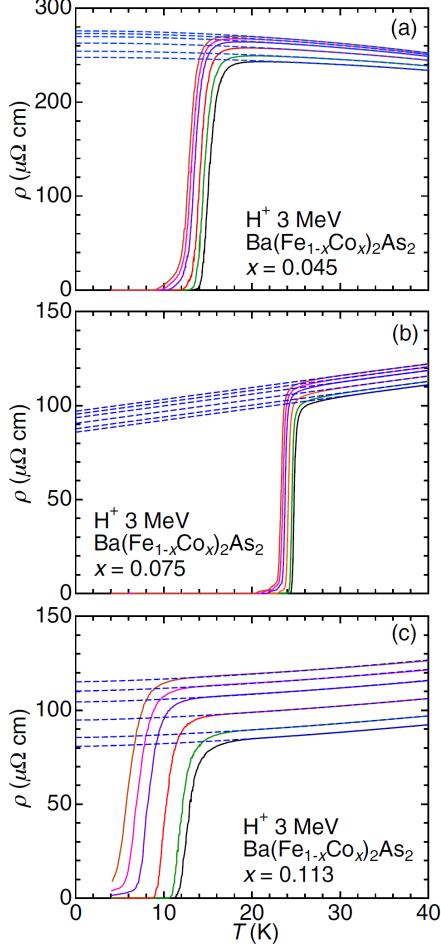


Figure 2.22: The temperature dependence of resistivity in single crystal of  $\text{Ba}(\text{Fe}_{1-x}\text{Co}_x)_2\text{As}_2$  with 3-MeV proton irradiation. (Source of figure: [18])

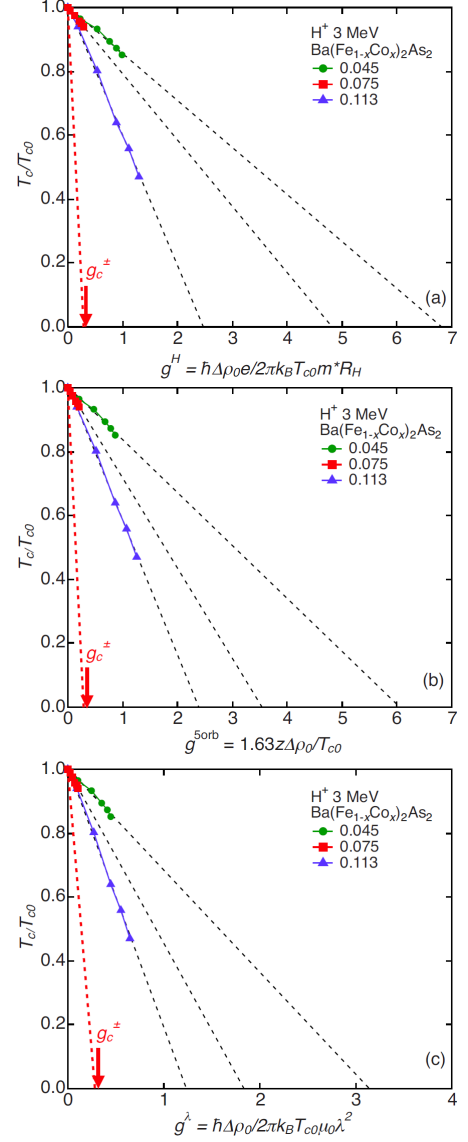


Figure 2.23: The reduced temperature  $T_c/T_{c0}$  as a function of the normalized relaxation rate  $g$  in 3-MeV proton irradiated  $\text{Ba}(\text{Fe}_{1-x}\text{Co}_x)_2\text{As}_2$  single crystals.  $g_c$  is the critical value of  $g$  for  $s_{\pm}$ -wave state. (Source of figure: [18])

#### 2.4.5 Summary and the motivation of our study

Although the unconventional gap symmetry of  $s_{\pm}$  in IBSs has received attention, the conclusive evidence has not been found so far. The  $s_{\pm}$ -wave state seems inconsistent with the results of laser-ARPES. The interpretation of INS and STM is not enough to conclude the gap symme-

try in IBSs, where the damping effects or the multiband nature should be taken into account. Furthermore, the impurities effects on  $T_c$  is much smaller than the theoretical prediction in  $s_{\pm}$ -wave state based on the five-orbital model. Accounting all the above, the realization of  $s_{\pm}$ -wave state is doubtful, and  $s_{++}$ -wave state seems rather appropriate to understand the experimental results. Therefore the gap symmetry should be carefully reexamined by means of the phase-sensitive probe. We will see this theme in chapter 5. Here we stress the pairing interactions of spin fluctuations and orbital fluctuations are not exclusive, and the crossover between  $s_{\pm}$ -wave state and  $s_{++}$ -wave state is possible by changing the strength of each interaction. In fact, both interactions seems important in  $\text{KFe}_2\text{As}_2$  to explain the FS dependent gap magnitudes observed in laser-ARPES. Subsequent experimental study is performed for heavily overdoped  $(\text{Ba,K})\text{Fe}_2\text{As}_2$  by means of the thermal transport and the penetration depth, suggesting the transition from  $s_{++}$ -wave state to  $s_{\pm}$ -wave state. We also note that these results also support that the superconducting pairing is not realized only from the spin fluctuations. The point we investigate is whether the superconductivity is mediated only or predominantly by the spin-fluctuation mechanism, in which case the  $s_{\pm}$ -wave state with sign reversal between the disconnected hole and electron FSs is realized. Even if the realization of  $s_{++}$ -wave state is concluded, we do not exclude the presence of spin fluctuations itself, whereas it points out the importance of the other mechanism, possibly the orbital fluctuations.

## Chapter 3

# Vortex matter in high-temperature superconductors

### 3.1 Vortex structure and vortex-line energy

The small magnetic field is expelled from a superconductor by Meissner effect. In type II superconductors, where  $\kappa$  is the ratio of the penetration depth  $\lambda$  to the coherence length  $\xi$  is larger than  $1/\sqrt{2}$ , the magnetic flux enters into a superconductor in terms of flux quantum under a relatively large field. Such a magnetic property is observed between the lower critical field  $H_{c1}$  and the upper critical field  $H_{c2}$ , and the superconducting state with flux quanta is called the mixed state. It is the result from the negative surface energy. The flux quantum has the value

$$\phi_0 = \frac{hc}{2e} \tag{3.1}$$

$$= 2.07 \times 10^{-7} \text{G cm}^2, \tag{3.2}$$

where  $h$ ,  $c$ , and  $e$  are the Planck's constant, the velocity of light, and the elementary charge. Due to its circulating structure of the current, the quantized flux in a superconductor is called "vortex". The schematic structure of the vortex is illustrated in Fig 3.1. In the simplest model, the core with a radius of  $\sqrt{2}\xi \sim \xi$  is dealt as the normal state, and the circulating current reaches as far as  $\lambda$ .

In an isotropic superconductor, the vortex-line energy per unit length, or the line tension, is

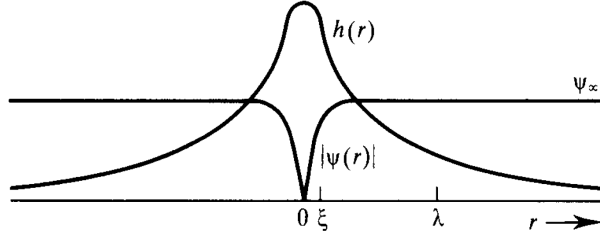


Figure 3.1: The structure of isolated vortex in a superconductor with  $\kappa \approx 8$ . The superconducting order parameter  $\Psi$  is suppressed at the vortex core  $r \approx 0$ , and the local magnetic field  $h$  is screened outside the core  $r \rightarrow 0$ . (Source of figure: [19])

calculated by concerning the field energy and the kinetic energy of the currents as

$$\varepsilon_l = \frac{1}{8\pi} \int (h^2 + \lambda |\text{curl } \mathbf{h}|^2) dS \quad (3.3)$$

$$\approx \left( \frac{\phi_0}{4\pi\lambda} \right)^2 \ln \kappa. \quad (3.4)$$

Here we neglect the core.

### 3.2 Bean's Critical state model

We set the magnetic field direction  $\mathbf{H}$  as  $\hat{z}$  axis. By creating vortices into a superconductor, the surface energy is gained, while the condensation energy is lost. First, consider the interaction between a single vortex (sv) and a defect. If the vortex sits on a defect in the superconductor, the loss of the condensation energy is minimized compared with sitting outside the defect. This is why the vortex-defect interaction is attractive in contrast to the vortex-vortex repulsive interaction. Next, we examine the interaction between the vortex and the screening current. The vortex is parallel to the direction of the field  $\mathbf{H}$ , while the screening current density  $\mathbf{J}$  is perpendicular to  $\mathbf{H}$ . As a result, the Lorentz force density  $\frac{1}{c} \mathbf{J} \times \phi_0 \hat{z}$  is exerted to the sv. Due to this force, the vortex tends to move perpendicular to  $\mathbf{J}$  with the average velocity of flux lines  $\mathbf{v}$ . This motion induces the electric field  $\mathbf{E} = \frac{1}{c} \mathbf{B} \times \mathbf{v}$ , which is parallel to  $\mathbf{J}$ . This leads to the resistive voltage, and power is dissipated. However, when defects are present in a sample, vortices are trapped by the defects and their motions are disrupted to move. As a result, a superconductor shows a zero resistance even after the penetration of vortices. In such a point of view, those defects are called vortex-pinning centers or pinning sites.

Then, let us consider the situation with many vortices in a superconductor. In a dirty super-

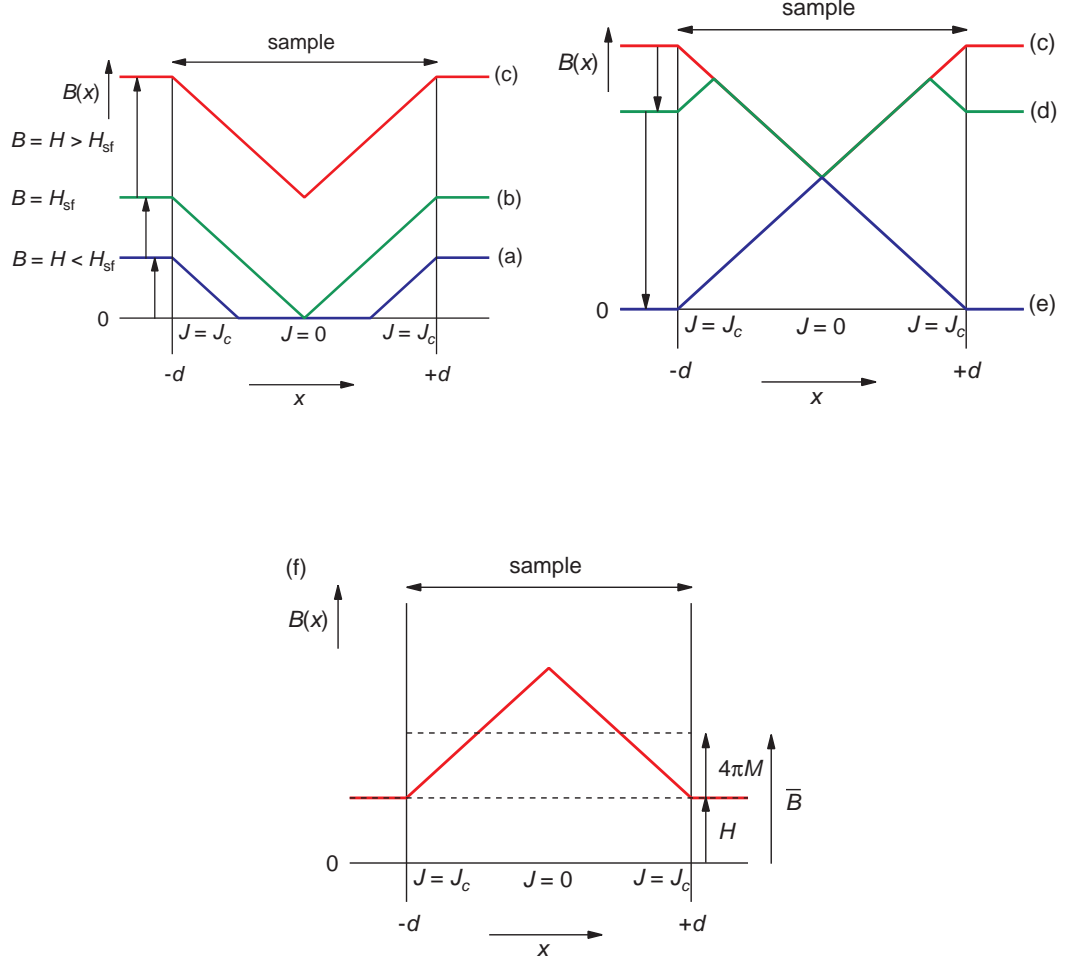


Figure 3.2: (a) The magnetic induction profile  $B(x)$  under the relatively small applied field  $H(< H_{\text{sf}})$ . Outside the sample,  $B = H$ , while inside the sample a straight lines with  $dB/dx = 0$  or a constant slope. Subsequent increase in  $H$  produces the profile of  $B(x)$  under (b)  $H = H_{\text{sf}} = 4\pi J_c d/c$  and (c)  $H > H_{\text{sf}}$ . The field sweeping after reaching to (c) produces  $B(x)$  of (e) under zero field (the remanent state) via the state of (d). (f) The relation among the average  $\bar{B}$ ,  $H$ , and  $4\pi M$ .

conductors, i.e., a superconducting sample containing considerable amount of pinning centers, the distribution of vortices are strongly affected by them. To illustrate such a situation, a phenomenological model is established by Bean [63, 64], which is so-called (Bean's) critical-state model. The concept of the model is the following. Once  $H$  is applied and the vortices penetrate the sample ( $H_{c1}$  is assumed to be zero), the screening current flows at the sample edge. Due to the Lorentz force  $F_L = (1/c)J\phi_0$ , vortices tend to be pushed forward the center of the sample. On the other hand, they are trapped by pinning centers, which disturb the motion of vortices with the pinning force  $F_p$ . First we consider a one-dimensional sample without demagnetization effect located  $-d \leq x \leq +d$ . If the maximal  $F_p$  is higher than  $F_L$ ,  $B(x)$  will substantially drop from  $B = H$  at the sample edge to  $B = 0$  at some point close to the edge. When  $H$  becomes large and the  $F_L$  exceeds the maximum  $F_p$ , the vortices penetrate farther toward the center of the sample, and finally balanced at the condition  $F_L = F_p$ . Hence, when applying magnetic field, the screening current density always has a maximum value of  $J_c = cF_p/\phi_0$  in the flux-penetrated region or zero in the non-penetrated region. After the full penetration, the screening current density reaches the largest value ( $|J| = J_c$ ) in the whole region of the sample. The state is called the Bean's critical state. This unique current density  $J_c$  is called the critical current density, above which ( $J > J_c$ ) zero-resistance state is destroyed by the motion of vortices. According to Maxwell's equation

$$J = \frac{c}{4\pi} \left| \frac{dB}{dx} \right| = J_c. \quad (3.5)$$

Since the Bean's model assumes a field-independent  $J_c$ , the profile of  $B(x)$  is piecewise-linear, as shown in Fig. 3.2(a). With increasing field, the vortices completely penetrate, reaching the center at the self field  $H = H = 4\pi J_c d/c$  (Fig. 3.2(b)). Further increase in the field ( $H > H_{sf}$ ) pushes up the valley structure of  $B(x)$  (Fig. 3.2(c)). As we can see, the magnetic property has a hysteretic character in sweeping field. The irreversible magnetization  $M_{irr}$  (or simply  $M$ ) is related to  $B$  as

$$M = \frac{1}{4\pi} (\overline{B(x)} - H), \quad (3.6)$$

where  $\overline{B(x)} = \frac{1}{2d} \int_{-d}^{+d} B(x) dx$  is the mean value of  $B(x)$ , and the sample is from  $-d$  to  $+d$ , so

that  $J_c$  is estimated by measuring  $M$ . Namely, from Eq. (3.5) and (3.6),

$$\overline{B(x)} - H = \frac{4\pi}{c} \int_{-d}^{+d} B(x) dx - H \quad (3.7)$$

$$= \frac{2\pi}{c} J_c d \quad (3.8)$$

$$= 4\pi M \quad (3.9)$$

$$\Rightarrow M = \frac{J_c d}{2c}. \quad (3.10)$$

Therefore, we have

$$J_c = \frac{2c}{d} M. \quad (3.11)$$

In order to adopt the practical unit such as A/cm<sup>2</sup> in  $J$ , cm in dimension, and emu/cm<sup>3</sup> in  $M$ ,  $c = 10$  is substituted. The hysteresis loop is depicted in Fig. 3.3. Since the flux enters or exits from the edge, and  $B(\pm d)$  equals to the applied field  $H$ , the evolution of the profile  $B(x)$  is identified only at the sample edge in the initial slope or at the beginning of changing the field-sweeping direction.

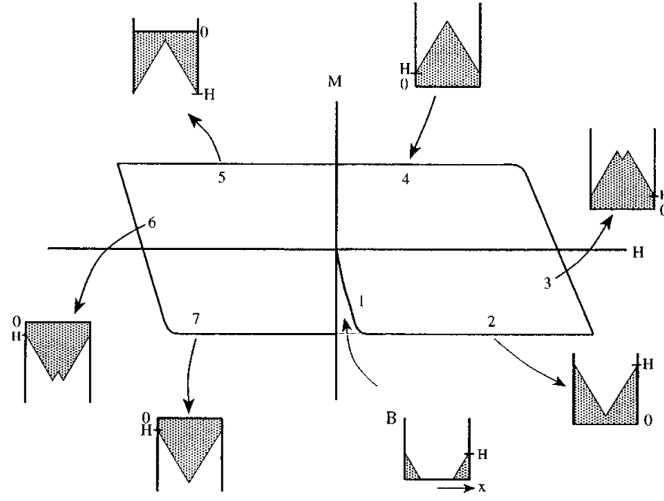


Figure 3.3: The hysteresis loop of a dirty superconductor according to the Bean's model. (Source of figure: [20])

In the three-dimensional case, the area  $\int_{-d}^{+d} B(x) dx$  is modified to the volume of the roof-top pattern in Fig. 3.4. Then  $J_c$  is practically estimated as

$$J_c = \frac{40M}{a(1 - a/3b)}, \quad (3.12)$$

where  $a$  and  $b(\geq a)$  are the lateral dimension of the sample, and  $c = 10$  is adopted.

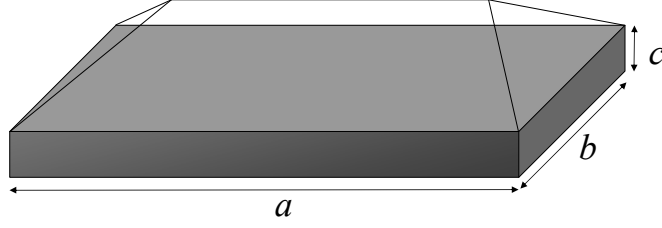


Figure 3.4: The rooftop pattern of  $B$  in three-dimensional Bean's model. The volume of the rooftop pattern is related to  $M$ .

### 3.3 Weak-collective pinning

When the vortex system forces from the weak and dense pinning centers, the weak-collective pinning theory works [65, 21]. The pinning force density acting on the flux lines per unit volume,  $F_p = (1/c)J_c B$ , is the result of the accumulation of individual pinning forces, which depends on the elementary pinning force  $f_p$  and the density of pins  $n_p$ , as well as the flux density to be pinned, namely, the magnetic inductance  $B$ . In general,  $F_p$  tends to increase when  $f_p$  and  $n_p$  becomes large, although their dependence is considerably complex. In contrast to the strong pinning, where  $F_p$  is evaluated by the direct summation, the pinning forces in the case of randomly distributed weak pins are canceled out due to the elastic interaction among flux lines. That is, the mutually repulsive flux lines are not always placed at the optimal position for the pinning. This is in sharp contrast to the strong pinning, where the compensation of pinning force is small since the elastic interaction among flux lines is negligible.

The collective pinning and creep of flux-line lattice are quite difficult to fully understand due to their complexity. The main reason is that there are many length scales to precisely describe the phenomena. The smallest length scale is the coherence length  $\xi$ , which describe the extent of the vortex core coupled with the pinning potential. The next small scale is the vortex-vortex distance  $a_0$ . This scale determines the interaction among vortices themselves, so that it is related to the collectively pinned vortex bundle. The concept of the vortex bundle is described below. This also determines the internal structure of an elastic medium composed of the discrete flux-line lattice. The internal structure has an effect to the phase transition of the vortex matter, such as the melting. The third length scale is the penetration depth  $\lambda$ , which



define the range of the interaction among vortices. Therefore this plays a role of adjusting a vortex bundle size. At elevating temperatures, the fourth intermediate length scale, locating between  $\xi$  and  $a_0$ , becomes relevant, i.e., the thermal displacement of each vortex  $< u^2 >_{\text{th}}^{1/2}$ . This has the thermal smearing effect on the vortex core.

The free energy  $F$  associated with distortions of flux-line lattice induced by randomly distributed weak pins is

$$F = \int d^3r \left[ \frac{c_{11}}{2} (\nabla \cdot \mathbf{u})^2 + \frac{c_{66}}{2} (\nabla_{\perp} \cdot \mathbf{u})^2 + \frac{c_{44}}{2} (\partial_z \mathbf{u})^2 + U_{\text{pin}}(\mathbf{r}, \mathbf{u}) - \mathbf{F}_L \cdot \mathbf{u} \right], \quad (3.13)$$

where the two-dimensional vector  $\mathbf{u}(\mathbf{r})$  describes a local displacement of flux-line lattices;  $c_{11}$ ,  $c_{44}$ , and  $c_{66}$  are bulk, tilt, and shear elasticity modulus, respectively;  $U_{\text{pin}}(\mathbf{r}, \mathbf{u})$  is the random potential describing the lattice interaction with defects. When the pinning is weak, the elastic force dominates rather than pinning force. In this case, we face the problem of statistical summation of elementary pinning force  $f_p$ . When accounting the pinning force density, the average  $< f_{\text{pin}} >$  disappears for weak pinning sites. Hence the pinning is induced by the local fluctuation of pinning site density. Considering the pinning sites with each pinning force  $f_p$ , a density  $n_p$ , and the range of pinning potential  $r_p \sim \xi$ , the summed pinning energy is given by

$$< \varepsilon_{\text{pin}}^2(V) >^{1/2} \approx [f_p^2 n_p (\xi/a_0)^2 V]^{1/2} \xi. \quad (3.14)$$

This equation can be led as following. Since the average of the weak pinning force  $f_p$  is canceled out to be zero, the second order term becomes relevant. We sum them by multiplying the number of defects  $n_p V$ , where  $V$  is the volume of the system. The factor  $(\xi/a_0)^2$  is to account for the volume of vortex core, only which is pinned instead of the whole vortex. Finally, with multiplying the characteristic length scale  $\xi$ , the total pinning energy is obtained to convert the total pinning force to the energy. In a realistic case, the elastic interaction distance of flux-line lattice is finite, as Larkin and Ovchinnikov pointed out, so that the discussion above is appropriate in the condition fulfilled. Let us consider the correlation volume  $V_c$  with the length along the field direction  $\sim L_c$  and the length perpendicular to field  $\sim R_c$ , in which the flux-line lattice does not distorted, and the pinning-induced distortion of shear  $c_{66}$  and tilt  $c_{44}$  occurs among them. Accordingly, each volume of  $V_c$  is independently pinned with the pinning energy

of  $U_c = \langle \varepsilon_{\text{pin}}^2(V_c) \rangle^{1/2}$  and the pinning force density is then written as

$$F_{\text{pin}} \sim U_c/V_c r_p \sim [f_p^2 n_p (\xi/a_0)^2/V_c]^{1/2}. \quad (3.15)$$

Since this balances with the Lorentz force density  $J_c B/c$ , we can obtain the critical current density  $J_c \sim c F_{\text{pin}}/B$ .

Now we go back to an isolated vortex (1D) problem. By comparing the elastic energy  $\varepsilon_0 \xi^2/L_c$  and the pinning energy  $U_c = (f_p^2 n_p L_c \xi^2)^{1/2} \xi$ , the collective pinning length is determined as following:

$$\frac{\varepsilon_0 \xi^2}{L_c} = (f_p^2 n_p L_c \xi^2)^{1/2} \xi \quad (3.16)$$

$$\varepsilon_0^2 = f_p^2 n_p L_c^3 \quad (3.17)$$

$$L_c = \left( \frac{\varepsilon_0^2}{f_p^2 n_p} \right)^{1/3}. \quad (3.18)$$

Thus, the critical current density is calculated as

$$j_c = c F_{\text{pin}}/B \quad (3.19)$$

$$= \frac{c}{B} \frac{U_c}{V_c r_p} \Big|_{\text{dp}} \quad (3.20)$$

$$= \frac{c}{B} \frac{(f_p^2 n_p (\xi/a_0)^2 V_c)^{1/2} \xi}{V_c \xi} \Big|_{\text{dp}} \quad (3.21)$$

$$= \frac{c}{B} \left[ f_p^2 n_p \frac{\xi^2}{a_0^4 L_c} \right]^{1/2} \quad (3.22)$$

$$= \frac{c \varepsilon_0}{B a_0^2 \xi} \left[ f_p^2 n_p \frac{\xi^4}{(\frac{\varepsilon_0^2}{f_p^2 n_p})^{1/3} \varepsilon_0^2} \right]^{1/2} \quad (3.23)$$

$$= j_0 \left[ \left( \frac{f_p^2 n_p \xi^4}{\varepsilon_0^2} \right)^3 \left( \frac{f_p^2 n_p}{\varepsilon_0^2} \right) \right]^{1/6} \quad (3.24)$$

$$= j_0 (n_p^4 \xi^{12} f_p^8 / \varepsilon_0^8)^{1/6} \quad (3.25)$$

$$= j_0 (n_p \xi^3 f_p^2 / \varepsilon_0^2)^{2/3}. \quad (3.26)$$

Here we express in terms of the depairing current density  $j_0 \sim c \varepsilon_0 / \phi_0 \xi$ .

Now we move on to the pinning of the vortex bundle. We put “*b*” to distinguish from sv

case if necessary. The discussion below is appropriate as long as

$$\langle u^2(R_c) \rangle \simeq \xi^2, \quad \langle u^2(L_c^b) \rangle \simeq \xi^2 \quad (3.27)$$

are applicable. We apply the current condition to the general expression introduced by Larkin-Ovchinnikov

$$\langle u^2(\mathbf{r}) \rangle \simeq \xi^2 \left( \frac{a_0}{L_c} \right)^3 \left[ \left( \frac{R^2}{\lambda^2} + \frac{a_0^2 L^2}{\lambda^4} \right)^{1/2} + \ln \left( 1 + \frac{R^2}{a_0^2} + \frac{L}{a_0} \right) \right], \quad u < \xi, a_0 < L_c. \quad (3.28)$$

When the 2nd term is relevant, i.e., in the short length scale,

$$R_c \simeq a_0 \exp \left[ \tilde{c} \left( \frac{L_c}{a_0} \right)^3 \right], \quad a_0 < R_c < \lambda \quad (3.29)$$

$$L_c^b \simeq \frac{R_c^2}{a_0}, \quad a_0 < L_c^b < \frac{\lambda^2}{a_0} \quad (3.30)$$

are obtained, where  $\tilde{c}$  is a constant of order unity. On the other hand, in the region that the 1st term is relevant, i.e., in large length scale,

$$R_c \simeq \lambda \left( \frac{L_c}{a_0} \right)^3, \quad \lambda < R_c \quad (3.31)$$

$$L_c^b \simeq \frac{\lambda}{a_0} R_c, \quad \frac{\lambda^2}{a_0} < L_c^b \quad (3.32)$$

are obtained. The pinning energy is summarized in the following. In the sv regime, it is written by the elastic energy as

$$U_{sv} = \varepsilon_0 \xi^2 / L_c \simeq H_c^2 \xi^3 \frac{\xi}{L_c}, \quad L_c < a_0, \quad (3.33)$$

where  $H_c = \Phi_0 / 2\sqrt{2}\pi\lambda\xi$  is the thermodynamic critical field. At the equilibrium state, the energy of tilt, shear, and pinning are equal, so that we use the shear energy here. Concerning the elastic domain, characterized by the scale  $R_c$  with the displacement of  $u \sim \xi$ , we have

$$U_c \simeq c_{66} \left( \frac{\xi}{R_c} \right)^2 V_c. \quad (3.34)$$

Here  $c_{66}$  is given by  $\phi_0 B / (8\pi\lambda)^2$ . Using Eq. (3.29) and (3.30), it leads

$$U_c \simeq c_{66} \left( \frac{\xi}{R_c} \right)^2 V_c \quad (3.35)$$

$$\simeq c_{66} \xi^2 L_c^b \quad (3.36)$$

$$\simeq c_{66} \xi^2 \frac{R_c^2}{a_0} \quad (3.37)$$

$$\simeq \frac{\Phi_0 B}{(8\pi\lambda)^2} \frac{\xi^2}{a_0} a_0^2 \exp \left( 2\tilde{c} \left( \frac{L_c}{a_0} \right)^3 \right) \quad (3.38)$$

$$= H_c^2 \frac{8\pi^2 \lambda^2 \xi^2}{\Phi_0^2} \frac{\Phi_0 B}{(8\pi\lambda)^2} \xi^2 a_0 \exp \left( 2\tilde{c} \left( \frac{L_c}{a_0} \right)^3 \right) \quad (3.39)$$

$$\simeq H_c^2 \frac{\xi^4 B a_0^2}{\Phi_0} \frac{1}{a_0} \exp \left( 2\tilde{c} \left( \frac{L_c}{a_0} \right)^3 \right) \quad (3.40)$$

$$= U_{sv} \frac{L_c}{a_0} \exp \left( 2\tilde{c} \left( \frac{L_c}{a_0} \right)^3 \right), L_c [\ln(\lambda/L_c)/\tilde{c}]^{-1/3} < a_0 < L_c \quad (3.41)$$

In the case of Eq. (3.31) and (3.32),

$$U_c \simeq c_{66} \xi^2 L_c^b \quad (3.42)$$

$$\simeq c_{66} \xi^2 \frac{\lambda}{a_0} R_c \quad (3.43)$$

$$\simeq c_{66} \xi^2 \frac{\lambda^2}{a_0} \left( \frac{L_c}{a_0} \right)^3 \quad (3.44)$$

$$\simeq H_c^2 \frac{8\pi^2 \lambda^2 \xi^2}{\Phi_0^2} \frac{\Phi_0 B}{(8\pi\lambda)^2} \xi^2 \frac{\lambda^2}{a_0} \left( \frac{L_c}{a_0} \right)^3 \quad (3.45)$$

$$\simeq H_c^2 \frac{\xi^2 \lambda^2}{a_0^3} \left( \frac{L_c}{a_0} \right)^3 \quad (3.46)$$

$$= U_{sv} \left( \frac{\lambda}{a_0} \right)^2 \left( \frac{L_c}{a_0} \right)^4, a_0 < L_c [\ln(\lambda/L_c)/\tilde{c}]^{-1/3} \quad (3.47)$$

is obtained. The critical current density  $J_c$  is given by

$$j_c \simeq \frac{c}{B} \frac{U_c}{V_c \xi} \quad (3.48)$$

$$\simeq \frac{c}{B} (c_{66}/\xi) \left( \frac{\xi}{R_c} \right)^2 \quad (3.49)$$

$$= j_0 \left( \frac{\xi}{R_c} \right)^2 \frac{a_0^2}{\varepsilon_0} c_{66} \quad (3.50)$$

$$\simeq j_0 \left( \frac{\xi}{R_c} \right)^2. \quad (3.51)$$

First we examine the critical current density for sv. From Eq. (3.18) and (3.26),

$$j_{\text{sv}} \simeq \frac{\xi^2}{L_c^2} j_0, \quad L_c < a_0 \quad (3.52)$$

is obtained. Substituting Eq. (3.29) into Eq. (3.51), we have

$$j_c \simeq \frac{\xi^2}{a_0^2} j_0 \exp \left( -2\tilde{c} \left( \frac{L_c}{a_0} \right)^3 \right) \quad (3.53)$$

$$= \frac{\xi^2}{L_c^2} j_0 \left( \frac{L_c}{a_0} \right)^2 \exp \left( -2\tilde{c} \left( \frac{L_c}{a_0} \right)^3 \right) \quad (3.54)$$

$$= j_{\text{sv}} \left( \frac{L_c}{a_0} \right)^2 \exp \left( -2\tilde{c} \left( \frac{L_c}{a_0} \right)^3 \right). \quad (3.55)$$

On the other hand, with Eq. (3.31),

$$j_c \simeq \frac{\xi^2}{\lambda^2} \left( \frac{a_0}{L_c} \right)^6 j_0 \quad (3.56)$$

$$= j_{\text{sv}} \frac{a_0^2}{\lambda^2} \left( \frac{a_0}{L_c} \right)^4 \quad (3.57)$$

is obtained. Summarizing the results above,  $J_c$  as a function of  $B = \phi_0/a_0^2$  in the weak-collective pinning theory behaves the following way.:

$$\text{sv} \quad j_c/j_{\text{sv}} \sim \text{const.}$$

$$\text{sb} \quad j_c/j_{\text{sv}} \propto B \exp[-B^{3/2}]$$

$$\text{lb} \quad j_c/j_{\text{sv}} \propto B^{-3}$$

These behaviors are summarized in Fig. 3.5.

### 3.4 Sparse strong-point pinning

By contrast, in the strong pinning theory,  $J_c$  behaves as

$$j_c^s(0) = \frac{\pi^{1/2} n_i^{1/2} j_0}{\varepsilon_\lambda} \left( \frac{f_{p,s} \xi_{ab}}{\varepsilon_0} \right)^{3/2} (B < B^*) \quad (3.58)$$

$$j_c^s(B) \approx \frac{2n_i j_0}{\varepsilon_\lambda^{5/4} \xi_{ab}^{1/2}} \left( \frac{f_{p,s} \xi_{ab}}{\varepsilon_0} \right)^{9/4} \left( \frac{\Phi_0}{B} \right)^{5/8} (B > B^*), \quad (3.59)$$

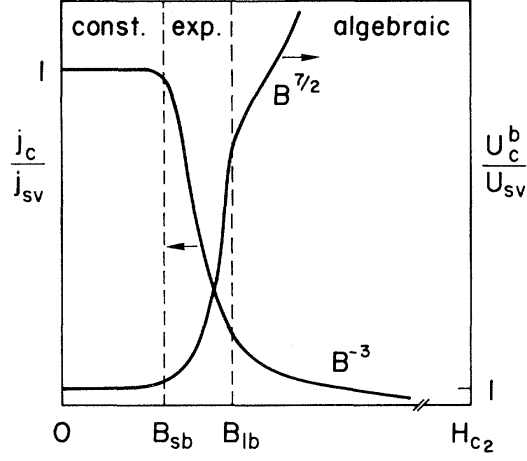


Figure 3.5: The field dependence of the critical current density  $J_c$  in the framework of the weak-collective pinning theory. For low field, the interaction between the vortices is irrelevant and  $j_c$  does not depend on the magnetic field. Within the small-bundle pinning regime, the critical current density decreases exponentially. Finally, in the large-bundle pinning regime, the field dependence of  $j_c$  turns algebraic, with  $j_c \propto B^{-3}$ . (Source of figure: [21])

where  $B^* = 0.74\epsilon_\lambda^{-2}\Phi_0(n_i/\xi_{ab})^{4/5}(f_{p,s}\xi_{ab}/\epsilon_0)^{6/5}$ . This power-law behavior  $J_c \propto B^{-\alpha}$  with  $\alpha \sim 1/2$  is experimentally confirmed in  $\text{YBa}_2\text{Cu}_3\text{O}_{7-\delta}$  film [66] and IBSs [67].

It is noteworthy that the vortex pinning is used to probe the defects included to a superconductor [67]. If atomic size defects are included, they contribute to the weak-collective pinning, while nm-sized defects work as strong pinning sites. Assuming  $J_c$  is the sum of  $J_{\text{coll}}$  and  $J_c^s$ , where  $J_{\text{coll}}$  is  $J_c$  only weak pins are included, and analogously  $J_c^s$  with only strong pins, we can deduce the density of each type of defects. Further studies of vortex pinning will provide a strong tool to identify the defect morphology and amount included in a superconductor.

### 3.5 Flux-pinning mechanism

In the discussion above, we have set the pinning potential without considering what is the origin of it. Here we briefly review the representative pinning mechanism of  $\delta T_c$  pinning and  $\delta l$  pinning [68].

**$\delta T_c$  pinning** The pinning originated from the fluctuation of  $T_c$ , which is accompanied by the impurities in some cases. The temperature dependence of  $J_c$  is

$$J_c(t) = (1 - t^2)^{7/6}(1 + t^2)^{5/6}$$

**$\delta l$  pinning** The pinning originated from the fluctuation of the mean-free path  $l$ , accompanied

by the microscopic inhomogeneity of dopant atoms. The temperature dependence of  $J_c$  is  $J(t) = (1 - t^2)^{5/2}(1 + t^2)^{-1/2}$

Here we adopt the reduced temperature  $t = T/T_c$ . These are led by  $j_c = j_0 \delta^{2/3} \varepsilon^{-2/3}$ , where  $j_0 = 4B_c/3\sqrt{6}\mu_0\lambda \propto (1 - t^2)$  is the depairing current density,  $\varepsilon < 1$  is mass anisotropy, and  $\delta$  is disorder parameter. In  $\delta T_c$  pinning and  $\delta l$  pinning,  $\delta \propto \xi$  and  $\delta \propto \xi^{-3}$  are assumed, respectively.

### 3.6 Flux creep in Anderson-Kim model

Up to now, we neglect the hopping probability of vortices among pinning sites. This is valid at  $T = 0$  K, apart from quantum tunneling. At the finite temperature, the vortex system is expected to undergo the relaxation process toward the equilibrium state, where the uniform distribution of vortices  $B(\mathbf{r}) = B$  is realized. We start from the critical state, which is a nonequilibrium state. When the vortex is thermally excited to escape from the pinning potential  $U$ , the hopping time  $t$  is described as

$$t = t_{\text{eff}} \exp(U/kT) \quad (3.60)$$

where  $t_{\text{eff}}$ ,  $k$  and  $T$  are the vortex hopping attempt time, the Boltzmann constant and temperature, respectively.  $t_{\text{eff}}$  is of the order of  $10^{-6}$  s. The driving force of the hopping process is the Lorentz force density  $\mathbf{F} = (1/c)\mathbf{J} \times \mathbf{B}$ . For simplicity, we consider only the hopping direction due to this force. Thus  $U$  takes the form of

$$U = U_0 - \frac{1}{c}JBx_0V \quad (3.61)$$

where  $V$  is the volume of the hopping flux, and  $x_0$  is the hopping distance. The second term is the work by the Lorentz force. With an assumption of constant  $V$  and  $x_0$ , independent of  $J$  and  $B$ ,  $U$  is linearly related to  $J$ , taking the form of

$$U = U_0[1 - J/J_{c0}] \quad (3.62)$$

where  $J_{c0} = cU_0/Bx_0V$  is the critical current density without thermally excited hopping. Since the Eq. (3.60) is rewritten as

$$U(J) = kT \ln(t/t_{\text{eff}}), \quad (3.63)$$

Eq. (3.62) and Eq. (3.63) lead to the classical flux-creep formula:

$$J = J_{c0} \left[ 1 - \frac{kT}{U_0} \ln \left( \frac{t}{t_{\text{eff}}} \right) \right]. \quad (3.64)$$

In evaluating the magnitude of the relaxation, the normalized relaxation rate

$$S \equiv \frac{d \ln M_{\text{irr}}}{d \ln t} = \frac{d \ln J}{d \ln t} \quad (3.65)$$

is useful to introduce, which enables us to reduce the parameters of  $J_{c0}$ ,  $U_0$ , and  $t_{\text{eff}}$ . Here  $M \propto J$  is utilized. In the Anderson-Kim model, with Eq. (3.64), we are able to evaluate

$$S = \frac{kT}{U_0 - kT \ln(t/t_{\text{eff}})} \quad (3.66)$$

or because of  $U_0 \gg kT$  in a low-temperature superconductor,

$$S = \frac{kT}{U_0} \quad (3.67)$$

Again taking  $U_0 \gg kT$  into account, the value of  $S$  should be very small, concluding that the effect of creep in low-temperature superconductors is negligible. Therefore, we can extract the pinning energy  $U_0$  by evaluating the normalized relaxation rate  $S$  in the Anderson-Kim model. By contrast, in high-temperature superconductors,  $U \ll kT$  can be satisfied, which is one of the reasons for existing the large flux creep.

### 3.7 Collective creep and vortex-glass theory

The general formalism is to introduce the nonlinearity in  $U(J)$ . Namely, the inverse-power-law barrier

$$U = \frac{U_0}{\mu} [(J_{c0}/J)^\mu - 1] \quad (3.68)$$

is assumed. Here  $\mu$  is called the glassy exponent. The special case is found in  $\mu = -1$ , which corresponds to the Anderson-Kim model. The important point is found in the case of positive  $\mu$ , which has the peculiar property of diverging  $U$  as  $J \rightarrow 0$ . Combining Eq. (3.63) and Eq. (3.68),



we derive the fundamental equation in the collective creep model

$$\frac{U_0}{\mu} [(J_{c0}/J)^\mu - 1] = kt \ln \left( \frac{t}{t_{\text{eff}}} \right) \quad (3.69)$$

$$\Leftrightarrow \left( \frac{J_{c0}}{J} \right)^\mu = 1 + \frac{\mu kT}{U_0} \ln \left( \frac{t}{t_{\text{eff}}} \right) \quad (3.70)$$

$$\Leftrightarrow J = \frac{J_{c0}}{[1 + (\mu kT/U_0) \ln(t/t_{\text{eff}})]^{1/\mu}}, \quad (3.71)$$

which is the so-called interpolation formula. In contrast to the classical theory, the volume of activated flux bundle is supposed to depend on  $J$ , and at  $J \rightarrow 0$ ,  $U$  becomes infinitely large and the vortex system is frozen, which corresponds to the equilibrium state. Interestingly, the interpolation formula Eq. (3.71) were derived on the basis of the vortex glass theory. In this model, the vortex system has a "vortex glass" phase apart from the vortex liquid phase in high-temperature and high-field region, and forms a metastable state due to vortex-defect interactions and vortex-vortex interactions. In addition,  $\mu$  and the bundle size are predicted to be field- and temperature-dependent. In three-dimensions, the following values are predicted.

- $\mu = 1/7$  in the low-field, low-temperature region, where the creep is predominantly characterized by the individual flux motion
- $\mu = 5/2$  in higher temperatures and fields, where the collective creep of small bundle dominates
- $\mu = 7/9$  in higher temperatures and fields, where the bundle size is much larger than the London penetration depth

According to Eq. (3.71), the normalized relaxation rate in the collective creep is written as

$$S = \frac{kT}{U_0 + \mu kT \ln(t/t_{\text{eff}})}. \quad (3.72)$$

The most intriguing result in this formula is observed at high temperature. Since  $U_0 \ll kT$  can be realized in high-temperature superconductors, we can simplify Eq. (3.72) as

$$S = \frac{1}{\mu \ln(t/t_{\text{eff}})}. \quad (3.73)$$

Unless  $\mu$  has a temperature dependence or  $t_{\text{eff}}$  is highly dependent on temperature, this leads to the presence of the plateau in  $S(T)$  at high temperatures. This was actually observed in  $\text{YBa}_2\text{Cu}_3\text{O}_{7-\delta}$  or other cuprate superconductors, where the prominent plateau structure instead of  $S \propto T$  is observed at intermediate temperatures.

The detail of vortex state is investigated by flux dynamics. The vortex dynamics is determined by vortex-vortex interactions, as well as vortex-defect interactions. At higher fields, where the density of vortices becomes high, the interaction among vortices is strong, resulting in the flux creep as a unit of vortex bundle, instead of a single vortex. The small bundle suppresses the flux creep, so if we control the field applied to superconductors, we can minimize the reduction of the persistent current density, which is important to realize the superconducting wire with high persistent current stable over time. *The vortex state is characterized by the glassy exponent  $\mu$ , so that it is important to determine the  $\mu$  in each temperature and field region.*

### 3.8 Vortices in as-grown $\text{YBa}_2\text{Cu}_3\text{O}_{7-\delta}$ and iron-based superconductors

Most of the studies on the vortex pinning and creep have been performed in  $\text{YBa}_2\text{Cu}_3\text{O}_{7-\delta}$  (YBCO) and  $\text{Bi}_2\text{Sr}_2\text{CaCu}_2\text{O}_{8+\delta}$  (BSCCO). BSCCO is, in a sense, quite different from YBCO, since vortex system in BSCCO is two-dimensional due to the anisotropy of BSCCO with  $\gamma \sim 50 - 100$  (see section 2.3), whereas YBCO is three-dimensional system with  $\gamma \sim 5 - 7$ . Before we focus on IBSs later, we summarize the vortex properties in YBCO. Figure 3.6 is the magnetic hysteresis loops at several temperatures under  $\mathbf{H}$  parallel to  $c$ -axis in YBCO with  $T_c = 93$  K. At low temperatures, the width of the loop,  $\Delta M(H)$  is field independent in the high-field limit, while there is a central peak at low fields. As  $T$  increases, the general trend is similar at high-field limit and the central peak, but a new feature is observed at intermediate field. Namely, the nonmonotonic field dependence of  $\Delta M(H)$  is identified. This broad peak structure is called “fish-tail effect“. This structure is more prominent at higher temperatures ( $T = 70$  K). The fish-tail effect has been observed also in some IBSs [69, 24, 70]. Although some mechanism for the origin of fish-tail effect, such as weak-collective pinning [71] and the crossover from elastic creep to plastic creep [69], a complete understanding of this phenomenon has not been achieved.

The persistent current density ( $J$ ) is calculated from hysteresis loop via the Bean’s critical

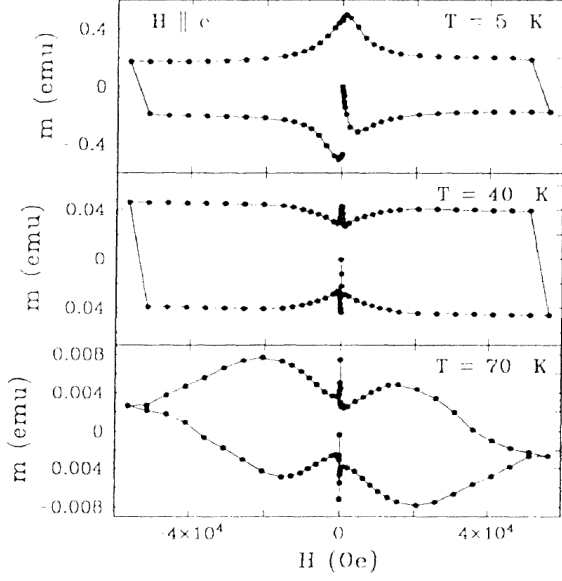


Figure 3.6: Magnetic hysteresis loops in  $\text{YBa}_2\text{Cu}_3\text{O}_{7-\delta}$  at several temperatures. (Source of figure: [22])

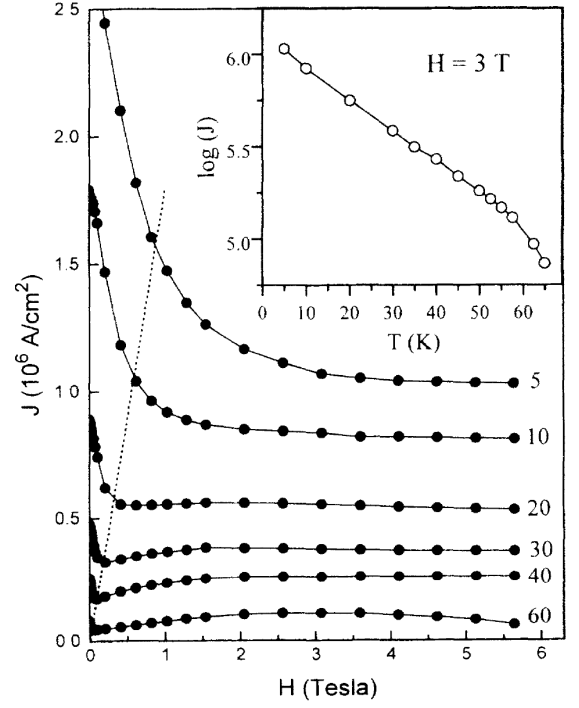


Figure 3.7: Field dependence of the persistent current density at several temperatures obtained from magnetization loops with the help of Bean's critical state model. Inset: the temperature dependence of the persistent current density at  $H = 3$  T. (Source of figure: [23])

state model. Figure 3.7 shows the field dependence of  $J$  at several temperatures in YBCO. Both the central peak and the fish-tail effect are clearly observed around  $H = 0$  and at intermediate fields, respectively. From these data, we can extract the temperature dependence of  $\log J$  at  $H = 3$  T, where a linear decrease is observed apart from high temperatures. Such an exponential decrease of  $J$  is also observed in IBSs [72].

YBCO provides a stage to examine the weak-collective pinning, since the oxygen vacancies in YBCO is expected to work as weak-pinning centers. The weak-collective pinning character, as seen in Fig. 3.5, is indeed observed in Fig. 3.8. In the high-field region, we can clearly see  $H^{-3}$  dependence in  $J$ , as predicted in the weak-collective pinning theory. This manifests that atomic size defects are included in YBCO and indeed work as weak-pinning centers, as well as the small vortex bundle is formed in this field region.

Flux dynamics is investigated in YBCO from the flux creep experiment. Figure 3.9(b) shows the field dependence of  $S$  at  $T = 40$  K in YBCO. At low fields,  $S$  is relatively large value of

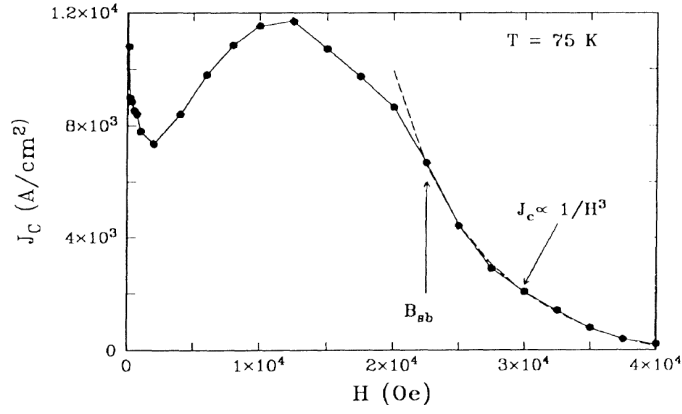


Figure 3.8: The field dependence of the critical current density at  $T = 75$  K in  $\text{YBa}_2\text{Cu}_3\text{O}_{7-\delta}$ . (Source of figure: [22])

$S \simeq 0.07$ , which is suppressed by increasing  $H$  to the value of 0.02-0.04. Figure 3.9(a) shows the field dependence of  $J$  at the same temperature. These two images are the mirror images of each other, indicating that the measured  $J$  is crucially affected by the flux relaxation. Namely, the measured  $J$  is not the true critical current density  $J_c$  in high-temperature superconductors. The long-term-relaxation measurements extract the glassy exponent  $\mu$ , as shown in 3.9(c). The prediction in the vortex-glass theory, the field dependence of  $\mu$  from  $1/7$  to  $5/2$  to  $7/9$  as  $H$  increases, well describes the experimental change in  $S$  from 0.16 at  $H \simeq 0.1$  T to 1.42 at  $H \simeq 1$  T. Each vortex bundle regime is summarized in Fig. 3.10.

The detailed studies of the temperature dependence of  $J$  and  $S$  show the validity of the collective creep theory. Figure 3.11 and 3.12 show the temperature dependence of  $J$  and  $S$ , respectively, both of which are well explained by the collective creep theory with Eq. (3.71) and Eq. (3.72). The dependence on the defect density is examined by the 3-MeV proton-irradiation with a dose of  $1 \times 10^{16}$  ions/cm<sup>2</sup>, which introduces random point defects. As also shown in Fig. 3.11 and 3.12, the sample after proton irradiation also shows the collective-creep behavior with the enhancement of  $J$  and the suppression of  $S$ . This leads to the evaluation of the change of vortex state in the framework of the collective creep theory. The vortex state is characterized by the true critical current density  $J_c$  and the glassy exponent  $\mu$ . With an introduction of point defects, it is expected that  $J_c$  is enhanced, while the value of  $\mu$  stays nearly constant due to the difficulty of the change in vortex-defect and vortex-vortex interactions. To deduce the parameters related to the vortex state, Thompson *et al.* utilize the Maley's method taking the temperature dependence of the vortex-pinning energy  $U(T)$  into account [1]. The Maley's

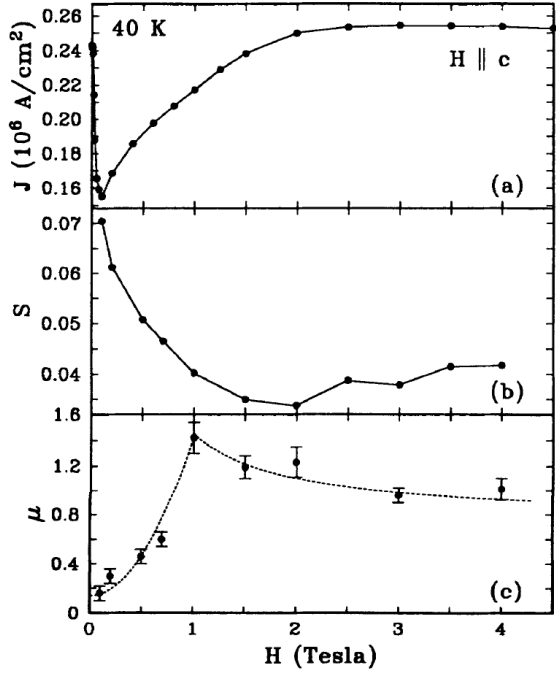


Figure 3.9: Field dependence of (a) the screening current density  $J$ , (b) the relaxation rate  $S$ , and (c) the glassy exponent  $\mu$  at  $T = 40$  K in  $\text{YBa}_2\text{Cu}_3\text{O}_{7-\delta}$ . (Source of figure: [23])

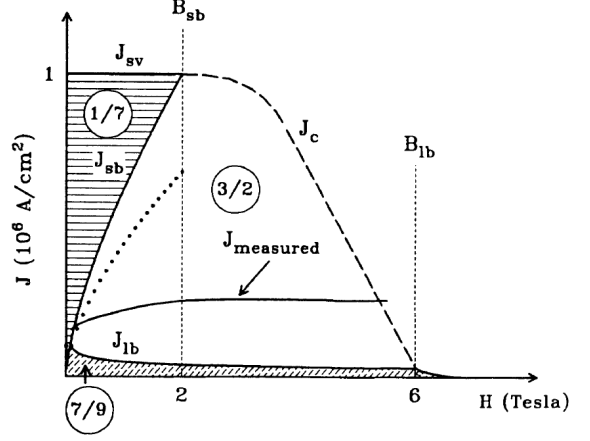


Figure 3.10: The vortex-bundle regime in each  $H$  and  $J$  region. (Source of figure: [23])

method [73] is based on the master rate equation

$$dM/dt = (B\omega a/2\pi r) \exp(-U/T), \quad (3.74)$$

where  $M$  is the magnetization,  $t$  is time from the critical state is created,  $B$  is the magnetic induction,  $\omega$  is the attempt frequency for vortex hopping,  $a$  is the hopping distance,  $r$  is the sample radius, and energies are measured in K. Solving  $U$  for the net pinning barrier  $U$  gives

$$U = -T[\ln(dM/dt) - C], \quad (3.75)$$

with  $C = \ln(B\omega a/2\pi r)$ . By selecting a suitable  $C$ ,  $U$  is scaled by the screening current density  $J$ , as in Eq. (3.68), and we can deduce the glassy exponent  $\mu$  and  $J_{c0}$ . However,  $U$  is assumed to be constant even at high temperatures, the direct plot of  $U(J)$  in a wide range of temperature would fail, since the smearing of the pinning barrier  $U$  is not negligible in high-temperature superconductors. To eliminate this effect,  $U/g(T)$  should be considered, instead of  $U$  itself, where  $g(T)$  is often assumed as  $[1 - (T/T_c)^p]^n$ . In Ref. [1],  $p = 2$  and  $n = 3/2$  are chosen. The

Maley's plot in YBCO is shown in Fig. 3.13, and the summary of the parameters are shown in Table 3.1.

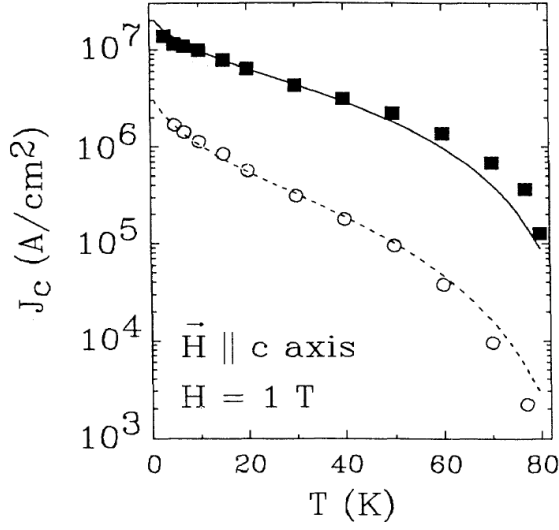


Figure 3.11: The temperature dependence of the screening current density  $J$  at  $H = 1$  T in  $\text{YBa}_2\text{Cu}_3\text{O}_{7-\delta}$ . The open and closed symbols are before and after proton irradiation with a dose of  $1 \times 10^{16}$  ions/cm<sup>2</sup>. Lines are fits to Eq. (3.71). (Source of figure: [1])

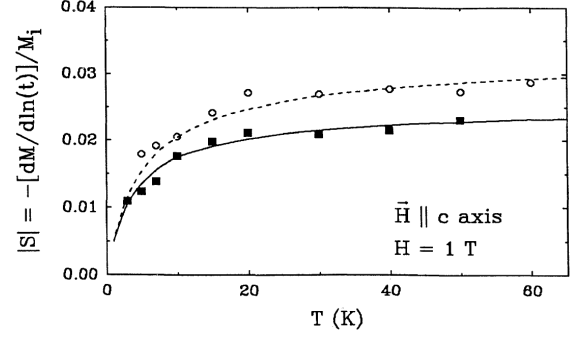


Figure 3.12: The temperature dependence of the normalized relaxation rate  $S$  at  $H = 1$  T in  $\text{YBa}_2\text{Cu}_3\text{O}_{7-\delta}$ . The open and closed symbols are before and after proton irradiation with a dose of  $1 \times 10^{16}$  ions/cm<sup>2</sup>. Lines are fits to Eq. (3.72). (Source of figure: [1])

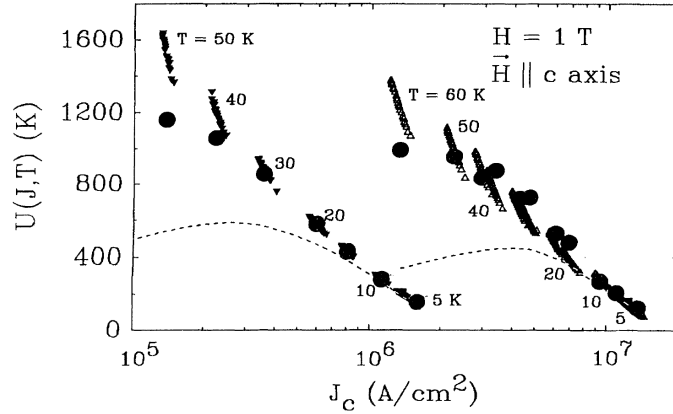


Figure 3.13: Maley's plot under  $H = 1$  T parallel to  $c$ -axis in  $\text{YBa}_2\text{Cu}_3\text{O}_{7-\delta}$ . (Source of figure: [1])

These studies are done also in IBSs [24, 70]. In Ref. [70],  $U$  is independently scaled at three different field regions,  $H < H_{\text{on}}$ ,  $H_{\text{on}} < H < H_{\text{p}}$ , and  $H_{\text{p}} < H$ , where  $H_{\text{on}}$  and  $H_{\text{p}}$  are associated with the characteristic field of the fish-tail effect, the starting field and the peak field, respectively. This indicates that the fish-tail effect is related to the crossover of vortex states, and the different

Table 3.1: Parameters used to model the temperature dependence of  $J_c(T)$  and  $S(T) = d \ln M / d \ln(t)$ . (Source of table: [1])

Crystal (no.)	Ion fluence $10^{16}$ ions/cm <sup>2</sup>	$J_{c0}$ (MA/cm <sup>2</sup> )	$U_{00}$ (K)	$\mu$	$\ln(t/t_{\text{eff}})$
1	0	3.6	140	1.0	33
1	1	23	160	1.6	42
2	0	2.5	160	1.06	33
2	0.3	7.0	160	1.5	33
2	0.6	11	160	1.4	33

dynamics is dominated within each regime. This is firstly pointed out by Prozorov *et al.* in IBSs [69]. Above  $H_p$ , the vortex dynamics is dominated by the plastic creep, as discussed by Abulafia *et al.* in YBCO [74]. Here the plastic creep is though to be the different category of vortex dynamics from elastic motion of vortex ensemble, i.e., the dislocation of flux-line lattice, mediating plastic creep, which leads to fast escape of vortices from the superconductor. The vortex pinning energy for plastic motion  $U_{\text{pl}}$  is estimated as

$$U_{\text{pl}} \simeq \varepsilon \varepsilon_0 a \propto B^{-1/2}. \quad (3.76)$$

The negative  $\mu$ , or often notated as  $p \equiv -\mu$  with a value of  $\simeq 0.5$  is interpreted as the realization of the plastic creep. As a simple way instead, the large  $S$  observed in IBSs is attributed to the plastic creep. The example of the vortex phase diagram extracted from the creep measurement in optimally-doped  $\text{Ba}(\text{Fe}_{0.92}\text{Co}_{0.08})_2\text{As}_2$  is shown in Fig. 3.14. The liquid phase, located at high temperatures and high fields in Fig. 3.14, is the region where the critical current density  $J_c$  is zero, where the vortices can freely move.

### 3.9 Pinning by columnar defects and Bose-glass theory

The weak-collective pinning and collective-creep theory are applicable to weak pointlike pins (uncorrelated disorder). However, the optimized vortex-pinning center should have a correlated structure along the field direction, since the vortex has one-dimensional structure. Such correlated disorders are categorized to planar defects and line defects. An example of planar defects is the twin boundaries. The twin boundaries are inevitable in YBCO unless the sample is "de-twinned" by applying in-plane uniaxial pressure. Actually the pinning from the twin-boundaries

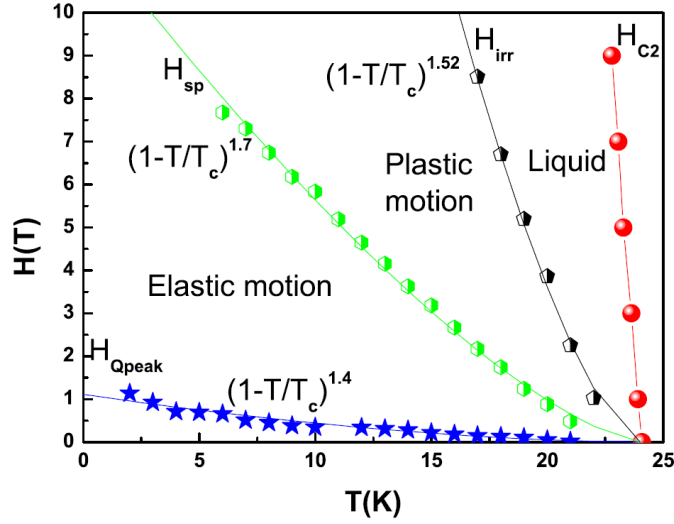


Figure 3.14: The vortex phase diagram in  $\text{Ba}(\text{Fe}_{0.92}\text{Co}_{0.08})_2\text{As}_2$  determined by the vortex creep measurement. (Source of figure: [24])

are often observed in untwinned YBCO. In highly anisotropic layered compounds, the blocking layers work as planar pinning (intrinsic pinning) when the in-plane field is applied. On the other hand, the screw dislocation is an example of the intrinsic uniaxial defects. However the amount of dislocation is uncontrollable. The most remarkable type of pinning is the pinning by the columnar defects (CDs). In the cuprate film, the naturally assembled columnar pins grown along the  $c$  axis can be utilized. The more prominent way to introduce CDs is to carry out by the energetic heavy-ion irradiation. The collision of the swift-heavy ion with the electronic and nuclear system of the target material makes the tracks of damage with a typical diameter of 5 nm. Note that the vortex-core diameter  $\sim \xi$  is just the right size of CD diameter in cuprates. When the energy of the heavy ions are high enough, the tracks are aligned parallel to each other, which is the ideal columnar pin configuration. With lowering irradiation-particle energy, the angular spread of the tracks is observed due to multiple scattering. In cuprates, this heavy-ion irradiation demonstrates a profound effect of CDs on the vortex system. First, due to its strong pinning energy, the critical current density  $J_c$  in heavy-ion irradiated cuprates is greatly enhanced, not only compared with  $J_c$  in pristine sample but that in proton-irradiated one. To show that this enhancement is due to the vortex confinement within the CDs, a YBCO single crystal irradiated at  $30^\circ$  off the  $c$  axis is measured under the applied field aligned to CDs and far away from CD direction ( $\pm 30^\circ$  with respect to  $c$  axis). This configuration extracts the unidirectional pinning effect apart from the isotropic point pinning effect or the geometrically



derived effect, such as demagnetization effect, so that we can know whether the enhancement is attributable to CDs or another ones, such as point pins introduced by the “side effect” of the irradiation. The magnetization loops address the significant enlargement at  $\mathbf{H}||\text{CDs}$ , which testifies the effectiveness of CDs in cuprates.

The amount of defects are conventionally counted by the matching field  $B_\phi = \phi_0/d^2 = \phi_0 n_{\text{pin}}$ , where  $d$  is the mean separation between the nearest CDs and  $n_{\text{pin}}$  is the areal density of columnar pinings. Here the CDs are assumed to pass completely through the sample. With this expression, we can know the relation between the number of vortices and that of CDs. Namely, when  $B = B_\phi$ , all the defects would be occupied by the vortices if CDs are periodically arranged.

The vortex pinning and dynamics have a peculiar properties, which is completely different from the vortex glass state. Since the physics of the vortex system under the CD pinning potential is mapped on the two-dimensional Boson, this phase is called the Bose glass phase. As far as  $\mathbf{H}$  is aligned to CDs, the Bose glass phase is realized in a wide range of the  $B - T$  phase diagram, apart from the liquid phase in the vicinity of the superconducting transition line. These two phases are separated by the Bose glass transition line  $T_{\text{BG}}(H)$ . Within the Bose glass phase, another characteristic field can be defined, so-called the accommodation field  $B^*(T)$ , which is the same with the matching field at low temperatures. Below  $B^*$ , all the vortices are trapped by CDs, while above  $B^*$  some of the vortices escape from CDs. In the former case, only the vortex-defect interaction is considered, while the interaction among vortices becomes relevant and the effect of the collective creep should be considered in the latter case. This  $B^*(T)$  line goes to zero at some characteristic temperature, called the depinning temperature  $T_{\text{dp}}$ , above which the effectiveness of the pinning from CDs is entropically smeared out. In this theory,  $J_c$  at low temperature is possible to become close to the depairing current density  $J_0 = c\phi_0/12\sqrt{3}\pi^2\lambda_{ab}^2\xi_{ab}$ , at which the superconducting pairing is broken.

Experimentally, we can clearly observe characteristic behaviors at  $B^*$ , attributable to the Bose-glass state. Figures 3.15 and 3.16 are the temperature dependence of the screening current density  $J$  and the normalized relaxation rate  $S$  at several fields parallel to CDs. The temperature of the peak in  $d \ln J/dT$  (in other words, the drop in  $J(T)$ ) and the peak in  $S(T)$  coincide. These points at several fields in  $B - T$  plane is shown in Fig. 3.17, indicating  $B^*$ .  $B^*(T)$  drops to zero at the so-called depinning temperature  $T_{\text{dp}}$  of  $\simeq 41$  K. This temperature is dose independent as shown in the inset of Fig. 3.17. Such an acceleration of  $S$  and the drop in  $J$  as a result

of a large  $S$  are explained by the variable range hopping of vortices among CDs. Namely, the vortex hopping is in most cases to the nearest CDs, but in this region the vortices can hop to the position far from CDs, resulting in fast relaxation rate.

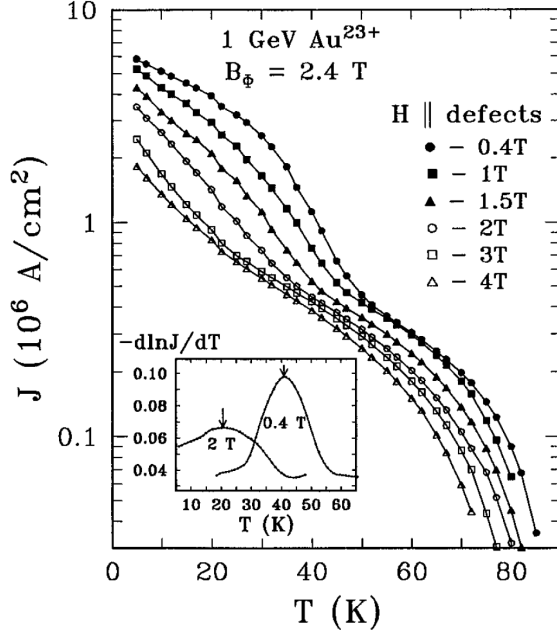


Figure 3.15: The temperature dependence of the screening current density  $J$  under several magnetic fields in 1-GeV Au-irradiated  $\text{YBa}_2\text{Cu}_3\text{O}_{7-\delta}$  with a matching field  $B_\phi = 2.4$  T. Inset: the derivation  $d \ln J / dT$  as a function of temperature. The arrows are correspondent to the drop in  $J(T)$ . (Source of figure: [25])

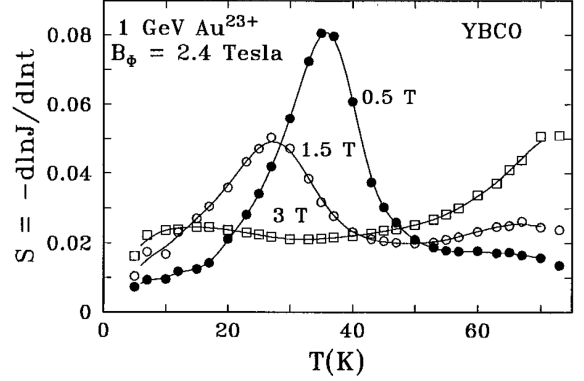


Figure 3.16: The temperature dependence of the normalized relaxation rate  $S$  under several magnetic fields in 1-GeV Au-irradiated  $\text{YBa}_2\text{Cu}_3\text{O}_{7-\delta}$  with a matching field  $B_\phi = 2.4$  T. The peak temperature in  $S(T)$  coincides with the temperature of the drop in  $J(T)$ . (Source of figure: [25])

Another interesting feature is observed in the response to tilting of magnetic field. When  $\mathbf{H}$  is parallel to the CDs, below the Bose glass transition temperature  $T_{\text{BG}}(\mathbf{H})$  vortices condense into a Bose glass phase. A fascinating feature of this phase is its stability to the tilting of magnetic field, which is the consequence of the infinite tilt modulus  $c_{44}$  [75, 76, 21]. When  $\mathbf{H}$  is tilted away from the direction of the CDs by an angle smaller than the so-called lock-in angle ( $\theta_L$ ), the vortices remain trapped by the CDs in their whole length. This stiffness of the vortex configuration manifests as an almost orientation-independent  $J_c$  over the angular extension of the lock-in phenomenon, which has often been observed in cuprates in magnetization [77, 78, 79, 80, 81] and transport measurements [82, 83, 84]. Figure 3.18 shows the fingerprint of lock-in state in 309-MeV Au-irradiated  $\text{YBa}_2\text{Cu}_3\text{O}_{7-\delta}$  with a matching field  $B_\phi = 1$  T. The CDs are introduced

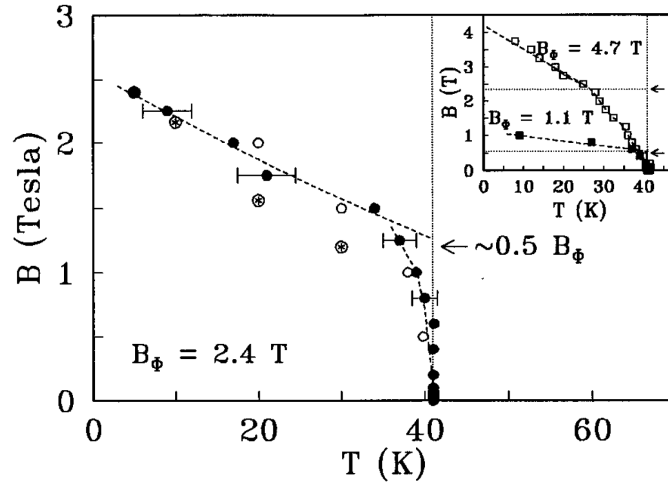


Figure 3.17: The vortex phase diagram in 1-GeV Au-irradiated  $\text{YBa}_2\text{Cu}_3\text{O}_{7-\delta}$  with a matching field  $B_\phi = 2.4$  T. Inset: the similar plot in different matching fields of  $B_\phi = 1.1$  T and 4.7 T. (Source of figure: [25])

with an angle of  $30^\circ$  from  $c$ -axis. We clearly see the plateau structure around  $\mathbf{H}||\text{CDs}$ , which is attributable to lock-in state. In fact, as shown in Fig. 3.19, the width of these plateau ( $2\varphi_L$ ) are proportional to  $1/H$ , which is consistent with the prediction of the Bose-glass theory.

### 3.10 Summary and the motivation of our study

Vortex pinning and dynamics are the result of complexity of vortex-defect and vortex-defect interactions. If point-like defects are included in a superconductor, the vortex system in high-temperature superconductors is expected to show the vortex-glass phase. A number of randomly distributed weak-pinning sites are the origin of the critical current density and the finite relaxation rate. Conversely, what vortex states are realized at each temperature and field region is investigated by those physical quantities. Although the general trend of vortex behaviors in cuprates are thought to be understandable, the fundamental features and their mechanism in the second class of high-temperature superconductor, IBSs, are still not clarified. As a first step, we should examine whether the vortex behaviors can be understood by the vortex-glass theory, similar to the case of cuprates. As a result, we can clarify the universality of vortex system in high-temperature superconductors.

In the case of heavy-ion irradiated system, the vortex system in cuprates is drastically different from that in the as-grown sample, which is explained by the Bose-glass phase. However,

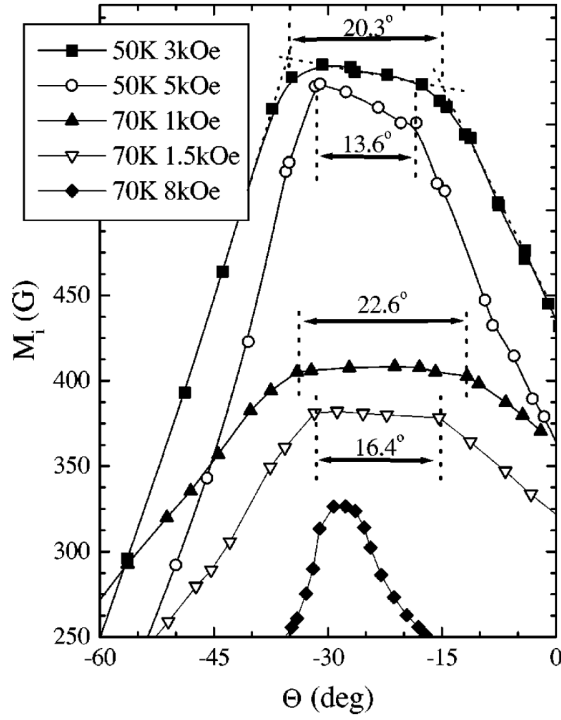


Figure 3.18: Angular dependence of the magnetization in 309-MeV Au-irradiated  $\text{YBa}_2\text{Cu}_3\text{O}_{7-\delta}$  with a matching field  $B_\phi = 1$  T. The CDs are introduced with an angle of  $30^\circ$  from  $c$ -axis. The plateau feature is observed around field parallel to CDs. (Source of figure: [26])

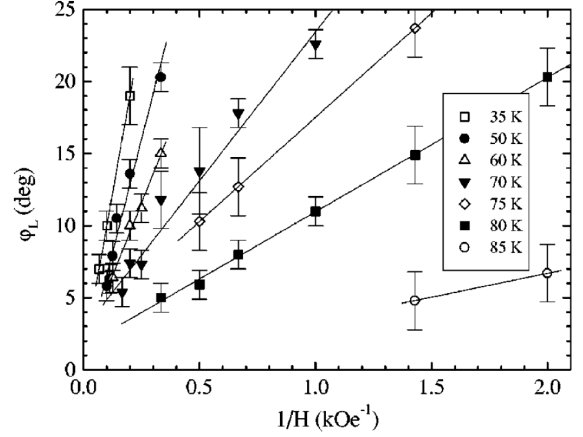


Figure 3.19: The plateau width  $2\varphi_L$  as a function of  $1/H$  in 309-MeV Au-irradiated  $\text{YBa}_2\text{Cu}_3\text{O}_{7-\delta}$  with a matching field  $B_\phi = 1$  T. The CDs are introduced with an angle of  $30^\circ$  from  $c$ -axis. The solid lines are the linear fit to each data of the fixed temperature. (Source of figure: [26])

some quantitative inconsistency between the experiment and theory is not solved. Since IBSs are known to be successfully introduced columnar defects by heavy-ion irradiation, IBSs propose a new stage to examine the validity of Bose-glass theory, if the realization of the Bose-glass phase in IBSs is testified. Therefore, the first step we should do is to show whether this Bose-glass state is realized also in IBSs.

In general, studies on the vortex physics is strongly related to future applications of superconducting wires, through the realization of high-performance of the transport current with a small dissipation. With this study, we can know the optimal condition for the highest  $J_c$  and the stability (keep high screening current density) over time.

## Chapter 4

# Experimental Details

### 4.1 Single crystal growth

The systems we focused on in this study are Co- and K-doped  $\text{BaFe}_2\text{As}_2$ . The high-quality single crystals of both doping were grown by self-flux method. The precursors of FeAs and CoAs powder are synthesized by solid-state reaction. The stoichiometric amounts of Fe/Co powder and As pieces were loaded into a quartz tube with a diameter of 10 mm $\phi$ , followed by evacuation, and sealing, where the weight of As is limited to  $\simeq 2$  g to avoid the explosion of quartz ampule. In dealing As pieces, we always picked them up from freshly opened package in glove box to avoid oxidization. For safety, we sealed it into a second evacuated tube with a diameter of 20 mm $\phi$ . The reaction was carried out at 1065°C for 10 h after heating at 700° for 6 h.

For Co-doped  $\text{BaFe}_2\text{As}_2$ , the crystal growth were carried out by Dr. Yasuyuki Nakajima in Tamegai laboratory. The starting materials were the chunk of Ba, the powder of FeAs, and that of CoAs with a ratio of Ba : FeAs/CoAs = 1 : 5. The oil covering the Ba chunk was washed out by hexane and immersed in that until just before the sealing process. The mixture was placed in an alumina crucible with a diameter of 15 mm $\phi$ , subsequently sealed in a evacuated quartz tube with a diameter of 20 mm $\phi$  as shown in Fig. 4.1. The whole assembly was placed with tilting at an angle of 45° in a box furnace. Empirically, a typical dimension in  $ab$ -plane of crystals becomes large at this angle rather than straight standing. We heated it up to 1150°C, followed by slow cooling down to 800°C at a rate of 5°C/h, as presented in Fig. 4.1(b). The nominal composition of  $x_{\text{nom}}$  defined by CoAs/(FeAs+CoAs) in molar ratio is related with the

actual doping level  $x$  in  $\text{Ba}(\text{Fe}_{1-x}\text{Co}_x)_2\text{As}_2$  by  $x \simeq 0.7 \times x_{\text{nom}}$ . Here the actual composition was determined by EPMA analysis, as described in next section.

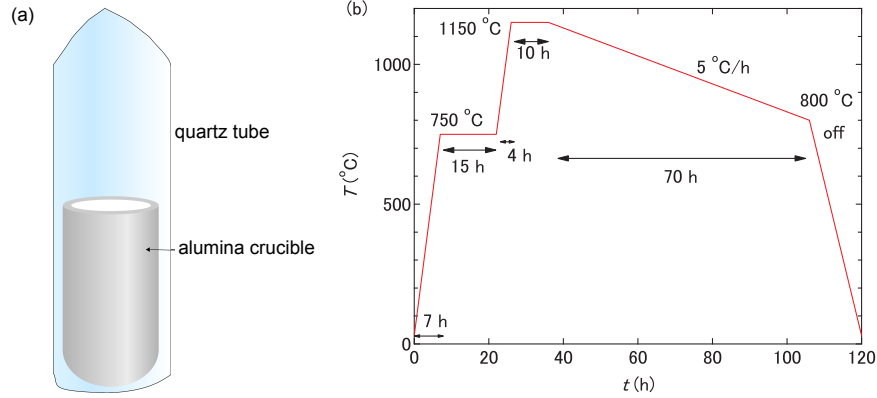


Figure 4.1: (a) The schematic view of the assembly for Co-doped  $\text{BaFe}_2\text{As}_2$  single crystal growth. (b) The heating procedure in  $\text{Ba}(\text{Fe}_{1-x}\text{Co}_x)_2\text{As}_2$  single-crystal growth.

For K-doped  $\text{BaFe}_2\text{As}_2$ , we used different flux for the different doping levels. Previously, the single crystals were grown by FeAs with quartz tube, as in the case of Co-doped  $\text{BaFe}_2\text{As}_2$ . It is known that the quartz tube is reacted and easily broken by K-vapor, so that we employed the stainless steel ampule as illustrated in Fig. 4.2(a). Here we utilize the swage lock to seal the ends of tube, as suggested in Ref. [85]. It should be noted that another advantage addressed in Ref. [85] is the use of KAs flux method. It is confirmed in transport measurements [85, 86, 87] (and in the sample by effectively similar synthesis [88]) that the quality of single crystals of  $\text{KFe}_2\text{As}_2$  by way of KAs self-flux is higher than that with K flux. For  $0.5 < x < 1.0$  in  $\text{Ba}_{1-x}\text{K}_x\text{Fe}_2\text{As}_2$ , the situation is more drastic, since only polycrystals had been able to grow in this doping levels [89]. The KAs-flux has solved this problem. Even at the doping levels of  $0 \leq x \leq 0.5$ , KAs flux is of advantage to obtain high-quality crystals [7]. However KAs is so reactive that it is difficult to deal with, so we have adopted KAs flux only for overdoped sample and conventional FeAs flux method was employed for underdoped and optimally doped samples. We have grown three different doping levels of  $x = 0.23$  (underdoped),  $0.42$  (optimally doped), and  $0.69$  (overdoped). (Here  $x$  is actual doping level, see next section.) For underdoped and optimally doped samples, the Ba and K chunks with FeAs powder were put into alumina crucible with a molar ratio of  $\text{Ba}/\text{K}:\text{FeAs}=1:4$ . The total amounts were  $\simeq 5$  g. The ampule sealed under  $\text{N}_2$  atmosphere was

placed in a box furnace with an angle of  $45^\circ$ , and heated up to  $1100^\circ\text{C}$ , similar to the case of Co-doping. The detail of heating procedure was shown in Fig. 4.2(b). Firing at  $1200^\circ\text{C}$  or higher makes stainless steel fragile. When high temperature synthesis is necessary, the oxidization of stainless steel should be avoided. This is, for example, realized by tube furnace with flowing  $\text{N}_2$  gas. The obtained crystals have mirror surfaces and can be cleaved to obtain *ab*-plane. The typical dimension in *ab*-plane is 5 mm as shown in Fig. 4.3 For overdoped sample, the precursor of FeAs and BaAs powder are necessary. The BaAs reaction was started from Ba chunks and As pieces. We cut Ba chunks into small pieces, typically 1 mm cubic, to enlarge the surface area for the reaction. Even if we do so, we have to care the amount of As, since the reactivity of As with Ba *pieces* is much weaker than that with Fe *powder*. Therefore the weight of As was limited to  $\simeq 0.7$  g not to be cracked by As vapor in heating. The stoichiometric amounts of Ba and As were sealed in evacuated 10 mm $\phi$  quartz tube with a length of 150 mm. After the reaction, BaAs was ground into powder in a glove box and kept away from air exposure. The starting materials for the crystal growth are K chunks, As pieces, BaAs powder, and FeAs powder. The idea is to grow crystals in BaAs/KAs flux, but we avoid to directly make KAs powder for safety, so that the effective KAs flux method was exploited. The specific molar ratio was BaAs : K : As : FeAs = 0.4 : 12 : 11 : 2. Namely, the nominal composition corresponds to  $\text{Ba}_{0.4}\text{K}_{0.6}\text{Fe}_2\text{As}_2$  and the remaining KAs flux. The processes other than heating procedure were the same as that in underdoped and optimally doped samples. As shown in Fig. 4.4, we heated up to  $900^\circ\text{C}$  for 10 h after held at low temperature for several hours, which was followed by slow cooling at a rate of  $4^\circ\text{C}/\text{h}$  down to  $650^\circ\text{C}$ .

We cut the samples into rectangular thin plates for dc-transverse resistivity and magnetization measurements before or after irradiations.

## 4.2 Electron probe micro probe analyses

The actual doping level in a single crystal was determined by electron probe micro probe analyzer. The crystal was attached on carbon tape, which was put onto scanning electron microscopy (SEM) sample holder. The energy-dispersive x-ray spectroscopy (EDX) was equipped to this SEM instrument, and the ratio of each element on the surface of the crystals was identified. The optimal Co-doping level covered in this thesis was  $x = 0.07$  with  $T_c = 23.5 - 24.0$  K. On the

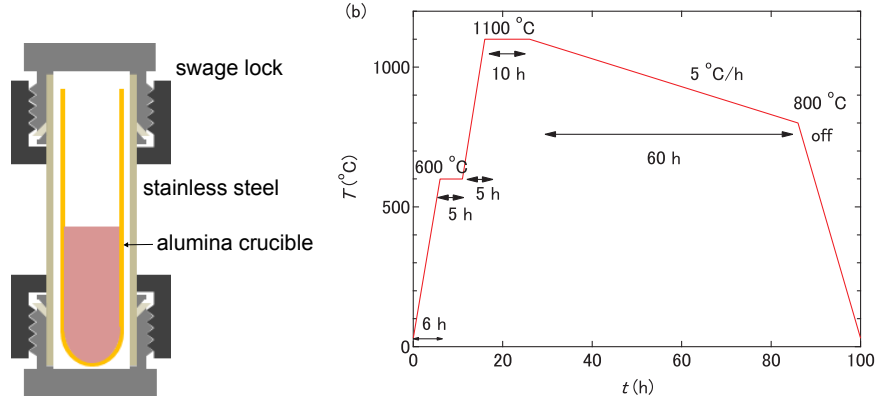


Figure 4.2: (a) The schematic view of the assembly for K-doped  $\text{BaFe}_2\text{As}_2$  single crystal growth. (b) The heating procedure in  $\text{Ba}_{1-x}\text{K}_x\text{Fe}_2\text{As}_2$  single-crystal growth for  $x = 0.23$  and  $0.42$ .

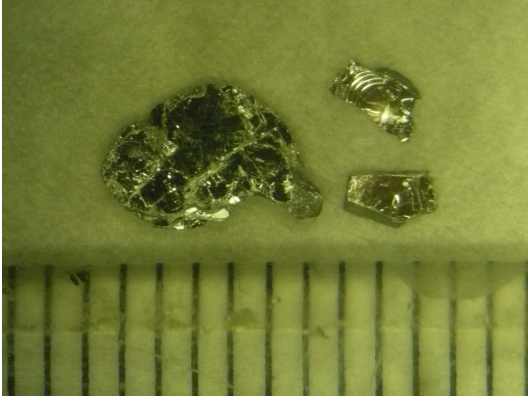


Figure 4.3: The obtained single crystals of  $\text{Ba}_{0.58}\text{K}_{0.42}\text{Fe}_2\text{As}_2$ . The scale is mm. The mirror surface is  $ab$ -plane.

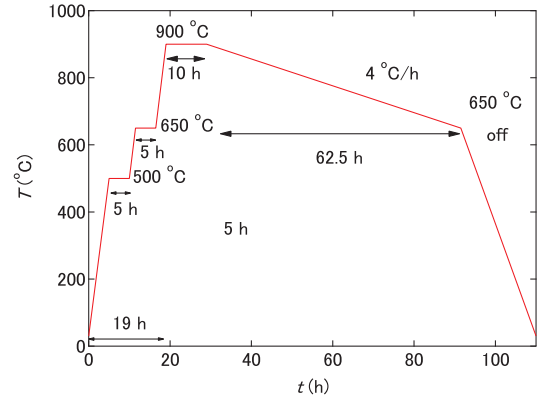


Figure 4.4: The heating procedure in  $\text{Ba}_{0.31}\text{K}_{0.69}\text{Fe}_2\text{As}_2$  single crystal growth.

other hand, the actual K-doping levels were  $x = 0.23$ ,  $0.42$ , and  $0.69$  for underdoped, optimally doped, and overdoped samples, respectively.

### 4.3 Heavy-ion irradiation

In this thesis, two species of heavy-ion are adopted to create correlated defects at some selective energies. One of them is gold (Au) ions, whose energy is 200 MeV or 2 GeV. The 200 MeV Au-irradiation was carried out using tandem accelerator in Japan atomic energy agency (JAEA). Another energy of 2 GeV Au-irradiation was done at INFN-LNS (Laboratori Nazionali del Sud), Catania, Italy. The other species of uranium (U) was irradiated at RIKEN, the energy



of which was fixed to 2.6 GeV. All the samples to be irradiated are thinned to fully penetrate the swift-heavy ions. The upper limit of the thickness, which is called the projected range, is calculated by the stopping and range of ions in matter (SRIM) code [90]. The values are 13.6  $\mu\text{m}$ , 62.8  $\mu\text{m}$ , and 60.8  $\mu\text{m}$  in the irradiation for  $\text{Ba}(\text{Fe}_{0.93}\text{Co}_{0.07})_2\text{As}_2$  irradiated by 200 MeV Au-ions, 2 GeV Au-ions, and 2.6 GeV U-ions, respectively. In  $\text{Bi}_2\text{Sr}_2\text{CaCu}_2\text{O}_{8+\delta}$ , it is reported that defect morphology along the track gradually changes [91]. In order to obtain the ideally parallel columnar defects (CDs), we cleaved the sample to be approximately half of the projected range. The fabricated samples were put on a aluminum sample holder. We prepared different sample holders for different irradiation conditions. The areal density of defects are counted by the matching fields  $B_\phi$ , at which the density of vortices and CDs is the same. The detail of the matching field is elaborated in the previous chapter. The typical  $B_\phi$  is a several tens of kOe.

#### 4.4 Proton irradiation and *in-situ* resistivity measurement

The 3-MeV proton ( $\text{H}^+$ ) was irradiated along the  $c$ -axis at  $T = 50$  K at National Institute of Radiological Sciences - Heavy Ion Medical Accelerator in Chiba (NIRS-HIMAC). Since random point defects including Frenkel pairs, some of which are mobile even at room  $T$  (Ref. [92]), were expected to be produced by 3-MeV  $\text{H}^+$  irradiation, [93] we kept the temperature low ( $\leq 50$  K) to stabilize defects during the following resistance measurements. The proton flux was limited to  $\lesssim 10^{12}$  ions/ $\text{cm}^2/\text{s}$  to avoid excessive heating of the crystals. The samples to be irradiated were cleaved to be thinner than a half of the projected range  $\sim 50$   $\mu\text{m}$ , similar to the heavy-ion irradiation. For *in-situ* resistivity measurements, gold wires were attached to the samples by silver paste with a standard four-probe configuration to measure the longitudinal resistivity  $\rho$ .

The home-built measurement system was based on the closed-cycle refrigerator. The sample holder is illustrated in Fig. 4.5. The wired samples were loaded onto the sapphire plate. The samples for vortex study were placed on the aluminum foil stucked on the side of sapphire plate. This foil was electrically contacted to the copper sample holder not to be charged up.

#### 4.5 Magnetization measurement

The dc magnetization up to 50 kOe was measured in a commercial superconducting quantum interference device (SQUID) magnetometer (MPMS-XL5, Quantum Design). Most of the mea-

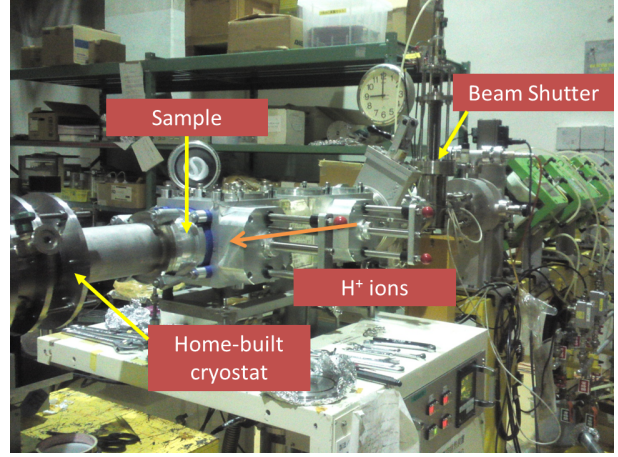
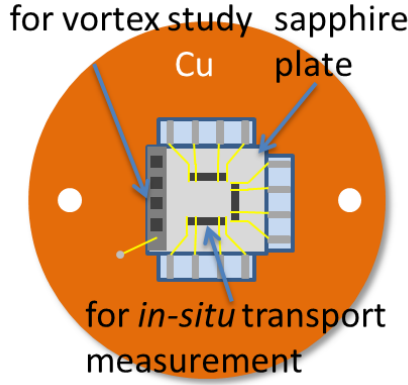


Figure 4.5: The schematic view of the sample holder the overall system for proton irradiation.

measurements were performed for longitudinal magnetization under magnetic field ( $H$ ) parallel to  $c$ -axis. Some of the samples were small, so the background signal from the sample holder ( $M_{BG}$ ) was not negligible. Therefore we designed the sample holder by quartz tube, which has a small cuboid-like hole as the sample space. The  $H$  dependence of  $M_{BG}$  is linear, which enables us to subtract the contribution from the sample holder without ambiguity.

The temperature dependence of Meissner signal was measured under low field parallel to  $c$ -axis, typically  $H = 5$  Oe. The magnetization loops were measured at fixed temperature with field sweeping  $H = 0 \rightarrow 50 \rightarrow -50 \rightarrow 0$  kOe. For the creep measurement, in evaluating of the normalized relaxation rate  $S$ , the time-evolution of the magnetization  $M(t)$  were traced typically for an hour.

To elucidate angular dependence of magnetization, the transverse magnetization  $M_t$  (perpendicular to  $\mathbf{H}$ ) was measured as well as the longitudinal component  $M_l$  (parallel to  $\mathbf{H}$ ), collaborated with the group of Dr. Leonardo Civale in Los Alamos National Laboratory (LANL). We used a SQUID magnetometer equipped with two sets of pick-up coils to measure both components, and change  $\mathbf{H}$  direction using a rotator with its rotational axis perpendicular to  $\mathbf{H}$ . Thus, we could control the polar angle ( $\theta$ ) between  $\mathbf{H}$  and the sample normal  $\hat{n}$ . One of the sides of the square crystal was aligned parallel to the rotation axis. To prevent any damage in the crystal from magnetic-field-induced torque, we loaded the sample after sandwiching it by a couple of sapphire plates with Apiezon grease. After cooling down the sample below  $T_c$  at

$\theta = 45^\circ$ , we aligned the rotator probe to maximize  $M_t$  by azimuthal rotation in order to make the sample plate face the transverse pickup coils.

## Chapter 5

# Pair-breaking effects in

## $\text{Ba}_{1-x}\text{K}_x\text{Fe}_2\text{As}_2$

### 5.1 Introduction

The superconducting gap structure and the underlying pairing mechanism of iron-based superconductors (IBSs) are under intense debate. Nevertheless, no consensus has been established. At a very early stage, it was claimed that the superconductivity in IBSs was mediated by anti-ferromagnetic (AFM) spin fluctuations, leading to the so-called  $s_{\pm}$ -wave gap structure [32, 31]. Namely, the opposite sign of the order parameter between hole and electron Fermi surfaces (FSs) is realized via interband scatterings between hole and electron FSs. However, another perspective has been proposed that the orbital degrees of freedom play an important role in various physical properties. The superconductivity mediated by orbital fluctuations has a gap function of  $s_{++}$ -wave without sign reversal [15, 33]. Some experimental results such as ultrasonic measurement support the importance of the orbital degrees of freedom [94, 95]. In optimally K-doped  $\text{BaFe}_2\text{As}_2$ , laser angle-resolved photoemission spectroscopy (ARPES) measurement provides results of the same magnitude of the superconducting gap on different hole FSs, which is difficult to explain by only the spin-fluctuation scenario [11], as we described in Sec. 2.4.1. Moreover, a FS-selective gap structure including octet line nodes in the end member of the series  $\text{KFe}_2\text{As}_2$  implies that several pairing mechanisms are competing, namely, spin fluctuations and orbital fluctuations [42].

To go forward with the identification of the pairing mechanism of IBSs, a phase sensitive

probe is required. The impurity effects have played a key role for this purpose since the study of cuprate superconductors [96]. According to Anderson's theorem, nonmagnetic impurities do not work as pair breaker in isotropic single-gap superconductors. By contrast, fast suppression of the superconducting transition temperature  $T_c$  is expected in superconductors with a sign change such as  $d$  wave, analogous to magnetic impurities in  $s$ -wave superconductors. The details are elaborated in Sec. 2.4.4. In fact, this has been observed in cuprate superconductors, such as Zn-doped  $\text{YBa}_2\text{Cu}_3\text{O}_{7-\delta}$  and  $\text{Bi}_2\text{Sr}_2\text{CaCu}_2\text{O}_8$  [96]. In IBSs, pioneering studies have been reported [97, 98, 57, 99, 62, 18, 58, 16, 100]. A peculiar way to introduce disorders is energetic particle irradiation. Defects created by 2.5-MeV electron irradiation are reported to behave similarly to Zn substitutions in  $\text{YBa}_2\text{Cu}_3\text{O}_{7-\delta}$  (Ref. [59]). In sharp contrast to chemical substitution, light-particle irradiations enable us to systematically introduce point-like defects in a given sample. The problems in chemical substitution, like structurally unstable and inhomogeneous properties and/or possible changes in carrier density and FS topology, can be also overcome. Such advantages are utilized to single crystalline IBSs to distinguish whether the gap has sign reversal or not. The most striking result obtained is in proton ( $\text{H}^+$ ) irradiated  $\text{Ba}(\text{Fe}_{1-x}\text{Co}_x)_2\text{As}_2$ , which shows a depression of superconductivity slower than that expected for  $s_{\pm}$ -wave superconductors [18].

Among several types of IBSs,  $\text{BaFe}_2\text{As}_2$  is the prototypical system. Especially, optimally and over K-doped  $\text{BaFe}_2\text{As}_2$  have very small residual resistivity (RR), so that the intrinsic impurity scattering is negligible [7]. This is in stark contrast to the Co-doped sample, where direct doping of Fe-site provides a large RR ( $\sim 50 \mu\Omega\text{cm}$  at optimal doping) even after BaAs annealing [34, 7]. Owing to the absence of the intrinsic scattering centers, we can safely attribute RR to extrinsically introduced scattering, which have a possibility of pair breaking.

The objective of this study is to examine the possible sign-reversal in the order parameter between electron- and hole-FSs. The fast suppression by impurity scattering rates means the realization of  $s_{\pm}$ -wave, indicating the pairing mediated by spin fluctuations, whereas the slow suppression denies it.

## 5.2 Results

### 5.2.1 Resistivity in as-grown sample

First, we have measured the resistivity ( $\rho$ ) in a wide range of temperature ( $T$ ) in the as-grown  $\text{Ba}_{1-x}\text{K}_x\text{Fe}_2\text{As}_2$ . Here three doping levels of  $x = 0.23, 0.42, 0.69$  are selected. They corresponds to underdoping, optimally doping, and overdoping, respectively. Figure 5.1 represents the result of  $\rho - T$  measurements in the as-grown samples, which are identical to those used in the irradiation study in the following. The absolute values of  $\rho$  at  $T = 300$  K is slightly reduced with increasing  $x$ . Upon cooling, the crossover from high- $T$  convex to low- $T$  concave behavior is observed at the characteristic  $T^* \simeq 100$  K. These results are quite consistent with the previous reports [101, 7]. In the low- $T$  region  $T \ll T^*$ , a quadratic  $T$  dependence of  $\rho$  is observed in all three samples, which is obvious in the inset of Fig. 5.1. The superconducting transition occurs at  $T_c = 24.4$  K, 37.4 K, and 17.8 K, in  $x = 0.23, 0.42$ , and 0.69, respectively, where  $T_c$  is defined by the midpoint of resistive transition. As shown in Fig. 5.1(b), these values of  $T_c$  almost coincide with the onset of the Meissner signal measured by the superconducting quantum interference device magnetometer, which gives evidence for the bulk transition.

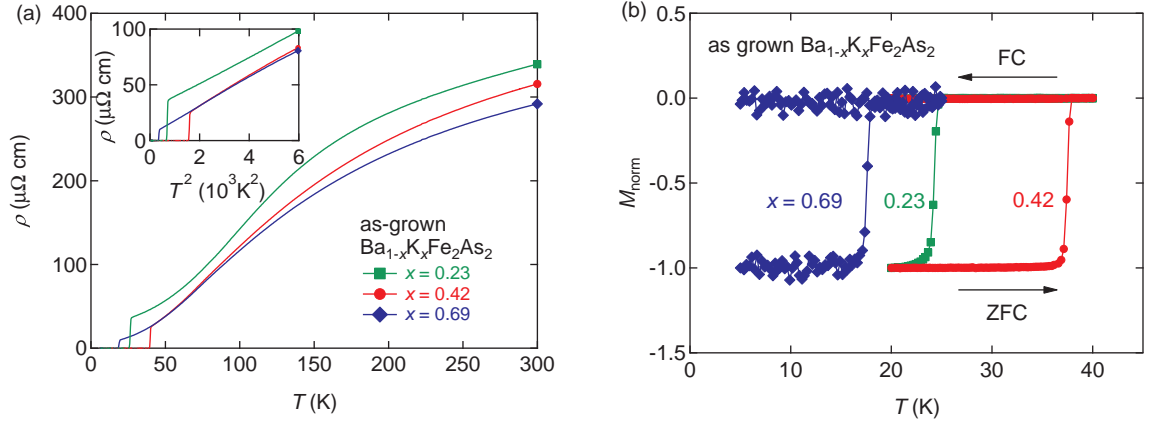


Figure 5.1: (a) Temperature dependence of the resistivity in  $\text{Ba}_{1-x}\text{K}_x\text{Fe}_2\text{As}_2$  ( $x = 0.23, 0.42$ , and  $0.69$ ). Inset: the resistivity as a function of  $T^2$ . (b) Temperature dependence of zero-field-cooled (ZFC) and field-cooled (FC) Meissner signal under  $H = 5$  Oe in  $\text{Ba}_{1-x}\text{K}_x\text{Fe}_2\text{As}_2$  ( $x = 0.23, 0.42$ , and  $0.69$ ).

### 5.2.2 Evolution of resistivity by proton irradiation

The *in situ*  $\rho - T$  measurements right after the 3-MeV  $\text{H}^+$  irradiation are shown in Fig. 5.2. The maximum dose reaches to  $9.2 \times 10^{16}$  ions/cm<sup>2</sup>. Regarding the normal state behavior, all samples show a parallel shift upon irradiation without any low- $T$  upturn, indicating that the point defects introduced by this irradiation are nonmagnetic and no localization effects appear. This fact is quite important in view of the study of pair-breaking effects, since the stiffness of the superconductivity to the nonmagnetic scattering is the key to distinguish the possible sign-reversing order parameter. To estimate the impurity scattering rate, we have extrapolated  $\rho$  in the normal state to  $T = 0$  K with a function of  $\rho = \rho_0 + AT^2$  and calculated  $\Delta\rho_0 \equiv \rho_0^i - \rho_0^0$ , where  $\rho_0^i$  is  $\rho_0$  of the  $i$ th irradiation. The evolutions of  $\Delta\rho_0$  with the dose are depicted in Fig. 5.3(a). An almost linear increase in  $\Delta\rho_0$  is evident in all samples, although the slope of the underdoped sample is twice as large as the slopes in the optimally doped and overdoped samples. On the other hand, we can see that  $T_c$  is gradually suppressed without significant broadening of the transition in all samples except for the tail part. We will comment on this point in next paragraph. We define  $T_c$  by the midpoint of a sharp  $\rho$  drop, as indicated by Fig. 5.3(c). The resultant  $T_c$  as a function of the dose is shown in Fig. 5.3(b). Here the error bars are twice  $T_c^{\text{onset}} - T_c$  ( $T_c^{\text{onset}}$  is the onset  $T$  of the  $\rho$  drop, see Fig. 5.3(c)), which is smaller than  $\sim 1$  K, except for underdoped sample at higher doses.  $T_c$  suppression,  $\Delta T_c = T_{c0} - T_c$ , is linear with a maximum reduction of 4.3, 3.0, and 4.3 K, for underdoped, optimally doped, and overdoped samples, respectively, where  $T_{c0}$  is  $T_c$  before the irradiation. It should be noted that this suppression of  $T_c$  is much larger than that reported for heavy-ion irradiated (Ba,K)Fe<sub>2</sub>As<sub>2</sub> with a matching field of 21 T ( $\Delta T_c \sim 0.3$  K), where the average spacing of columnar defects is 100 Å (Ref. [102]).

### Tail of the resistive transition

Here we comment on the tail of resistive transition. Namely, by increasing the irradiation dose, a finite value of  $\rho$  remains after the main superconducting transition followed by the second broad transition at a low  $T$ . To clarify the origin, we performed magneto-optical (MO) imaging in a similar crystal of  $\text{H}^+$ -irradiated Ba<sub>0.6</sub>K<sub>0.4</sub>Fe<sub>2</sub>As<sub>2</sub> [Fig. 5.4(b)] after carefully removing silver paste and gold wires. Figure 5.4(a) shows an example of the MO image at  $T = 33$  K under

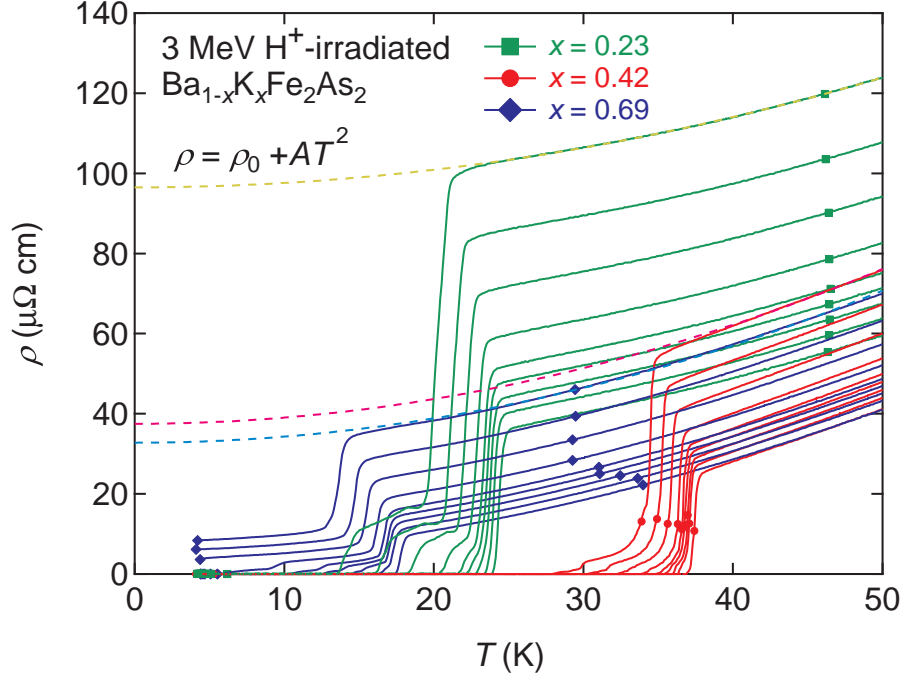


Figure 5.2: Temperature dependence of the resistivity in  $\text{Ba}_{1-x}\text{K}_x\text{Fe}_2\text{As}_2$  ( $x = 0.23, 0.42$ , and  $0.69$ ) with doses of  $0, 0.52, 1.0, 1.6, 2.1, 3.1, 4.8, 6.8$ , and  $9.2 \times 10^{16}$  ions/cm<sup>2</sup>. Broken lines represent fitting lines of  $\rho = \rho_0 + AT^2$ .

$H = 5$  Oe. Under this low-field condition, the superconducting region gives a Meissner response, which shows up as a dark part in the MO image. This is actually observed in most parts of the crystal. Additional dark regions are detected at the very narrow regions just beneath gold wires, surrounded by bright regions, where the superconductivity is weakened or lost. This positional dependent magnetic response addresses lower  $T_c$  beneath the silver paste. One of the possible origins for such a stronger suppression of  $T_c$  is that lower energy  $\text{H}^+$  ions and/or the secondary electrons generated in the silver paste are more effective in introducing point defects. Hence we conclude that the fast suppression of superconductivity under silver paste accompanied by the spatially modulated  $T_c$  is the origin of the tail in resistive transition. A close inspection of the  $\rho - T$  data in Fig. 5.2 allows us to roughly estimate  $(T_{c0} - T_c^{\rho=0})/\Delta T_c \sim 2$  in  $x = 0.23$  and  $0.42$ , while  $\sim 3$  in  $x = 0.69$ . Since  $\Delta T_c$  is proportional to  $\Delta \rho_0$ ,  $\rho_0$  of the part beneath the silver paste is estimated to be twice as large as that of the bare part in  $x = 0.23$  and  $0.42$ , while it is 3 times as large in  $x = 0.69$ . Here the main transition at  $T_c$  is attributed to the property of the bare parts and zero resistivity appears at  $T_c^{\rho=0}$  as a consequence of transition in the region beneath the silver paste. Since the volume beneath the silver paste is much smaller than that of the bare



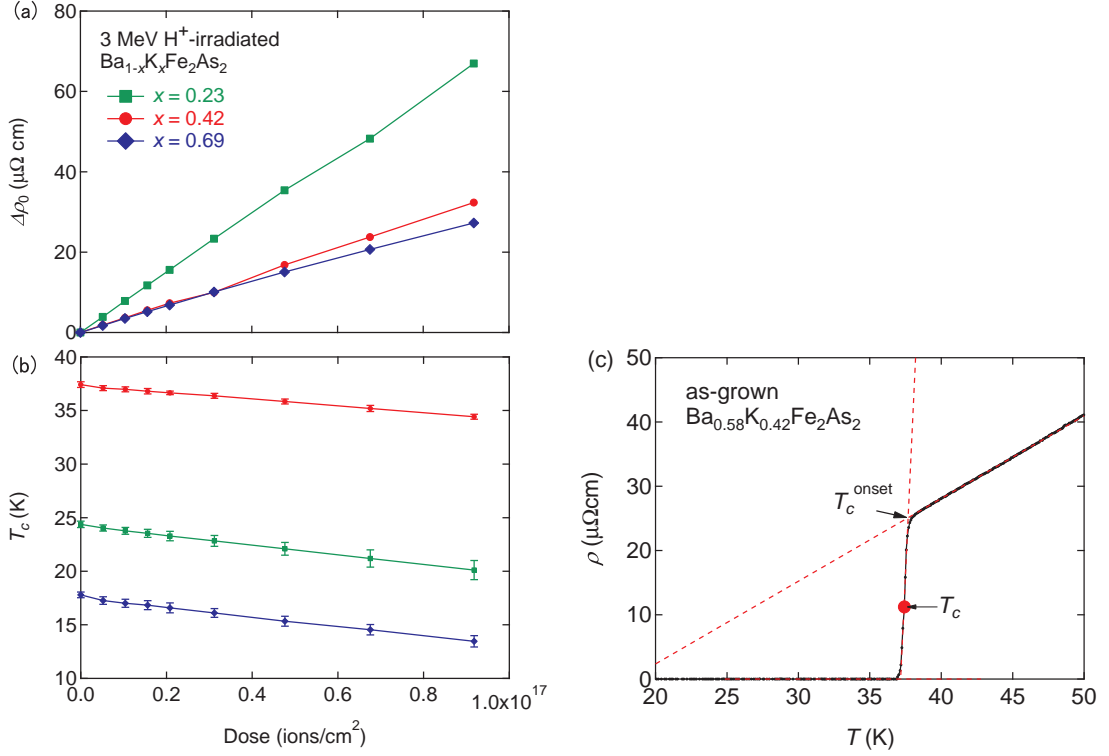


Figure 5.3: Dose dependence of (a)  $\Delta\rho_0 \equiv \rho_0^i - \rho_0^0$  and (b)  $T_c$  in  $\text{Ba}_{1-x}\text{K}_x\text{Fe}_2\text{As}_2$  ( $x = 0.23, 0.42$ , and  $0.69$ ). (c) The definition of  $T_c$  and  $T_c^{\text{onset}}$ . Dashed lines are the linear fit above and in the middle of the resistive transition.

parts, the serial circuit of these parts provides only a small correction to  $\rho_0$ . Such a few percent enhancement of the RR does not affect the pair-breaking discussion above.

### 5.2.3 The relation between $T_c$ and $\Delta\rho_0$

The central issue of the impurity effect is to clarify the relationship between the evolution of  $\rho_0$  and the reduction of  $T_c$ , where  $\rho_0$  is the residual resistivity. Figure 5.5 represents  $T_c$  (main panel) and  $T_c/T_{c0}$  (inset) as a function of  $\Delta\rho_0$ . The suppression rates of  $T_c$ ,  $-\Delta T_c/\Delta\rho_0$ , are 65 K/m $\Omega\text{cm}$ , 95 K/m $\Omega\text{cm}$ , and 161 K/m $\Omega\text{cm}$  for  $x = 0.23, 0.42$ , and  $0.69$ , respectively. It is noteworthy that these values are comparable to the value of 46-77 K/m $\Omega\text{cm}$  in chemically substituted  $\text{Ba}_{0.5}\text{K}_{0.5}\text{Fe}_2\text{As}_2$  (Ref. [16]). The linear extrapolation, drawn by broken lines in Fig. 5.5, gives the critical residual resistivity value  $\Delta\rho_0^{\text{cr}}$  to fully suppress  $T_c$  as 376, 396, and 110  $\mu\Omega\text{cm}$ , respectively. These values of  $\Delta\rho_0^{\text{cr}}$  for the underdoped and optimally doped samples

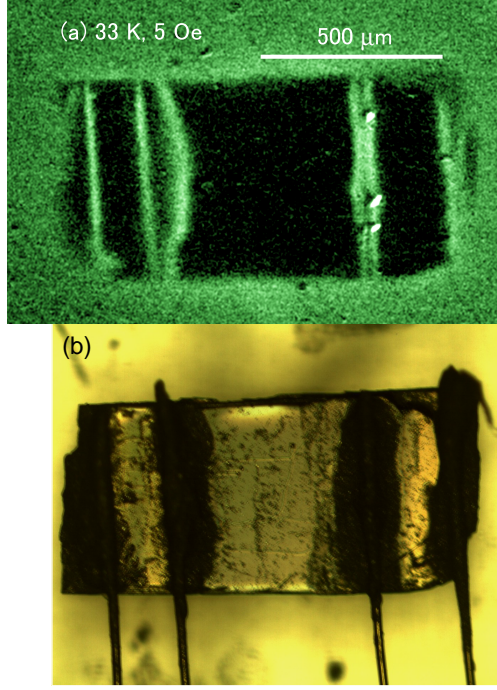


Figure 5.4: (a) A magneto-optical image at 33 K under  $H = 5$  Oe taken after removing silver paste and gold wire from the crystal of  $\text{Ba}_{0.6}\text{K}_{0.4}\text{Fe}_2\text{As}_2$  shown in panel (b).

are similar to previous reports (100-1000  $\mu\Omega\text{cm}$ ) [62, 18, 58, 16]. The overdoped sample, on the other hand, has a smaller  $\Delta\rho_0^{\text{gr}}$ . The fast suppression rate of  $T_c$  in the overdoped sample can be seen even in the  $T_c/T_{c0}$  vs.  $\Delta\rho_0$ , depicted in the inset of Fig. 5.5. The slope in the overdoped sample is 3.5 times larger than the slopes of the underdoped and optimally doped samples.

### 5.3 Discussion

For quantitative discussion of pair-breaking effects by nonmagnetic scatterings, we evaluate the normalized scattering rate  $g = \hbar/2\pi k_B T_{c0} \tau$ , where  $\hbar$ ,  $k_B$ , and  $\tau$  are the Planck's constant divided by  $2\pi$ , the Boltzmann constant, and the scattering time, respectively. If we assume the intraband scattering rate  $\tau_{\text{intra}}^{-1}$  and the interband scattering rate  $\tau_{\text{inter}}^{-1}$  are the same, i.e.  $\tau_{\text{intra}}^{-1} \simeq \tau_{\text{inter}}^{-1} \equiv \tau^{-1}$ , then  $1/\Delta\rho_0 = 1/\Delta\rho_{\text{intra}} + 1/\Delta\rho_{\text{inter}} = (ne^2/m^*)(\tau_{\text{intra}} + \tau_{\text{inter}}) = 2ne^2/m^*\tau^{-1}$ , and we can estimate  $\tau^{-1}$  from  $\Delta\rho_0$  as  $\tau^{-1} = 2ne^2\Delta\rho_0/m^*$ , where  $n$  is the carrier density,  $e$  is the elementary charge, and  $m^*$  is the effective quasiparticle mass. In the following, we show three different estimations of  $g$ ;  $g^{5\text{orb}}$ ,  $g^\lambda$ , and  $g^H$ , which are described in Fig. 5.6(a), 5.6(b), and 5.6(c), respectively.

According to linear response theory based on the five-orbital model, we obtain the relation

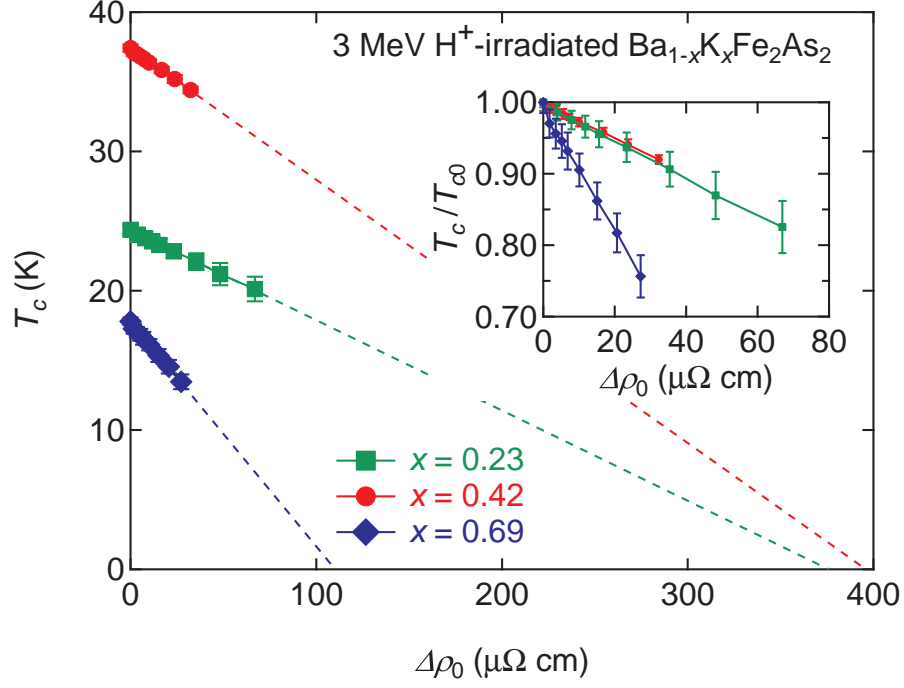


Figure 5.5:  $T_c$  as a function of  $\Delta\rho_0$  in  $\text{Ba}_{1-x}\text{K}_x\text{Fe}_2\text{As}_2$  ( $x = 0.23, 0.42$ , and  $0.69$ ). Inset: The vertical axis is changed to  $T_c/T_{c0}$ .

$\Delta\rho_0$  ( $\mu\Omega$  cm) =  $0.18\tau^{-1}$  (K) in  $\text{Ba}_{1-x}\text{K}_x\text{Fe}_2\text{As}_2$ , leading to the first estimation of  $g^{\text{5orb}} = 0.88z\Delta\rho_0/T_{c0}$ , where  $z$  is the renormalization factor. [103] The angle resolved photoemission spectroscopy measurement in  $\text{Ba}_{0.6}\text{K}_{0.4}\text{Fe}_2\text{As}_2$  gives a result of the renormalization factor  $z = 1/2$  (Refs.[104] and [105]). The obtained  $T_c/T_{c0}$  as a function of  $g^{\text{5orb}}$  is shown in Fig. 5.6(a). The critical values of  $g$  ( $\equiv g_c$ ) where the linear extrapolation of  $T_c/T_{c0}$  goes to zero are evaluated as 6.8, 4.7, and 2.7 in  $x = 0.23, 0.42$ , and  $0.69$ , respectively. These values compare well with those obtained for substitutions of Mn, Co, Ni, Cu, and Zn for Fe in almost optimal-doped crystals of  $\text{Ba}_{0.5}\text{K}_{0.5}\text{Fe}_2\text{As}_2$ ,  $g_c = 4 - 8$  [16].

With London penetration depth  $\lambda = \sqrt{m^*/\mu_0 n e^2}$ , we can obtain another estimation of  $\tau^{-1}$  as  $\tau^{-1} = n e^2 \Delta\rho_0 / m^* = \Delta\rho_0 / \mu_0 \lambda^2$ , where  $\mu_0$  is the vacuum permeability. It is noted that the use of  $\lambda$  allows us to avoid direct estimation of  $n$  and  $m^*$ . Optical measurements in the low-frequency limit give  $\lambda \simeq 2000$  Å in  $\text{Ba}_{0.6}\text{K}_{0.4}\text{Fe}_2\text{As}_2$  (Ref. [106]). Without considering the K doping dependence of  $\lambda$ , we obtain the second estimation  $g^\lambda = \hbar \Delta\rho_0 / \pi k_B T_{c0} \mu_0 \lambda^2$ .  $T_c/T_{c0}$  as a function of  $g^\lambda$  is shown in Fig.5.6(b). The critical values  $g_c$  of the normalized scattering rate obtained from linear extrapolations are 7.5, 5.1, and 3.0 in  $x = 0.23, 0.42$ , and  $0.69$ , respectively.

The conventional approach to estimate carrier density  $n$  is from Hall coefficient  $R_H$  mea-

measurements.  $R_H$  at 300 K is reported to be  $\sim 1 \times 10^{-9} \text{ m}^3/\text{C}$  (Refs. [101, 107], and [108]), which offers the third estimation of  $g^H = \hbar \Delta \rho_0 e / \pi k_B T_{c0} m^* R_H$ . With the mass enhancement factor  $m^* = 2m$  as mentioned above, the critical scattering rate  $g_c$  for  $x = 0.23, 0.42$ , and  $0.69$  is estimated as  $g_c = 33, 23$ , and  $13$ , respectively. Here  $m$  is assumed to be the free electron mass. These values are more than 4 times larger than the other estimations above. This is possibly because  $R_H$  is not a good measure of  $n$  in  $\text{Ba}_{1-x}\text{K}_x\text{Fe}_2\text{As}_2$ , since the  $T$  variation of  $R_H$  is ascribed to several contributions such as multiband nature, antiferromagnetic spin fluctuations, Fermi surface reconstruction, and so on. Unfortunately, it is difficult to separate these contributions from others. For example, Ohgushi and Kiuchi analyzed  $R_H$  in  $\text{Ba}_{1-x}\text{K}_x\text{Fe}_2\text{As}_2$  assuming two-band model with an expression of hole carrier density  $n_h = n_0 + \frac{x}{2} \frac{m_h}{m_h + m_e}$  and electron carrier density  $n_e = n_0 - \frac{x}{2} \frac{m_e}{m_h + m_e}$  and found a strong  $T$  dependence of  $n_0$  and  $m_h/m_e$  (Ref. [101]). This means that the estimation of  $g^H$  largely depends on the choice of  $T$  in  $R_H$ . In addition, we cannot use  $R_H$  at low  $T$  since an apparent spin fluctuation effect is identified as evidenced by a strong  $T$  dependence of  $R_H$ , especially in underdoped samples. Thus  $g^H$  must overestimate the scattering rate.

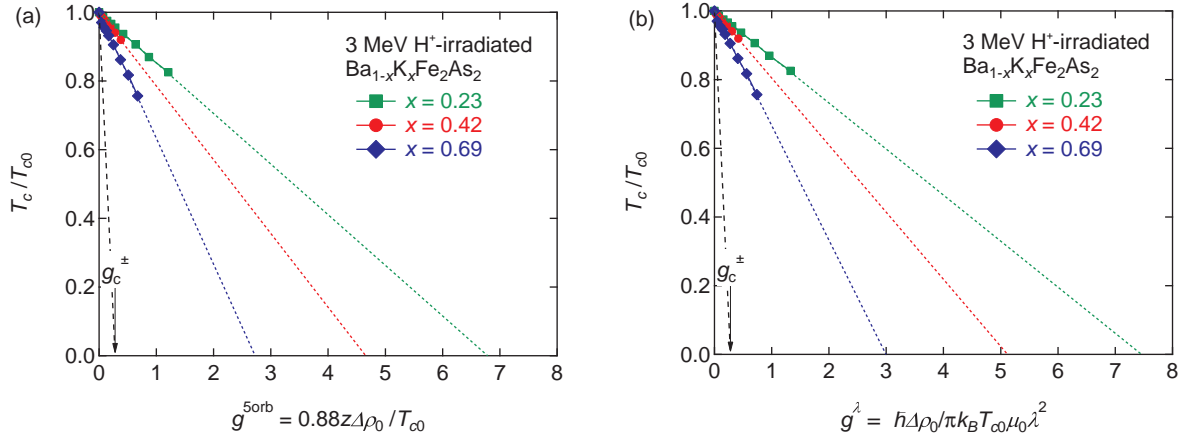


Figure 5.6:  $T_c/T_{c0}$  as a function of a normalized scattering rate  $g = \hbar/2\pi k_B T_{c0}\tau$  in  $\text{Ba}_{1-x}\text{K}_x\text{Fe}_2\text{As}_2$  ( $x = 0.23, 0.42$ , and  $0.69$ ) evaluated by (a) the five-orbital model  $g^{5orb} = 0.88z\Delta\rho_0/T_{c0}$  and (b) the London penetration depth  $g^\lambda = \hbar\Delta\rho_0/\pi k_B T_{c0}\mu_0\lambda^2$ . These data are linearly extrapolated to obtain critical values of  $g$  as shown by dotted lines. Dashed lines indicate the critical scattering rate  $g_c^\pm \simeq 0.3$  by simple estimation for  $s_\pm$ -wave scenario.

These three results should be compared with the  $s_\pm$ -wave scenario with equal gap magnitudes

of opposite signs on different FSs. Provided the simplest assumption of  $\tau_{\text{intra}}^{-1} = \tau_{\text{inter}}^{-1}$ , the pair breaking is evaluated by the Abrikosov-Gor'kov formula,  $-\ln T_c/T_{c0} = \psi(1/2 + gT_{c0}/2T_c) - \psi(1/2)$ , where  $\psi(x)$  is a digamma function and  $g = \hbar\tau_{\text{inter}}^{-1}/2\pi k_B T_{c0}$ . The obtained critical  $g$  in this scenario is  $g_c^{\pm} \simeq 0.3$ , as shown in Figs. 5.6(a)- 5.6(c). Obviously, all estimates of  $g_c$  are much larger than  $g_c^{\pm} \simeq 0.3$ . By contrast, it is expected that the rate of  $T_c$  suppression is much smaller in the  $s_{++}$ -wave scenario. Therefore, our results strongly suggest that the realization of the  $s_{\pm}$ -wave gap function in K-doped  $\text{BaFe}_2\text{As}_2$  is unlikely. However, it should be noted that an impurity-robust  $s_{\pm}$  state has recently been discussed by changing the ratio of inter- to intra-band scatterings. [109, 110] To examine if the anomalously small ratio of inter- to intra-band scattering is feasible, Yamakawa *et al.* have recently studied the nonlocal impurity scattering effect [56] in accordance with the first-principle study deriving 3d- and 4d-impurity potentials. [111] They have found that the negligible interband scattering is unrealistic and  $-\Delta T_c/\Delta\rho_0$  is independent of the impurity potential strength and  $T_{c0}$ . They concluded that the  $s_{\pm}$ -wave state is inconsistent with the experimental results reported in IBSs, which is consistent with the local impurity model in Ref.[33]. The results obtained in Refs.[109, 110, 112, 113, 114, 115, 15], and [116] are based on orbital-less multiband model. In this model, the amplitude of interband scattering becomes negligible in a unitary impurity scattering regime. This is why a wide range of ratios of intraband to interband scatterings is examined, and at a small interband scattering rate the superconductivity is robust even in the  $s_{\pm}$ -wave state. However, this model neglects the momentum dependence of the impurity potential originated from the orbital degrees of freedom. When taking it into account, i.e. based on the five-orbital model, it is revealed that a large interband scattering should appear and the  $s_{\pm}$  state is fragile. Hence, we must adopt the comparable interband scattering to the intraband one. Although we cannot specify the ratio of interband to intraband scattering rates, the ratio is not completely an arbitrary assumption. Our present results manifest the robustness of  $T_c$  against the introduction of impurity scatterings, and based on the above consideration, we can safely conclude that they are inconsistent with the  $s_{\pm}$ -wave state in the  $\text{Ba}_{1-x}\text{K}_x\text{Fe}_2\text{As}_2$  system. We should additionally point out that faster suppression of  $T_c/T_{c0}$  in highly overdoped samples is possibly realized if the mass enhancement  $m^*/m$  is large, taking the stronger correlation in the end member of  $\text{KFe}_2\text{As}_2$  into account. [117, 118] The disappearance of the electron FS and the negligible gap size of the outer hole FS are reported for  $x \geq 0.6$ , leading to possible crossover of the superconducting

order parameter, caused by the competition of the pairing mechanism, probably the orbital fluctuations and the spin fluctuations [119, 120]. The observed faster suppression of  $T_c/T_{c0}$  in the  $x = 0.69$  sample might be related to such differences.

Here we stress the advantage of K-doped  $\text{BaFe}_2\text{As}_2$  to discuss impurity effects. As already mentioned above, the as-grown K-doped system has no intrinsic impurity scattering, i.e., negligible RR, so we can discuss all the above by means of  $\rho_0$  instead of  $\Delta\rho_0$ . This enables us to make a straightforward transformation from the RR to the impurity scattering rate. Even if we do so, the obtained results are almost the same because of very small  $\rho_0^0$ . This point gives a significant advantage compared with the Co-doped system, where we can understand the origin of the increment  $\Delta\rho_0$  only but not clearly of  $\rho_0^0$ . Once we are able to obtain high-quality single crystals of K-doped  $\text{BaFe}_2\text{As}_2$ , the study in this sample is more suitable than that in the Co-doped one to purely testify to the robustness of superconductivity against impurity scattering.

## 5.4 Summary

We have evaluated the impurity effects in IBSs of underdoped, optimally doped, and overdoped  $\text{Ba}_{1-x}\text{K}_x\text{Fe}_2\text{As}_2$  single crystals by means of 3-MeV  $\text{H}^+$  irradiation. All samples show a parallel shift of the  $\rho - T$  curves by the irradiation, which manifests that defects introduced by the irradiation are nonmagnetic and are not causing localization effects. Almost linear variations of  $\Delta\rho_0$  and  $T_c$  as a function of dose are obtained. The critical value of the normalized scattering rate  $g_c$  is estimated by three different methods. By assuming a realistic condition of similar magnitudes of intra- and inter-band scattering rates, all obtained  $g_c$ 's are much larger than  $g_c^\pm$ , excluding the  $s_\pm$ -wave state in  $\text{Ba}_{1-x}\text{K}_x\text{Fe}_2\text{As}_2$ .

## Chapter 6

# Proton irradiation effects on vortex pinning and dynamics

### 6.1 Introduction

In chapter 5, the effects of proton irradiation on the pair breaking are focused on. As a result of the proton irradiation, we recognized that the superconductivity is not easily destroyed by point defects. In the practical point of view, this property is very useful since a number of pinning centers can be introduced in IBSs without decreasing  $T_c$ . The almost isotropic superconducting property will also help the application of IBSs. Thus, the IBSs are anticipated to be used as a second class of high-temperature superconducting wire, and actually a lot of prototype of wires and tapes are successfully developed [36, 121, 122, 123, 124]. Although the overall (transport) critical current density is determined by the impurity phase present in the grain boundaries, the weak-link problem is not so severe due possibly to the smaller anisotropy. This is in contrast with cuprate tapes, where the texturing of grains is absolutely required to achieve a large transport current flow. Once the grain boundaries do not disturb the supercurrent flow, the key ingredient for high  $J_c$  is to enhance the intragrain  $J_c$ . For this purpose, the random point defects are the most promising candidate since an introduction of point defects is easily carried out by the inclusion of impurity atoms. In general, the random point defects produce a pinning potential for vortex motion. In addition, the cuprate superconductors show many interesting phenomena in vortex dynamics, such as giant-flux creep, thermally activated flux flow, and the theories to describe them have been elaborated in the last decades [21]. Especially,

collective pinning with weak pinning potential by the quenched disorder and collective creep of vortex bundles give rise to intriguing experimental results, such as “plateau” observed in temperature dependent normalized relaxation rate ( $S \equiv |d \ln M / d \ln t|$ ) [125], in contrast to the linear increase with temperature predicted by Anderson-Kim model in low-temperature superconductors. We therefore believe that the current importance is to clarify the effects of random point defects. The similarities between IBSs and cuprates, such as the shape of magnetization loop and the existence of giant-flux creep, indicate that these two systems share the common vortex physics. Moreover, how introduction of artificial pinning center affects flux dynamics or  $J_c$  is also interesting [126, 127]. Hence, the IBSs are suitable candidates to check whether glassy behavior of vortices is universal in all high-temperature superconductors. As we mentioned in Sec. 3.10, the vortex pinning and dynamics should be clarified to understand the vortex states in high-temperature superconductors. The fundamental character of vortex states in cuprates are overviewed in Chapter 3. However, the vortex states in IBSs have still not been identified. The main goal of our study is to clarify the fundamental properties of vortex state in IBSs and check the universality of them in high-temperature superconductors.

The pure effects of point defects are investigated with defects introduced by light-particle irradiation, which do not change the carrier number and the crystal structure. In this chapter, we show the proton-irradiation effects on the vortex system in mostly studied IBSs of  $\text{Ba}(\text{Fe}, \text{Co})_2\text{As}_2$  as well as  $(\text{Ba}, \text{K})\text{Fe}_2\text{As}_2$  system.

## 6.2 Optimally Co-doped $\text{BaFe}_2\text{As}_2$

In  $\text{YBa}_2\text{Cu}_3\text{O}_{7-\delta}$ ,  $J_c$  is enhanced and glassy behavior remains basically the same after proton ( $\text{H}^+$ ) irradiation, which is known to introduce point defects. This is also expected in IBSs. In fact, Haberkorn *et al.* recently reported that  $\text{H}^+$ -irradiation does not affect to  $H - T/T_c$  phase diagram in  $\text{Ba}(\text{Fe}_{0.925}\text{Co}_{0.075})_2\text{As}_2$  [93]. It is important to clarify how vortex dynamics is affected by  $\text{H}^+$ -irradiation in IBSs. Since this system is twin free and less anisotropic, it enables us to discuss intrinsic pinning and dynamic properties of vortices without complication. However, it is difficult to synthesize large and clean crystals especially in  $\text{LnFeAsO}$  ( $\text{Ln}$  is lanthanoid, so-called ‘1111’ system) [28]. This prevents us from discussing vortex dynamics due to strong inhomogeneities unless we use local probes [67]. Since high-quality single crystals are readily



available in  $AEFe_2As_2$  [30, 128], it is possible to discuss details of vortex pinning also in IBSs with global magnetic measurements. Actually, homogeneous flow of superconducting current in this system has been confirmed by magneto-optical measurement [34]. This is why we choose optimally Co-doped  $BaFe_2As_2$  single crystal.

### 6.2.1 Enhancement of screening current density

Figure 6.1 shows magnetic field dependence of the screening current density  $J_s$  in (a) pristine and (b)  $H^+$ -irradiated  $Ba(Fe_{0.93}Co_{0.07})_2As_2$ . It is obvious that  $H^+$  irradiation enhances  $J_s$  from  $1 \times 10^6$  A/cm<sup>2</sup> to  $2.5 \times 10^6$  A/cm<sup>2</sup> at 2 K under zero-field. In pristine sample,  $J_s$  is nearly constant below 1 kOe, followed by power law decay  $H^{-\alpha}$  at a field of 2-10 kOe with  $\alpha \sim 0.5$ . As discussed by van der Beek *et al.*, these behaviors at low-fields are attributed to sparse strong-point pinning centers, as in the case of  $YBa_2Cu_3O_{7-\delta}$  films [67, 66]. At a glance, it seems inappropriate to analyze it in the framework of collective-pinning-collective-creep and vortex glass theory. However, since strong-point-pinning contribution for temperature dependence of current density is smaller than weak-collective pinning (see Fig. 6 or 9 in Ref. [67]), we can approximate  $J(T)$  only by the contribution from collective creep (pinning). In  $H^+$ -irradiated sample, it is basically the same as the pristine one, although there is a wide-crossover region with  $\alpha \sim 0.3$  between low-field plateau and  $H^{-0.5}$  region. Such a weak field dependence has been also observed in  $YBa_2Cu_3O_7$  and  $YBa_2Cu_4O_8$  films by Griessen *et al.*, and they concluded that single vortex creep is achieved in this region [68].

### 6.2.2 Quantitative analyses in vortex dynamics

To elucidate the vortex dynamics, it is important to measure (static) magnetic relaxation rate  $S \equiv |d \ln M / d \ln t|$  in both samples, where  $M$  is the irreversible component of the magnetization,  $t$  is time from the moment when the critical state is prepared. In order to discuss temperature dependence of vortex dynamics, we fix magnetic field. However, as we mentioned above, there is a strong-pinning background, so that we have to select a field where the field dependence of  $J_s$  is similar for all temperatures to exclude field-dependent strong-point-pinning effect. Besides, we should carefully keep away from fish-tail effect with non-monotonic field dependence of  $J_s$  at high fields and self-field effect at low fields, which disturb direct extraction of typical parameters for vortex dynamics. Based on these consideration, we select  $H = 5$  kOe in both samples,

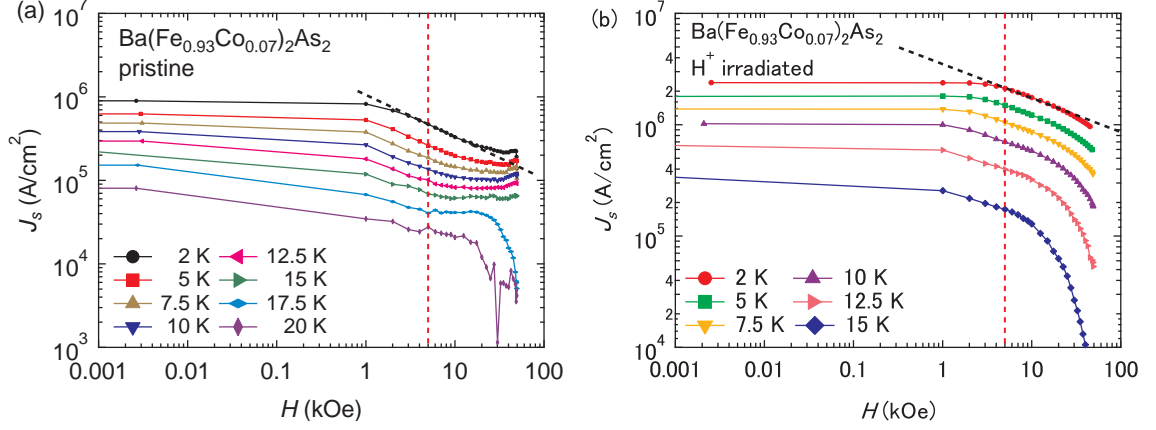


Figure 6.1: Field dependence of  $J_s$  in (a)pristine and (b) $H^+$  irradiated  $Ba(Fe_{0.93}Co_{0.07})_2As_2$  at several temperatures. Dotted line on  $\bullet$  (2 K) shows power-law decay of (a)  $H^{-0.5}$  and (b)  $H^{-0.3}$ , respectively. Vertical line indicates the field where we discuss the vortex dynamics,  $H = 5$  kOe.

shown as vertical broken lines in Fig. 6.1. Insets of Fig. 6.2 show temperature dependence of  $S$ . According to collective pinning theory [20], this is described by Eq. (3.72). One of the most remarkable results extracted from this equation is the prediction of plateau in the intermediate temperature range if  $U_0 \ll T$  [125]. The value of plateau  $S \sim 1/(\mu \ln(t/t_{\text{eff}}))$  falls in the range of 0.02-0.04 theoretically, which has been confirmed in  $YBa_2Cu_3O_{7-\delta}$  [125]. The inset of Fig. 6.2(a) is consistent with this behavior quantitatively, as observed in other IBSs [129, 69, 130]. This proves the validity of applying collective pinning theory to IBSs. Here we emphasize that it is quite important to determine the value of  $\mu$  in discussing vortex dynamics, since  $\mu$  includes information on the size of vortex bundle in collective pinning theory. In three-dimensional system, it is predicted as  $\mu = 1/7, 3/2, 7/9$  for single-vortex, small-bundle, and large-bundle regime, respectively [65], as explained in sec. 3.7. Inverse-current-density dependence of effective pinning energy  $U^* = T/S$  is convenient to extract this value.

We can define inverse power-law form of flux activation energy  $U(J)$  as Eq. (3.68). Combining this with  $U = T \ln(t/t_{\text{eff}})$  extracted from Arrhenius relation, we can deduce the so-called “interpolation formula” Eq. (3.71). From Eqs. (3.68) and (3.71),

$$U^* = U_0 + \mu T \ln(t/t_{\text{eff}}) = U_0 (J_{c0}/J)^\mu \quad (6.1)$$

is derived. Thus the slope in double logarithmic plot of  $U^*$  vs.  $1/J$  gives the value of  $\mu$ , shown in the main panels of Fig. 6.2. In this way, we evaluate  $\mu = 1.09$  and  $0.82$  for pristine and  $H^+$ -irradiated samples, respectively. Note that  $\mu \simeq 1$  in pristine crystal is often reported in  $YBa_2Cu_3O_{7-\delta}$  [1] and IBSs [70]. Contrary to the above prediction of  $\mu > 0$ , negative slope is observed at small  $J$ . This negative slope is often denoted as  $p$  in plastic creep theory with  $p = -0.5$ , and confirmed experimentally [74]. Our evaluation of  $p = -0.61$  in pristine sample is very similar to this value.

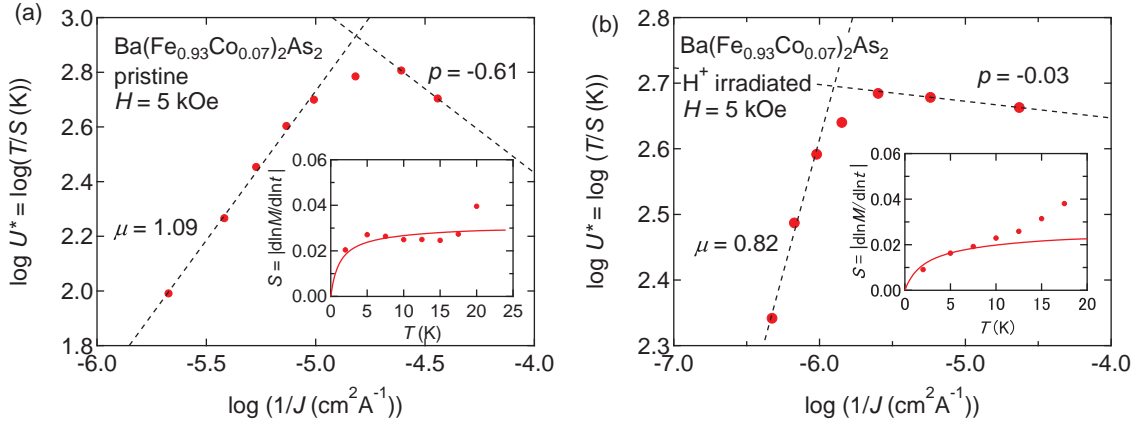


Figure 6.2: Inverse current-density dependence of effective pinning energy  $U^*$  in (a)pristine and (b) $H^+$  irradiated  $Ba(Fe_{0.93}Co_{0.07})_2As_2$ . Inset: Temperature dependence of normalized relaxation rate  $S$ . Solid line indicates fitting by Eq. (3.72).

To determine actual flux activation energy, we employ extended Maley's method. [131] Since temperature dependence of  $U$  is not considered in the original Maley's method, [73] it is impossible to scale  $U$  in a wide range of  $J$  even if glassy exponent is unique. In order to solve this problem, appropriate temperature dependences of  $U_0$  and  $J_{c0}$  are assumed as follows.

$$U_0(T) = U_{00}[1 - (T/T_c)^2]^n, \quad (6.2)$$

$$J_{c0}(T) = J_{c00}[1 - (T/T_c)^2]^n. \quad (6.3)$$

In order to simplify the problem, we choose the same exponents in Eq. (6.2) and Eq. (6.3). Here exponent  $n$  is set to  $3/2$ , as in the case of Ref. [1] and [131], while  $(1 - T/T_c)^{3/2}$  is selected in  $Ba_{1-x}K_xFe_2As_2$  [70].  $U = -T \ln[dM(t)/dt] + CT$  and  $C = \ln(B\omega a/2\pi r)$  is assumed as a

Table 6.1: Parameters obtained from extended Maley's method and inverse of plateau value in  $S(T)$ .

Sample	$J_{c0}$ (MA/cm <sup>2</sup> )	$U_{00}$ (K)	$\mu$	$\mu \ln(t/t_{\text{eff}})$
Pristine	0.85	41.2	1.01	35
H <sup>+</sup> irradiated	2.90	93.1	1.24	43

constant, where  $B$  is the magnetic induction,  $\omega$  is the attempt frequency for vortex hopping,  $a$  is the hopping distance, and  $r$  is the sample radius. We select  $C = 18$  and 20 for pristine and H<sup>+</sup>-irradiated samples, respectively. Figures 6.3 show current density dependence of  $U$  in (a)pristine and (b)H<sup>+</sup>-irradiated Ba(Fe<sub>0.93</sub>Co<sub>0.07</sub>)<sub>2</sub>As<sub>2</sub>, respectively, constructed by extended Maley's method. Solid lines indicate power-law fitting to large  $J$  region where the slope in Fig. 6.2 is positive. Note that deviation of the data from the fitting in the small  $J$  region is reasonable since creep is plastic there. The obtained glassy exponents are  $\mu = 1.01$  and 1.24 for pristine and H<sup>+</sup>-irradiated samples, respectively. For pristine sample, this value is nearly the same as that obtained in Fig. 6.2(a),  $\mu = 1.09$ . On the other hand, the change of  $\mu$  by H<sup>+</sup> irradiation has an opposite trend. Namely, the value of  $\mu$  decreases in Fig. 6.2(b), while grows in Fig. 6.3(b) after H<sup>+</sup>-irradiation. This is because the vortex system in H<sup>+</sup>-irradiated sample crossovers from elastic to plastic creep more gradually, as we can see in the main panel and inset of Fig. 6.2(b). Hence we may underestimate  $\mu$  and overestimate  $p$  with the scheme of Fig. 6.2, and it is more reliable to estimate it from the extended Maley's method of Fig. 6.3, which uses more data points. For this reason, we conclude that  $\mu$  is slightly increased by H<sup>+</sup> irradiation. Additionally, slight increase of  $\mu$  is consistent with the regime of measurement, where it is closer to small bundle regime with  $\mu = 3/2$ , as we discussed in Fig. 6.1. Other resultant parameters are summarized in Table 6.1. With these  $U_{00}$ , temperature dependence of  $S$  is fitted by Eq. (3.72) with a single free parameter of plateau value  $S^{\text{sat}} = 1/\mu \ln(t/t_{\text{eff}})$  as shown in the inset of Fig. 6.2. The inverse of this value is also shown in Table 6.1.

Using parameters obtained above, we calculate  $J$  after creep from attempt function of (true) critical current density Eq. (6.3), which is shown as lower solid line in Fig. 6.4. In both cases,  $J$  is reasonably reproduced, especially at high  $J$  region (i.e. at low temperature). This means that the present collective pinning/creep analysis is appropriate. To get more insight into pinning mechanism in IBSs, we also show a function of  $\delta T_c$ - and  $\delta l$ -pinning in Fig. 6.4. These functions

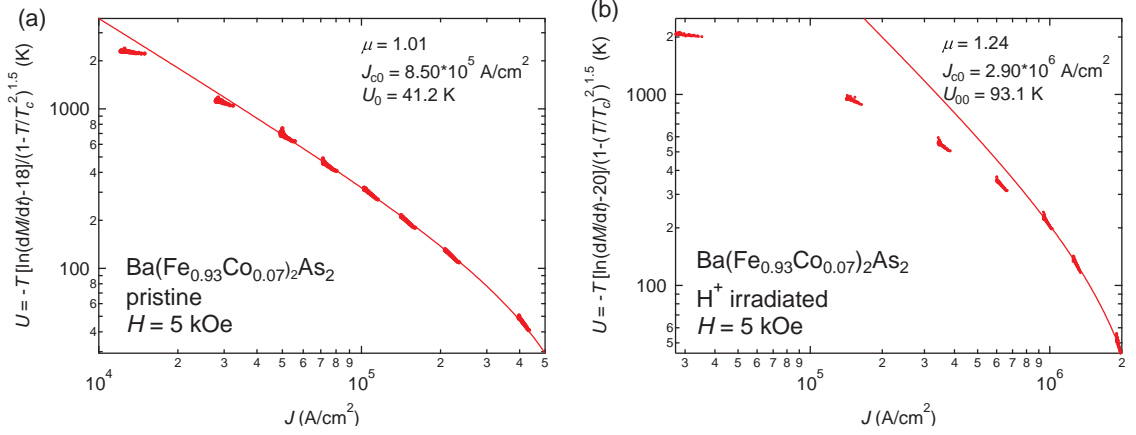


Figure 6.3: Current density ( $J$ ) dependence of the vortex pinning energy ( $U$ ) in (a) pristine and (b)  $H^+$ -irradiated  $\text{Ba}(\text{Fe}_{0.93}\text{Co}_{0.07})_2\text{As}_2$  constructed by extended Maley's method. Solid line indicates power-law fitting in large  $J$  region.

are written as  $J_c(t)/J_c(0) = (1 - t^2)^{7/6}(1 + t^2)^{5/6}$  and  $(1 - t^2)^{5/2}(1 + t^2)^{-1/2}$ , respectively. [68] From this figure, our model function of  $J_c$  can be considered as a superposition of the two pinning mechanisms. To discuss such a mechanism, generalized inversion scheme (GIS) is utilized. [132, 133] Although in this scheme, we have to assume empirical temperature dependence of penetration depth  $\lambda$  and coherence length  $\xi$  as  $\propto (1 - t^4)^{-1/2}$  and  $\propto (1 + t^2)^{1/2}(1 - t^2)^{-1/2}$ , respectively, we can directly reconstruct true critical current density  $J_c$  from  $J_s$  and discuss pinning mechanism. When we assume  $\ln(t/t_{\text{eff}}) \sim 23$  in the measurement with field sweeping, and choose parameters for three-dimensional single vortex pinning,  $J_c$  is reconstructed as shown in Fig. 6.4, which are in reasonable agreement with the model function. Similar analyses of pinning mechanism using GIS in pristine  $\text{Ba}(\text{Fe}_{1-x}\text{Co}_x)_2\text{As}_2$  have been attempted in Ref. [24]. They also conclude that both  $\delta T_c$ - and  $\delta l$ -mechanisms are working in this system. Here, we want to compare our work with similar work by Haberkorn *et al.* [93] In their work, temperature dependence of (measured) current density  $J(T)$  is used to discuss the pinning mechanism in pristine and proton-irradiated  $\text{Ba}(\text{Fe}_{1-x}\text{Co}_x)_2\text{As}_2$ . However, identification of pinning mechanism using  $J(T)$  is only empirical and lacks firm physical background. So, although their conclusion and our conclusion on the pinning mechanism are similar, we believe that our identification of pinning mechanism is more appropriate.

We can basically describe physical quantities for vortex system by means of collective creep

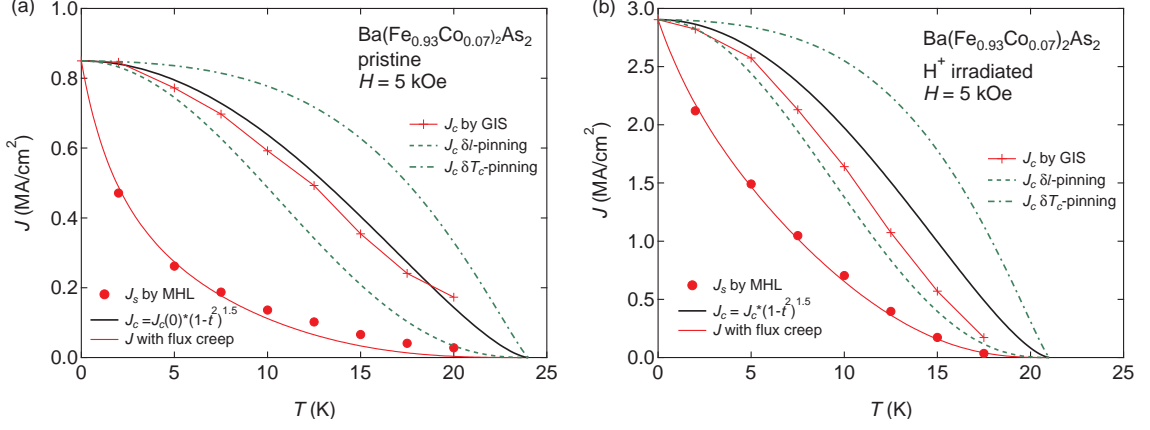


Figure 6.4: Temperature dependence of  $J_s$  ( $\bullet$ ), model function of  $J_c$  before and after creep with the parameters in Table 6.1 (solid line),  $\delta T_c$ - and  $\delta l$ -pinning (dashed line) and  $J_c$  reconstructed by GIS (+) in (a)pristine and (b) $H^+$ -irradiated  $Ba(Fe_{0.93}Co_{0.07})_2As_2$ .

theory both in the case of pristine and  $H^+$ -irradiated  $Ba(Fe_{0.93}Co_{0.07})_2As_2$ . It is noteworthy that the effect of  $H^+$  irradiation can be summarized as  $U_{00}$  enhancement, without replacing model function  $U_0(T)/U_{00}$  and  $J_0(T)/J_{00}$ . Namely, we can conclude that the effect of  $H^+$  irradiation is enhancement of the collective pinning force by increasing weak-point-pinning centers without a drastic change of pinning mechanism.

Finally, we comment on the absolute value of  $J$  instead of  $J(T)/J(0)$ .  $J$  is determined by the sum of weak-collective-pinning contribution  $J^{wcp}$  and strong-point-pinning contribution  $J^{spp}$ . [67] Instead, if we assign  $J$  to  $J^{spp}$  in the absence of flux creep (so that we write  $J$  as  $J_c$  here), we can estimate upper limit of strong-pinning center fraction in the crystal. In the strong pinning theory [66], critical current density is written as  $J_c \approx 0.14\sqrt{n}\gamma[DF(T)]^{3/2}J_0$ . Here,  $J_0 = c\phi_0/12\sqrt{3}\pi^2\xi_{ab}\lambda_{ab}^2$  is depairing current density,  $\gamma = H_{c2}^{ab}/H_{c2}^c$  is anisotropy parameter,  $n$ ,  $D$  are density and diameter of pinning centers, respectively. Assuming  $D$  as several times of  $\xi_{ab}$ , we can simplify  $F(T) \approx \ln[1 + D^2/8\xi^2(T)] \approx 1$ . Using pinning center volume  $\nu \approx D^3/2$ ,  $n\nu = (J_c/J_0)^2(\sqrt{2} \times 0.14\gamma)^{-2} \approx 0.05\%$  with  $\xi_{ab} \sim 34 \text{ \AA}$  from  $H_{c2}(0) \sim 280 \text{ kOe}$  [34] and  $\lambda_{ab} \sim 2000 \text{ \AA}$ . [134] This value is similar to the value reported in Na-doped  $CaFe_2As_2$ . [130]

### 6.2.3 Summary

In summary, we have studied the effect of proton irradiation up to  $1.2 \times 10^{16} \text{ cm}^{-2}$  in optimally Co-doped  $\text{BaFe}_2\text{As}_2$  single crystals. Critical current density under self-field is enhanced by a factor of 2.5 at 2 K. Temperature dependence of critical current density and normalized flux relaxation rate is interpreted by collective creep theory. With Maley's method, a glassy exponent  $\mu \sim 1$  and variation of barrier height for flux creep  $U_{00} \sim 41 \text{ K}$  to  $93 \text{ K}$  are directly determined. To explain the value of  $J$  after the creep from the model function of  $J_c$ ,  $J_c$  is concluded to be controlled by both  $\delta T_c$ - and  $\delta l$ -pinning. This model function is consistent with the result of generalized inversion scheme. Proton irradiation effect is concluded as doubling of barrier height in the absence of flux creep.

## 6.3 Optimally K-doped $\text{BaFe}_2\text{As}_2$

The electron-doped system of  $\text{Ba}(\text{Fe}_{1-x}\text{Co}_x)_2\text{As}_2$  with high quality is readily available, so that the vortex dynamics in this material is intensively investigated as a prototypical system [69, 34, 135, 93, 136]. The vortex phase diagram in this material is similar to cuprate superconductors such as  $\text{YBa}_2\text{Cu}_3\text{O}_{7-\delta}$ , which has an elastic phase at low temperatures ( $T$ ) and low magnetic fields and a plastic phase at high temperatures and high fields, as well as vortex liquid phase in the vicinity of the superconducting transition. In addition to a variety of vortex phases, a sizable  $J_c$  over  $10^5 \text{ A/cm}^2$  is achieved at low temperatures, which exceeds the technically required value.

By means of flux creep experiments, the dynamical behavior of vortices can be determined [20]. The most notable feature in high-temperature superconductors is the very fast decay of screening current density with time, so-called “giant flux creep” [137]. Not only high  $J_c$  but also reasonably small flux relaxation rates are required for technological application. From such a point of view, the effect of artificial defects on vortex pinning and dynamics are interesting and important. Actually,  $J_c$  in proton ( $\text{H}^+$ )-irradiated YBCO is considerably enhanced, although the irreversibility line and the pinning potentials are little affected [138, 1]. In IBSs, the stability of irreversibility line to  $\text{H}^+$ -irradiation has also been confirmed [93]. The pinning force depends on the defect size and its morphology. Columnar defects introduced by swift heavy-ion irradiation are very effective in pinning vortices [126, 127], since columnar defects can trap vortices with one-dimensional structures perfectly and work as strong pinning centers.

On the other hand, point defects are introduced by the light-particle irradiation, for example electrons,  $H^+$ -ions, and  $\alpha$ -particles. Evidence for such defects formation is provided by an increase of residual resistivity in dc transport measurements in both YBCO [59, 60, 17, 61] and  $Ba(Fe_{1-x}Co_x)_2As_2$  [62, 18].

As a counterpart of  $Ba(Fe_{1-x}Co_x)_2As_2$ , a hole-doped  $Ba_{1-x}K_xFe_2As_2$  must be compared. Superconductivity in this material appears by a substitution to the blocking layer, which is in sharp contrast to the doping in Fe sites. In the case of Co doping, since dopant atoms are on the superconducting FeAs sheets, and consequently work as quasiparticle scatterers, the intrinsic disorder is expected. Intuitively, the fluctuation of dopant-atom density results in the fluctuation of a local superconducting order parameter and/or that of superconducting carrier density. This is actually confirmed by a detailed flux-creep analysis, characterized by both  $\delta T_c$  and  $\delta l$  pinning mechanisms [136]. On the other hand, since K-dopants are far from conducting layer, the effect of doping fluctuation on vortex pinning is expected to be weaker, so that the inherent pinning will be dominated by another origin such as sparse strong pinning centers. This perspective should be verified. If the pinning in K-doped system is really weaker than Co-doped one, it is intriguing to know if the collective pinning property is recovered by introducing point pinning centers.

In this section, we refer to the vortex pinning properties in hole-doped  $Ba_{0.6}K_{0.4}Fe_2As_2$  with optimal doping before and after the introduction of point defects. In the pristine sample, the magnetization loops are characterized by a sharp central peak as in the case of other IBSs. With increasing temperature, the fast shrinkage of the loops is observed, which means that  $J_c$  is strongly suppressed with elevating  $T$ . The concomitant normalized relaxation rate ( $S$ ) also depends on  $T$ , attributed to vortex bundle crossover or the vicissitude of different pinning mechanisms, namely the strong and weak-collective pinning. The magnetic-field ( $H$ ) dependence of  $S$  manifests a strong self-field effect in a wide range of  $H$  especially at low  $T$ . In  $H^+$ -irradiated sample, on the other hand, the central peak is broadened, leading to weakened  $T$  and  $H$  dependence of  $J_c$ . Regarding the vortex dynamics, the value of  $S$  and its  $H$  dependence becomes weaker, and  $T$  dependence becomes monotonic. This can be understood if irradiation-introduced point defects by irradiation work as weak-collective pinning centers.



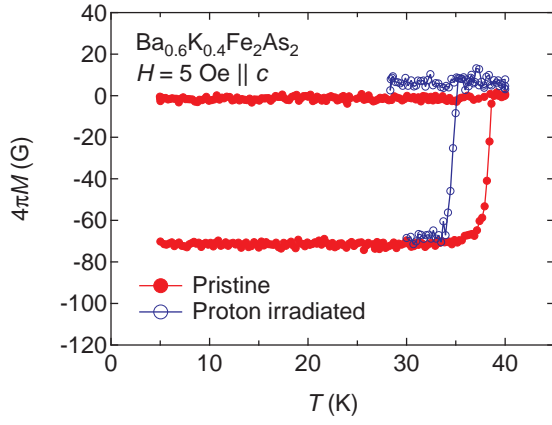


Figure 6.5: Temperature dependence of the magnetization under  $H = 5$  Oe along  $c$ -axis in pristine and  $H^+$ -irradiated  $\text{Ba}_{0.6}\text{K}_{0.4}\text{Fe}_2\text{As}_2$ .

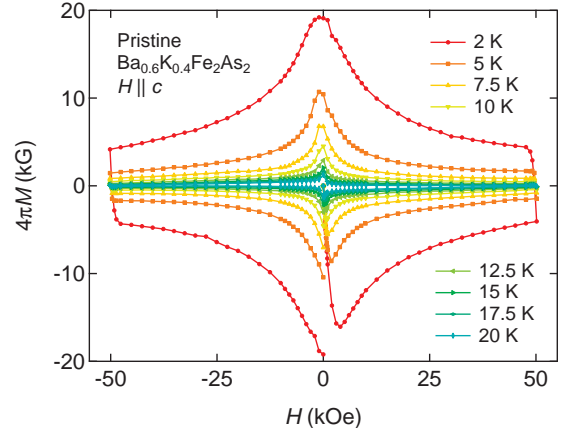


Figure 6.6: Magnetization loops under  $H||c$  in pristine  $\text{Ba}_{0.6}\text{K}_{0.4}\text{Fe}_2\text{As}_2$  at several temperature.

### 6.3.1 Pristine $\text{Ba}_{0.6}\text{K}_{0.4}\text{Fe}_2\text{As}_2$

First, we start with the analysis of pristine  $\text{Ba}_{0.6}\text{K}_{0.4}\text{Fe}_2\text{As}_2$ . The onset of Meissner response under  $H = 5$  Oe along  $c$ -axis occurs at a critical temperature  $T_c = 38.6$  K, as shown in Fig. 6.5. To clarify the fundamental vortex pinning properties, we have measured hysteresis loops under  $H||c$  at several temperatures as shown in Fig. 6.6. The loop at 2 K is almost symmetric with respect to both  $H$ - and  $M$ -axes, indicating that bulk pinning dominates. As higher  $T$ , the width of  $\Delta M = M_{\text{down}} - M_{\text{up}}$  rapidly shrinks, where  $M_{\text{up}}$  and  $M_{\text{down}}$  are  $M$  measured at  $H$  sweeping up and down, respectively. According to the Bean critical state model [63, 64], this  $\Delta M$  is proportional to the in-plane screening current density  $J$  through the form of Eq. (3.12). The calculated  $J$  in Fig. 6.7(a) has a reasonably large value up to  $2.4 \times 10^6$  A/cm<sup>2</sup> at  $T = 2$  K and  $H = 0$ , larger than the self-field  $J(2 \text{ K}) = 1 \times 10^6$  A/cm<sup>2</sup> in optimally Co-doped  $\text{BaFe}_2\text{As}_2$  [34, 129]. The values are almost the same magnitude as those reported in the same compounds [139, 102].

To investigate the corresponding vortex dynamics due to flux creep, we have traced the magnetization with time  $M(t)$  for an hour, where  $t$  is the time from the moment that the critical state is created. The normalized relaxation rate  $S = |\text{dln}M/\text{dln}t|$  as a function of  $H$  is depicted in Fig. 6.7(b). At low  $H$ , a characteristic dip structure can be identified as in the case of Co-doped  $\text{BaFe}_2\text{As}_2$  [129, 140, 127] and  $\text{FeTe}_{1-x}\text{Se}_x$  [141, 142]. The peak position shifts to lower  $H$  at higher  $T$ , with a larger value of  $S \simeq 0.06$ . This value is consistent with that reported

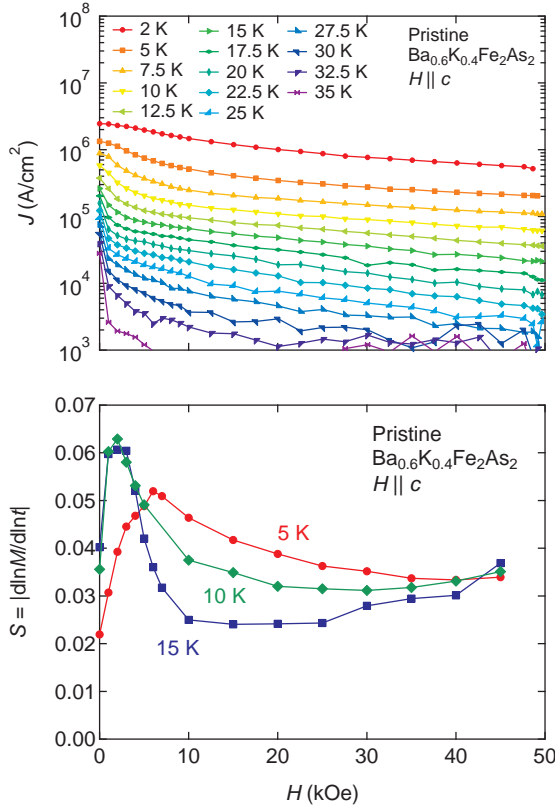


Figure 6.7: (a) Field dependence of in-plane screening current density  $J$  under  $H||c$  at several temperature and (b) the normalized relaxation rate  $S$  at 5, 10, and 15 K under  $H||c$  in pristine  $\text{Ba}_{0.6}\text{K}_{0.4}\text{Fe}_2\text{As}_2$ .

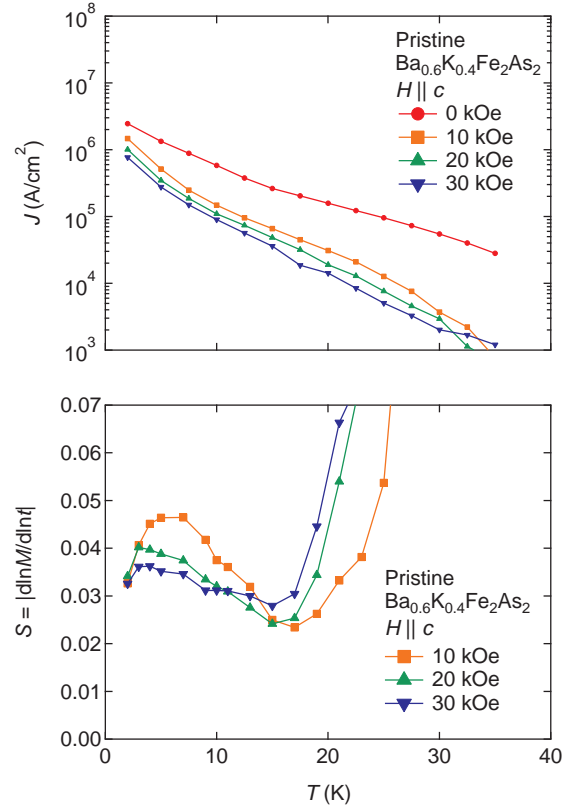


Figure 6.8: (a) Temperature dependence of in-plane screening current density  $J$  at  $H = 0$ , 10, 20, and 30 kOe and (b) the normalized relaxation rate  $S$  at  $H = 10$ , 20, and 30 kOe under  $H||c$  in pristine  $\text{Ba}_{0.6}\text{K}_{0.4}\text{Fe}_2\text{As}_2$ .

in the same system for  $H = 6$  kOe at  $T = 8$  K [143]. We point out the difference between our study and Ref.[143], in which the creep study less than  $H = 10$  kOe is focused on. Our creep study with a wide range of  $H$  up to 50 kOe manifests that the low- $H$  behavior is not typical. The vortex creep study at low  $H$  must include this self-field effect. The self-field effect usually suppresses  $S$ , which is because Meissner hole appears at the sample edge [144]. The anomalously large  $S$  value at low  $H$  is coming from the single vortex pinning, as concluded in Ref. [143], but the self-field effect should be taken into account.

Above the self-field dominant region, the  $H$  dependence is determined by the variation of glassy exponent  $\mu$ , as observed in  $\text{YBa}_2\text{Cu}_3\text{O}_{7-y}$  [22]. As increasing  $H$ ,  $S$  at  $T = 10$  K drops to the value of  $S = 0.03 - 0.04$ , followed by a gradual increase, which is attributed to successive changes from single vortex to small bundle and large bundle regimes. At higher  $T = 15$  K, the drop is faster and reaches a smaller value of  $S = 0.02 - 0.03$ . On the other hand, at lower  $T$

of 5 K, the suppression rate of  $S$  is small, starting from  $H = 6$  kOe. Such a  $T$  dependence is consistent with  $H - T$  phase diagram in the framework of collective pinning theory. Namely, the characteristic  $H$  such as self field and crossover field becomes smaller at elevated  $T$ . At  $H = 45$  kOe, the  $T$  dependence of  $S$  is negligible with a value of  $S = 0.03 - 0.04$ . Figure 6.8(b) indeed demonstrates that  $S$  becomes more insensitive to  $T$  when  $H$  becomes higher. By contrast, at lower field of  $H = 10$  kOe,  $S$  nonmonotonically changes at low  $T$ , subsequently crossovers to plastic creep phase at high  $T \geq 17$  K with very large  $S$ . The weak-collective pinning theory predicts that  $S$  behaves as Eq. (3.72), and has a plateau at intermediate  $T (\gg U_0/k_B)$  with a value of  $S = 0.02 - 0.04$ . Considering that the contribution of the strong pinning becomes weaker at high  $H$ , we have indeed observed weak-collective pinning behavior at high  $H$  both with qualitative and quantitative agreement.

Figure 6.8(a) shows a  $T$  dependence of  $J$ . Almost exponential decay of  $J$  is observed at all  $H$ , where  $J$  changes by a factor of 10 for every  $\sim 10$  K, except for  $H = 0$  with a gradual slope.

### 6.3.2 $H^+$ -irradiated $\text{Ba}_{0.6}\text{K}_{0.4}\text{Fe}_2\text{As}_2$

The variation of  $J$  and vortex dynamics after the introduction of weak-pinning centers by means of proton irradiation have been examined. The sample with a dose of  $5.8 \times 10^{16}$   $H^+$  ions/cm<sup>2</sup> has  $T_c = 35.1$  K without broadening in magnetic transition, as shown in Fig 6.5. Note that the suppression of  $T_c$  shows a sharp contrast to that in heavy-ion (1.4 GeV Pb) irradiated  $\text{Ba}_{0.6}\text{K}_{0.4}\text{Fe}_2\text{As}_2$  with a dose of  $B_\phi = 21$  T =  $1.0 \times 10^{12}$  ions/cm<sup>2</sup>, which demonstrates almost no effect of columnar defects on  $T_c$ . [102] In accordance with a large amount of point defects, vortex pinning behavior changes considerably compared with the pristine sample. Figure 6.9 shows hysteresis loops under  $H$  parallel to  $c$  in the  $H^+$ -irradiated  $\text{Ba}_{0.6}\text{K}_{0.4}\text{Fe}_2\text{As}_2$ . The significant broadening of the central peak can be seen at 2 K, while another notable feature of a dip structure is evolved from 5 to 20 K. This broadening and dip structures have been also observed in 1.4 GeV Pb irradiated  $\text{Ba}_{0.6}\text{K}_{0.4}\text{Fe}_2\text{As}_2$ , [102] as well as 2.6 GeV U irradiated  $\text{Ba}(\text{Fe}_{0.93}\text{Co}_{0.07})_2\text{As}_2$ . [127] The corresponding  $J$  calculated using Eq. (3.12) is depicted in Fig. 6.10(a). The self-field  $J$  at 2 K reaches  $1.1 \times 10^7$  A/cm<sup>2</sup>. This value is one of the highest reported ever in  $\text{Ba}_{1-x}\text{K}_x\text{Fe}_2\text{As}_2$  [124]. The enhancement factor  $\sim 5$  in  $J$  is surprisingly large compared with  $H^+$ -irradiated  $\text{Ba}(\text{Fe}_{0.93}\text{Co}_{0.07})_2\text{As}_2$  of  $\sim 2.5$ . This is probably because of the cleanness of the pristine sample. Namely, the Co-doped sample originally has weak-pinning

centers of Co dopant in FeAs plane, while K-doped sample does not. The  $H$  dependence of  $J \propto H^{-0.5}$  in the pristine sample, mentioned above, is replaced by  $J \propto H^{-0.3}$ . This change is the same as we reported in  $H^+$ -irradiated  $\text{Ba}(\text{Fe}_{0.93}\text{Co}_{0.07})_2\text{As}_2$ . [136] Another peculiar feature in hysteresis loops is the very broad return branch from  $M_{\text{up}}$  to  $M_{\text{down}}$ , and *vice versa*. The  $H$  width of the return branch is estimated as twice of the self field  $H^* \sim J \times t$ , where  $t = 20 \mu\text{m}$  is the sample thickness. Using almost field-independent  $J \simeq 1 \times 10^7 \text{ A/cm}^2$  at  $T = 2 \text{ K}$ , we get an evaluation of  $\sim 20 \text{ kOe}$ , which is consistent with the experimental value. Besides, a fast suppression with  $T$  observed in the pristine sample in Fig. 6.6 is not applicable in  $H^+$ -irradiated sample. This means that  $J$  is not easily suppressed at elevated temperatures. We can clearly see this in Fig 6.11(a), where  $J$  changes by a factor of 10 by increasing  $T$  by  $\sim 35 \text{ K}$ .

Not only on the enhancement of  $J$ , introduced point defects have an effect also on vortex dynamics. First we inspect the field dependence of  $S$  in  $H^+$ -irradiated sample. As we can see in Fig. 6.10(b), the low field peak structure is eliminated, and  $S$  becomes almost field independent. The highest value is limited to  $S \simeq 0.03$  at  $T \leq 25 \text{ K}$ . This is in sharp contrast with the behavior in the pristine sample depicted in Fig. 6.8(b), where most of the points are  $S \geq 0.03$ . The low-field drop can be observed less than  $H^* \sim J \times t$  and the minimum of  $S$  locates at  $H = 0$  for  $T = 15 \text{ K}$  and  $25 \text{ K}$ , which is very similar to low- $T$  behavior in  $H^+$ -irradiated  $\text{Ba}(\text{Fe}_{0.93}\text{Co}_{0.07})_2\text{As}_2$ . [145, 140, 127] At  $T = 5 \text{ K}$ , on the other hand, the behavior is different from that at high  $T$ , and similar to 200 MeV Au-irradiated  $\text{Ba}(\text{Fe}_{0.93}\text{Co}_{0.07})_2\text{As}_2$  at  $T = 5 \text{ K}$ . [129, 127] Namely, the minimum of  $S \simeq 0.01$  locates at intermediate  $H$  and  $S$  gradually goes up at  $H \rightarrow 0$ . In contrast to the pristine sample, data points at different  $T$  do not cross, indicating a monotonic  $T$  dependence for all  $H$ . This can be clearly seen in Fig. 6.11(b). A gradual increase at all  $T$  is similar to the  $H^+$ -irradiated  $\text{Ba}(\text{Fe}_{0.93}\text{Co}_{0.07})_2\text{As}_2$ , [145] while the slope at intermediate  $T$  is small and the plateau-like feature is identified with  $S \simeq 0.02$  for all measured  $H$ .

### 6.3.3 Discussion

The pinning property is examined by  $H$  and  $T$  dependence of  $J$ . As in the case of most of as-grown IBSs, [139] the drop of  $J(H)$  at the central peak follows  $J \propto H^{-\alpha}$  due to strong pinning by the sparse nm-sized defects, where  $\alpha = 0.5 - 0.625$ . [146, 66] This is depicted in Fig. 6.12(a). At high fields, we have not observed any nonmonotonic behavior. One of the notable differences from

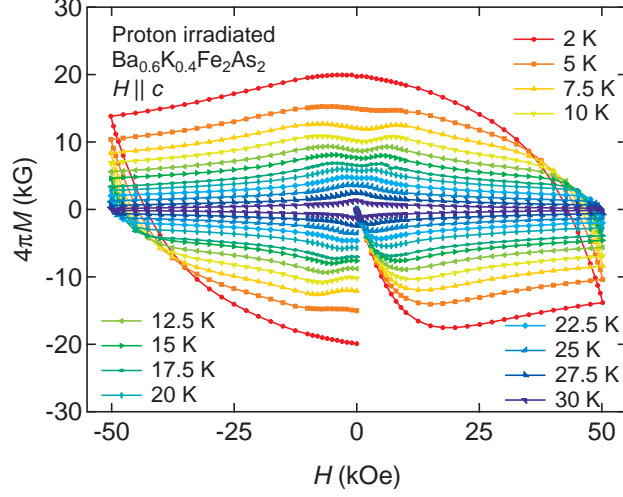


Figure 6.9: Magnetization loops under  $H||c$  in  $H^+$ -irradiated  $\text{Ba}_{0.6}\text{K}_{0.4}\text{Fe}_2\text{As}_2$  at several temperature.

$\text{Ba}(\text{Fe}_{1-x}\text{Co}_x)_2\text{As}_2$  is the absence of fish-tail effect, namely, nonmonotonic field-dependence of  $J$ . This is consistent with Ref.[102], while obvious fish-tail effects are observed even at intermediate  $T$  in previous reports. [147, 70] In our case, the fish-tail effect is not observed up to  $H = 50$  kOe or limited only very close to  $T_c$ . Note that in  $\text{Ba}_{0.5}\text{K}_{0.5}\text{Fe}_2\text{As}_2$  we indeed observed such a high- $T$  fish-tail effect. [148] The following  $H$  dependence of  $J$  has faster suppression with  $\alpha > 0.5$  at high  $H$ . Neither  $H$  independent behavior nor upturn behavior is observed. The absence of fish-tail effect is pointed out in isovalently substituted  $\text{BaFe}_2(\text{As}_{1-x}\text{P}_x)_2$ , [139, 149, 150] which is understood only by the innately included strong pinning centers. By contrast, most of other IBSs contain weak-pinning sites such as oxygen vacancies and charged dopant atoms, so that  $J$  is composed of both strong pinning and weak-collective pinning contributions. These charged quasi-particle scattering centers are considered as the origin of fish-tail effect. [139] In this scenario,  $\text{Ba}_{1-x}\text{K}_x\text{Fe}_2\text{As}_2$  should show nonmonotonic  $H$  dependence of  $J$ , and indeed observed it previously, so that what we observe in the pristine sample is inconsistent with the scenario above. As an opposite exception, the existence of fish-tail effect is reported in isovalent system such as  $\text{Ba}(\text{Fe}_{1-x}\text{Ru}_x)_2\text{As}_2$ ,  $\text{LiFeAs}$ , [150] and  $\text{FeTe}_{1-x}\text{Se}_x$ . [151, 141, 152, 142] These exceptions are possibly explained by the sample quality, since artificially introduced point defects by energetic electron irradiation are reported to invoke fish-tail effect. [150] However, the absence of fish-tail effect in the charge-doped system is hardly accountable in the framework of the scenario. So, we believe that, in our crystal, the contribution of the weak-collective pinning is much smaller

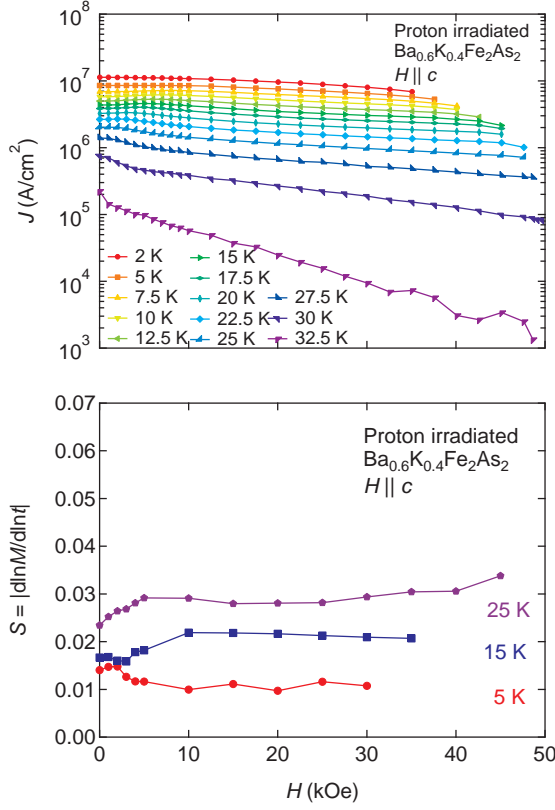


Figure 6.10: (a) Field dependence of in-plane screening current density  $J$  under  $H||c$  at several temperature and (b) the normalized relaxation rate  $S$  at 5, 10, and 25 K under  $H||c$  in  $H^+$ -irradiated  $Ba_{0.6}K_{0.4}Fe_2As_2$ .

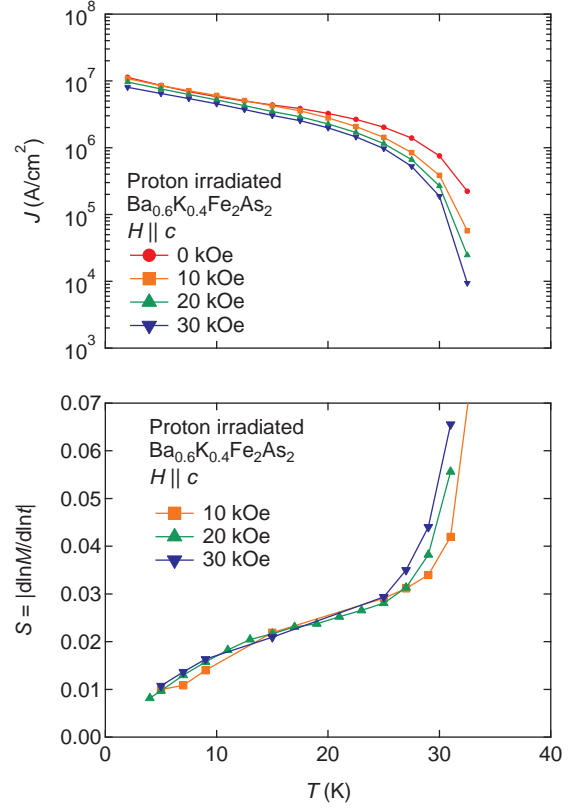


Figure 6.11: (a) Temperature dependence of in-plane screening current density  $J$  at  $H = 0, 10, 20, \text{ and } 30$  kOe and (b) the normalized relaxation rate  $S$  at  $H = 10, 20, \text{ and } 30$  kOe under  $H||c$  in  $H^+$ -irradiated  $Ba_{0.6}K_{0.4}Fe_2As_2$ .

than the strong pinning and/or the onset of fish-tail effect is shifted to higher  $H$  because the sample quality in this study is high. However we cannot exclude the absence of fish-tail effect if a sample is free from defects, and the high- $H$  fish-tail effect is originated from defects included even in the pristine sample, similar to the electron-irradiated  $BaFe_2(As_{1-x}P_x)_2$ .

The vortex dynamics must be compared with the counterpart-doped system of electron-doped  $Ba(Fe_{1-x}Co_x)_2As_2$ . In the pristine Co-doped  $BaFe_2As_2$ , we have observed the plateau in  $S(T)$  at intermediate  $T$ . [136] This plateau is a fingerprint of the weak-collective pinning in high- $T$  superconductors, often observed in cuprates. [125, 20] By contrast, pristine K-doped  $BaFe_2As_2$  lacks this feature even at relatively large  $H \simeq 20$  kOe. Only at  $H \geq 30$  kOe the plateau feature is recovered, as can be seen in Fig. 6.8(b) and Fig. 6.7(b). A similar but a smaller feature can be seen in pristine  $Ba(Fe_{1-x}Co_x)_2As_2$ . [93] This difference suggests the material dependent inherent pinning property. Namely, Co dopant atoms themselves work as pinning centers, while K atoms

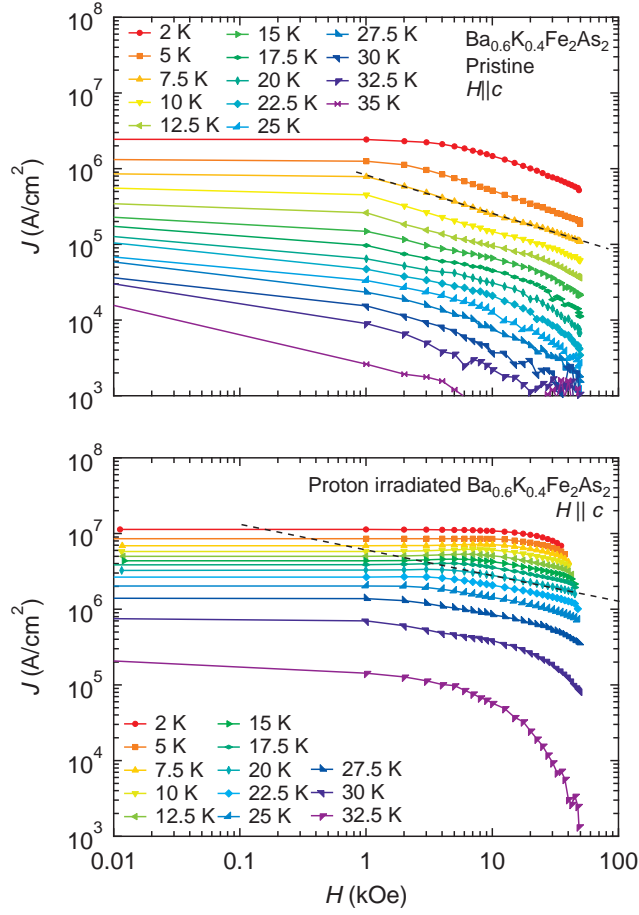


Figure 6.12: (a) A log-log plot of Fig. 6.7(a) and (b) that of Fig. 6.10(a). The broken lines indicates  $J \propto H^{-\alpha}$  with (a)  $\alpha = 1/2$  and (b)  $\alpha = 1/3$ .

do not. The difference originates from the doping site. In the former system, Co substitutes Fe sites. The substitution in the Fe sites, which compose Fermi surfaces in IBSs, largely affects the superconductivity, including the vortex pinning property by means of  $\delta T_c$  and  $\delta l$  pinning mechanisms. [136] Such a dopant-derived pinning is similar to the oxypnictide superconductors  $\text{PrFeAsO}_{1-y}$  and  $\text{NdFeAsO}_{1-x}\text{F}_x$  by oxygen vacancies or fluorine dopant atoms, [67] while these dopant atoms are located in blocking layer. According to Ref. [67], the dopant atoms or vacancies participate in the weak-collective pinning. The pinning by Co dopant atoms is similar to this case. In the latter system of K-doped  $\text{BaFe}_2\text{As}_2$ , the situation is different because the K dopant is far from FeAs layers but sits in Ba-blocking layer. As a result, K dopant atoms do not work as weak-collective pinning centers. Such an intuitive insight is indirectly confirmed by the residual resistivity in dc transport measurement, which manifests that the disorder is small as doping sites are far from Fe sites. [7] Since the K-doped system is intrinsically cleaner than the Co-

doped system, we can hardly observe the weak-collective pinning character of plateau in  $S(T)$  in the pristine K-doped sample. The fact that the crossover to plastic creep regime happens at a relatively low  $T \simeq T_c/2$  supports this perspective. Instead, we have observed nonmonotonic behavior both in  $S(H)$  and in  $S(T)$ . In the high- $T$  limit,  $S$  is proportional to  $1/\mu$  according to the weak-collective pinning theory, so naively this nonmonotonicity of  $S$  can be attributed to the variation of  $\mu$ . Since  $\mu$  is related to the vortex bundle size, this means that the vortex bundle size is highly sensitive to  $T$  and  $H$ . Reviewing Fig. 6.8(b), the variation of  $S(T)$  is strongest at  $H = 10$  kOe, suggesting the sensitivity of  $\mu$  is higher at low  $H$  especially. However, Konczykowski *et al.* concluded that  $\mu$  is almost  $H$  independent at  $H < 10$  kOe. [143] These two results are contradictory. One possible reason is that the analysis adopted in Ref. [143] is not adequate because the self-field effect is not properly considered. The value of self field is similar between their and our studies, so that, at the  $H$  region of interest, the vortices at the sample edge are strongly curved. This is why the dynamics in this region are difficult to approach. Another probable reason is the presence of two different pinning, i.e., the strong pinning and the weak-collective pinning. At low  $H$ , the strong pinning is dominant as indicated by the behavior of  $J \propto H^{-0.5}$ , while the weak-collective pinning dominates at high  $H$ . In fact, the positive slope in  $S(T)$  is suggested at  $H \geq 45$  kOe in Fig. 6.7(b) within the range of  $0.03 < S < 0.04$ . This means that  $S(T)$  at low  $H$  is not described by a simple weak-collective-pinning scenario if the strong pinning is  $T$  dependent. Although we can ignore the  $T$  dependence of strong pinning in Co-doped BaFe<sub>2</sub>As<sub>2</sub>, as in the case of other IBSs, this is unmasked if the weak collective pinning contribution is small, probably which is the case in the present system. Another example to show small contribution of weak-collective pinning in the pristine sample is that the anomalous  $S$  behavior cannot be seen when the strong pinning contribution becomes negligible due to the introduction of weak collective pinning centers. In H<sup>+</sup>-irradiated sample, monotonic and plateau-like feature is recovered. This suggests that elementary pinning force of point defects introduced by irradiation is small and work as weak-pinning centers, hence the vortex system is subscribed by simple vortex glass theory with a unique  $\mu$ . Besides, a large enhancement of  $J$ , and a shift-up of both irreversibility line and crossover line from collective to plastic creep are realized by a significant enhancement of the total pinning energy.



### 6.3.4 Summary

We have investigated critical current density and vortex dynamics in the pristine and proton-irradiated  $\text{Ba}_{0.6}\text{K}_{0.4}\text{Fe}_2\text{As}_2$ . The pristine  $\text{Ba}_{0.6}\text{K}_{0.4}\text{Fe}_2\text{As}_2$  has a smaller weak-collective pinning contribution than  $\text{Ba}(\text{Fe}_{0.93}\text{Co}_{0.07})_2\text{As}_2$ . As a result, the  $T$  dependence of  $S$  has no plateau  $H \leq 20$  kOe and is nonmonotonic, as well as  $H$  dependence of  $S$  is. The weak-collective-pinning character is recovered by an introduction of point defects with 3-MeV proton ( $\text{H}^+$ ) irradiation. These pinning sites enhance self-field  $J$  at 2 K from  $2.4 \times 10^6$  A/cm<sup>2</sup> in pristine sample to  $1.1 \times 10^7$  A/cm<sup>2</sup> in  $\text{H}^+$ -irradiated sample, which is the highest value reported ever in IBSs. The vortex creep rate is considerably slowed down by  $\text{H}^+$  irradiation, which originates from the enhanced weak-collective-pinning contribution.

## Chapter 7

# Vortex pinning and dynamics in heavy-ion irradiated

## $\text{Ba}(\text{Fe}_{1-x}\text{Co}_x)_2\text{As}_2$

### 7.1 Introduction

In stark contrast to the proton irradiation as described in chapter 6, energetic heavy-ion irradiation creates columnar defects (CDs) correlated along the direction of irradiation particles. In cuprates, almost ideal CDs, which are parallel to each other, are confirmed by transmission electron microscopy (TEM) observation. It is interesting to know whether CDs can be introduced in IBSs. This is firstly examined in 200-MeV Au irradiated  $\text{Ba}(\text{Fe}_{0.93}\text{Co}_{0.07})_2\text{As}_2$  by TEM observation [129], where almost parallel CDs are introduced, although they are not continuous. A similar result is obtained in 1.4 GeV Pb irradiated  $\text{Ba}_{0.6}\text{K}_{0.4}\text{Fe}_2\text{As}_2$  [102]. In general, the most effective pinning centers for vortices are CDs. In fact, significant enlargements of  $J_c$  are observed in  $\text{YBa}_2\text{Cu}_3\text{O}_7$ , *e.g.*, ten-fold increase in maximum was observed at low temperatures in Pb-irradiated sample. In IBSs, the irradiation are mainly performed in Co-doped and K-doped  $\text{BaFe}_2\text{As}_2$  crystals. The maximum enhancement is realized in 200-MeV irradiated  $\text{Ba}(\text{Fe}_{1-x}\text{Co}_x)_2\text{As}_2$  by a factor of 5 [129, 127]. It is interesting to know what kind of vortex state is realized with such strong and dense pinning potentials. In particular, the intriguing vortex phase "Bose glass" state is expected under the landscape of CD-pinning sites. We investigate the

vortex state in the heavy-ion irradiated system, especially in terms of the Bose glass phase. In order to investigate the dose dependence and irradiation-particle-energy dependence, we study the vortex pinning and dynamics in the mostly studied system of Co-doped  $\text{BaFe}_2\text{As}_2$  single crystals.

## 7.2 Screening current density and vortex dynamics under $H||\text{CDs}$

In the cuprates, characteristic behaviors have been observed under  $H||\text{CDs}$  in the Bose glass phase. One of them is the abrupt drop in the temperature dependence of the screening current  $J(T)$ , which is more clearly seen as a peak structure in  $-dJ(T)/dT$ . Another one is the peak structure in the temperature dependence of the normalized relaxation rate  $S(T)$ . Since both of them are originated from the variable range hopping, the characteristic temperature of the peak position in  $-dJ(T)/dT$  and  $S(T)$  are the same. Here we examine the possibility of the realization of Bose glass by means of the screening current density and vortex dynamics under  $H||\text{CDs}$ .

### 7.2.1 200-MeV Au irradiation

First we begin with relatively low energy irradiation of 200 MeV of gold (Au). We have already reported the 200 MeV Au irradiation in  $\text{Ba}(\text{Fe}_{0.93}\text{Co}_{0.07})_2\text{As}_2$  with a matching field of  $B_\phi = 20$  kG in Ref. [129]. Here detailed analyses are performed in the sample with  $B_\phi = 10$  kG, and later we compare with 2-GeV Au-irradiated sample with the same matching field. The screening current densities  $J_s$  are calculated by Bean model using the magnetization loops. The field dependence of  $J_s$  are depicted in Fig. 7.1.  $J(H)$  at  $T = 2$  K in unirradiated sample is also shown by the open symbol. We can see almost three times enhancement of the self-field  $J$  at  $T = 2$  K. Although this factor is smaller than that in  $B_\phi = 20$  kG, where 5-fold enhancement is observed, the significant enhancement manifests the strong pinning effects of CDs also in this matching field of  $B_\phi = 10$  kG. The normalized relaxation rate  $S$  at  $T = 5$  K and the field from 0 to 30 kOe are plotted in Fig. 7.2. The results in unirradiated sample and the sample with  $B_\phi = 20$  kG (Ref. [129]) are also shown. The value of  $S$  is systematically decreased with increasing the matching field. To extract the temperature dependence, we plot the  $J(T)$  and  $S(T)$  at some selected fields in Fig. 7.3 and Fig. 7.4, respectively. At any fields up to twice of

$B_\phi$ ,  $J(T)$  and  $S(T)$  monotonically change.

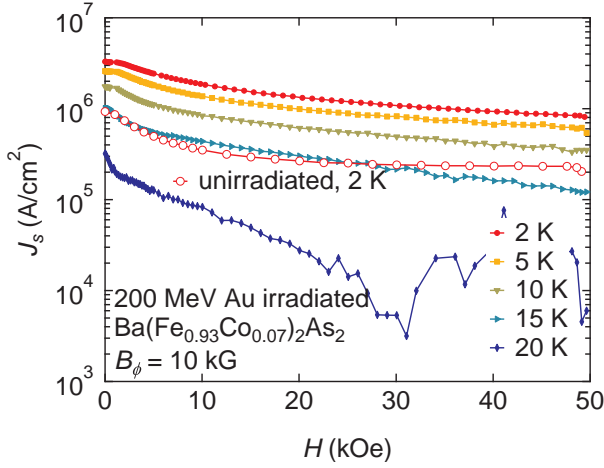


Figure 7.1: Field dependence of screening current  $J_s$  at several temperatures in 200-MeV Au-irradiated  $\text{Ba}(\text{Fe}_{0.93}\text{Co}_{0.07})_2\text{As}_2$ .

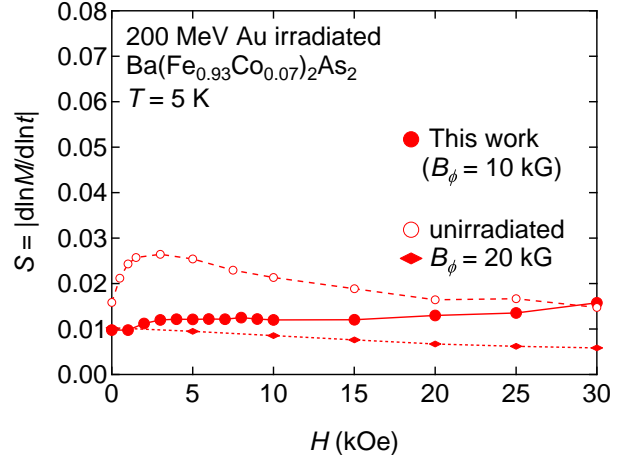


Figure 7.2: Field dependence of the normalized relaxation rate  $S$  at  $T = 5$  K and  $0 \leq H \leq 30$  kOe in 200-MeV Au-irradiated  $\text{Ba}(\text{Fe}_{0.93}\text{Co}_{0.07})_2\text{As}_2$  with  $B_\phi = 0$  (unirradiated), 10, and 20 kG.

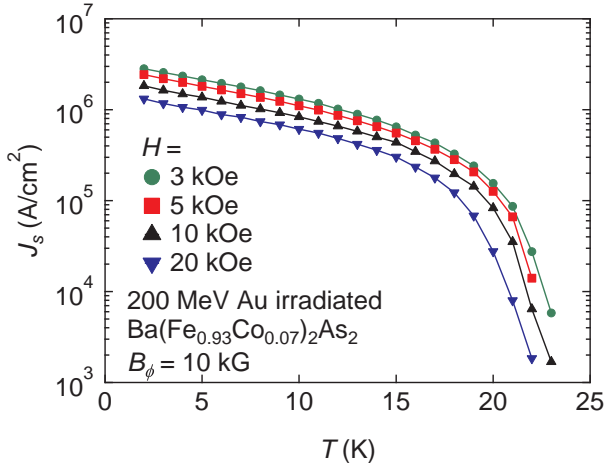


Figure 7.3: Temperature dependence of screening current  $J_s$  at several  $H = 2, 4, 10$ , and  $15$  kOe in 200-MeV Au irradiated  $\text{Ba}(\text{Fe}_{0.93}\text{Co}_{0.07})_2\text{As}_2$ .

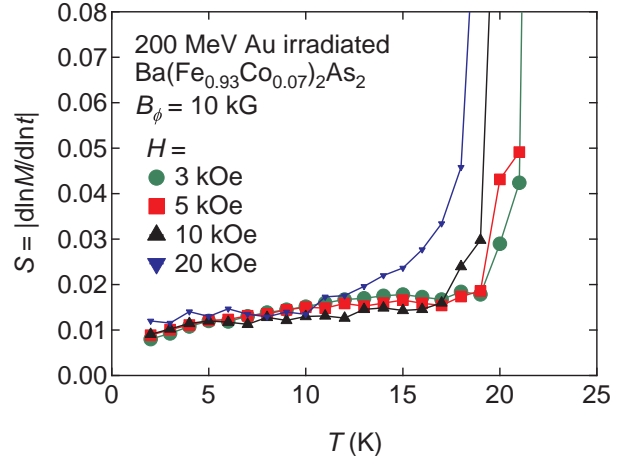


Figure 7.4: Temperature dependence of the normalized relaxation rate  $S$  at  $H = 0, 2, 4$ , and  $10$  kOe in 200-MeV Au irradiated  $\text{Ba}(\text{Fe}_{0.93}\text{Co}_{0.07})_2\text{As}_2$ .

### 7.2.2 2-GeV Au irradiation

The same physical values of  $J$  and  $S$  are compared also in the case of 2-GeV Au irradiation. Figure 7.5 and 7.6 are the field dependence of  $J$  and  $S$  at some selected temperatures, respectively. Although the enhancement in  $J$  are small, the general trend is similar to what observed

in 200-MeV irradiation. The different enhancement factor in  $J$  (5 times in 200-MeV irradiation and 2 times in 2-GeV irradiation) at low doses is explained as follows. According to the study on the damage structure introduced by heavy-ions in  $\text{Bi}_2\text{Sr}_2\text{CaCu}_2\text{O}_{8+y}$ , the defects are found to be parallel to each other at high energies and become splayed at lower ion energies by the sample stopping power [91]. Splayed structure is more effective to suppress the motion of vortices than only parallel structure since magnetic relaxation via half loop excitation [21] becomes slower by forced entanglement of vortices, resulting in enhancement of  $J_c$ . This is confirmed in cuprates superconductors by deliberate [153] or accidental splaying [154]. Now for Xe and Au irradiation in Co-doped  $\text{BaFe}_2\text{As}_2$ , splayed structure is expected to be introduced accidentally due to nuclear collision event as the heavy-ion energy is lowered. Besides, it is natural to assume that low energy irradiation should produce splayed structure frequently. As a consequence, an advantage of large enhancement of  $J_c$  in low-energy irradiation is due to accidental splayed structure, which disturbs magnetic relaxation in the same way. The temperature dependencies of  $J$  and  $S$  in 2-GeV irradiated sample are shown in Fig. 7.7 and 7.8. Here no anomaly is detected both in  $J(T)$  and  $S(T)$  at least around  $T_c/2$ . These are also the case in 200-MeV irradiation.

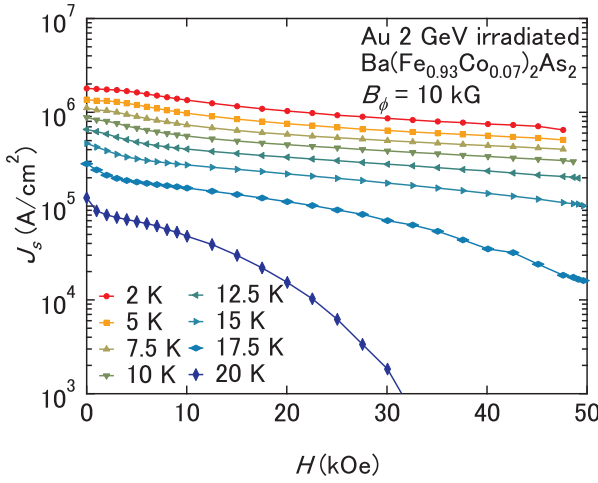


Figure 7.5: Field dependence of screening current  $J_s$  at several temperatures in 2-GeV Au irradiated  $\text{Ba}(\text{Fe}_{0.93}\text{Co}_{0.07})_2\text{As}_2$ .

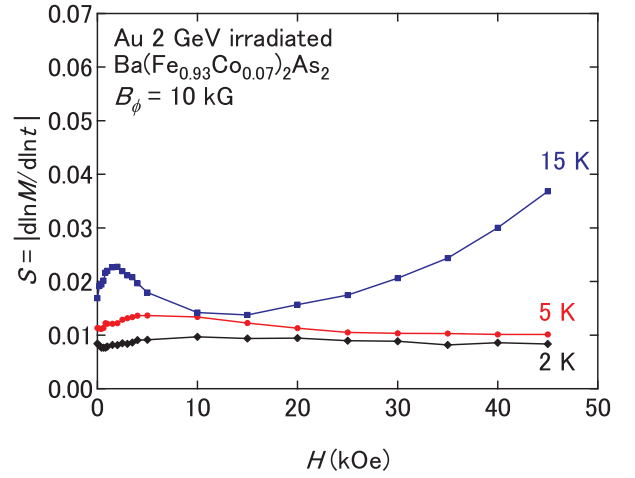


Figure 7.6: Field dependence of the normalized relaxation rate  $S$  at  $T = 2, 5$ , and  $15$  Ks in 2-GeV Au irradiated  $\text{Ba}(\text{Fe}_{0.93}\text{Co}_{0.07})_2\text{As}_2$ .

### 7.2.3 Discussion

In all the case above,  $J(T)$  and  $S(T)$  monotonically change, namely the abrupt drop in  $J(T)$  and the acceleration in  $S(T)$  are absent. This is quite contrast to the case in cuprates with CDs,

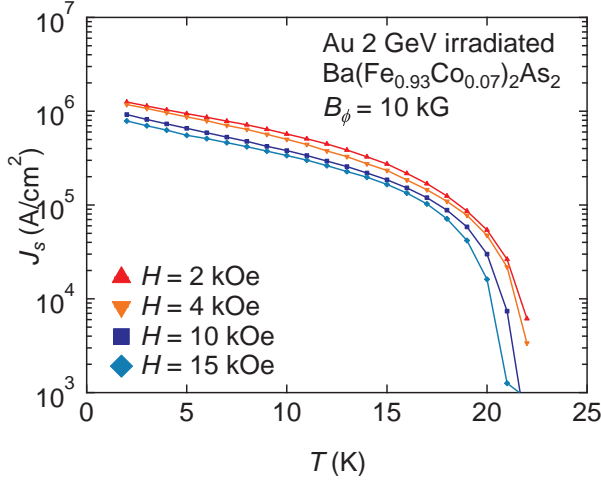


Figure 7.7: Temperature dependence of screening current  $J_s$  at several  $H = 2, 4, 10$ , and  $15$  kOe in 2-GeV Au irradiated  $\text{Ba}(\text{Fe}_{0.93}\text{Co}_{0.07})_2\text{As}_2$ .

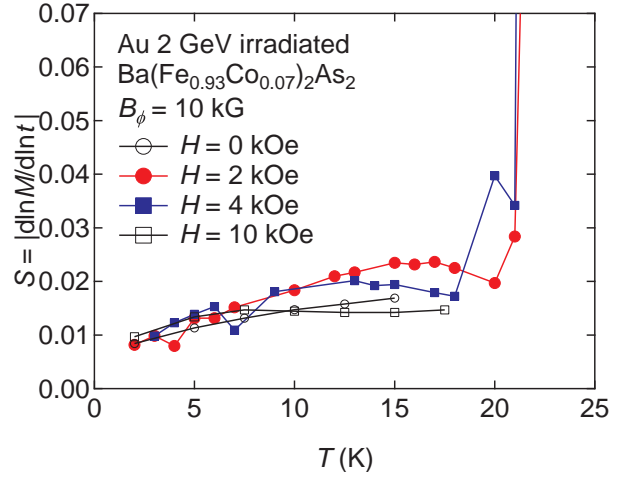


Figure 7.8: Temperature dependence of the normalized relaxation rate  $S$  at  $H = 0, 2, 4$ , and  $10$  kOe in 2-GeV Au irradiated  $\text{Ba}(\text{Fe}_{0.93}\text{Co}_{0.07})_2\text{As}_2$ .

where the characteristic structures are observed at  $T \simeq T_c/2$  [126]. The drop in  $J(T)$  and the acceleration of  $S(T)$  are attributed to the variable range hopping of vortices in the Bose glass phase. The absence of such behaviors in IBSs are naively thought that the Bose glass state is not realized in IBSs. However we cannot conclude the absence of them in the vicinity of  $T_c$ , since the precise determination of  $J$  and  $S$  is difficult due to the small absolute value of the magnetization signal. Besides, the theoretically predicted temperature to show such behaviors is very close to  $T_c$ , although it contradicts with the observation in cuprates. This inconsistency is not solved in the study of cuprates. If the vortex state in cuprates has some special characters and is normal in IBSs, the absence of the anomaly in  $J(T)$  and  $S(T)$  is not the good test for the presence of the Bose glass phase. If this is true, we have to examine the presence of the Bose glass phase in another way. In next section, we will approach another fingerprint of the Bose glass "lock-in" transition by means of the angular dependence of the magnetization.

### 7.3 Lock-in phenomena in $\text{Ba}(\text{Fe}_{0.93}\text{Co}_{0.07})_2\text{As}_2$

Vortex matter in high-temperature superconductors shows interesting phenomena in the presence of correlated defects, such as planar or columnar defects (CDs). Since vortices have a one-dimensional structure, these defects work as strong pinning centers when they trap vortices within the planes or columns. As a result, the critical current density ( $J_c$ ) exhibits a maximum when the applied magnetic field ( $\mathbf{H}$ ) is parallel to CDs. This directional pinning has been confirmed in heavy-ion irradiated  $\text{YBa}_2\text{Cu}_3\text{O}_7$  (YBCO) single crystals [155, 126] as well as in YBCO thin films with non-superconducting second phase additions that self-assemble into approximately aligned nanorods [156, 157, 158, 159]. This behavior has also been observed in the more recently discovered iron-based superconductors (IBSs), a clear indication that correlated defects can grow naturally and produce correlated pinning in these materials [160].

The response to tilt of the pinning by CDs depends on the electronic mass anisotropy ( $\varepsilon$ ) of the superconductor ( $\varepsilon^2 = m_{ab}/M_c$ , where  $m_{ab}$  and  $M_c$  denote effective electron masses in the  $ab$ -plane and along the  $c$ -axis), thus the angular dependence of correlated pinning is different in YBCO ( $\varepsilon \sim 1/5 - 1/7$ ) and  $\text{Bi}_2\text{Sr}_2\text{CaCu}_2\text{O}_{8+y}$  (Bi-2212,  $\varepsilon \sim 1/100$ ). The IBSs have a layered crystalline structure similar to the cuprates, with FeAs conducting layers instead of  $\text{CuO}_2$  layers, also leading to anisotropic behavior. But, in addition, IBSs are multi-band systems [32, 161, 162], allowing the possibility that the coherence length anisotropy ( $\varepsilon_\xi$ ) and the penetration depth anisotropy ( $\varepsilon_\lambda$ ) are different from each other and temperature dependent, as in the case of  $\text{MgB}_2$  [163, 164, 165]. These two anisotropy parameters influence the pinning of vortices in a nontrivial way. A recent numerical study shows that different angular dependences of  $J_c$  may be obtained by changing  $\varepsilon_\xi$  and  $\varepsilon_\lambda$ , even in the case of spherical pinning sites [166]. For the particular case of the IBSs of the  $\text{BaFe}_2\text{As}_2$  family (so-called "122"),  $\varepsilon_\xi$  estimated from  $H_{c2}$  is  $\sim 2$  near  $T_c$  and almost unity in the low temperature limit [8, 167, 168]. In addition, single crystals of 122 superconductors with optimal doping are free from twin boundaries, in contrast to YBCO, so that the effect of CDs can be purely investigated. Consequently, IBSs system must be an ideal platform to unveil the interaction of vortices and correlated pinning centers in multi-band high-temperature superconductors.

### 7.3.1 The orientation of irreversible magnetization

To investigate the vortex pinning properties we need to isolate the irreversible components from  $M_l$  and  $M_t$ , which are related to  $J_c$  through the critical state model. Figure 7.9(a) shows an example of isothermal hysteresis loops  $M_l(H)$  and  $M_t(H)$  at  $T = 5$  K,  $\theta = 45^\circ$ . To extract the irreversible longitudinal component  $M_{l,\text{irr}} \equiv \Delta M_l/2$ , we calculate  $\Delta M_l = M_{l,\text{up}} - M_{l,\text{down}}$ , where  $M_{l,\text{up}}$  and  $M_{l,\text{down}}$  are the magnetization for field sweeping up and down, respectively, and analogously for  $M_{t,\text{irr}} \equiv \Delta M_t/2$ . At this angle  $\theta = 45^\circ$  the amplitude of  $\Delta M_l$  and  $\Delta M_t$  are almost the same, which indicates that the irreversible magnetization vector  $\mathbf{M}_{\text{irr}}$  approximately points parallel to  $\tilde{n}$ . This is always the case in plate-like superconductors due to the large aspect ratio, and holds for all orientations except a narrow angular range  $\sim t/w$  around  $\mathbf{H} \parallel ab$  [27] ( $\sim 3^\circ$  in our case). We have measured these  $M_l(H)$  and  $M_t(H)$  loops for many orientations. Shown in Fig. 7.9(b) is the angle ( $\alpha$ ) between  $\mathbf{M}_{\text{irr}}$  and  $\tilde{n}$ , estimated as  $\alpha = \theta - \arctan(\Delta M_t/\Delta M_l)$ , confirming that  $\alpha \sim 0$  over most orientations as expected. Also included in the figure is the fit to  $\alpha(\theta)$  according to Ref. [27], showing good agreement. To understand the vortex states at temperatures where the pinning by CDs is strong and dominant, hereafter we focus on  $\mathbf{M}_{\text{irr}}$  at  $T = 5$  K, well below the depinning temperature ( $T < T_{\text{dp}}$ ) [75, 76].

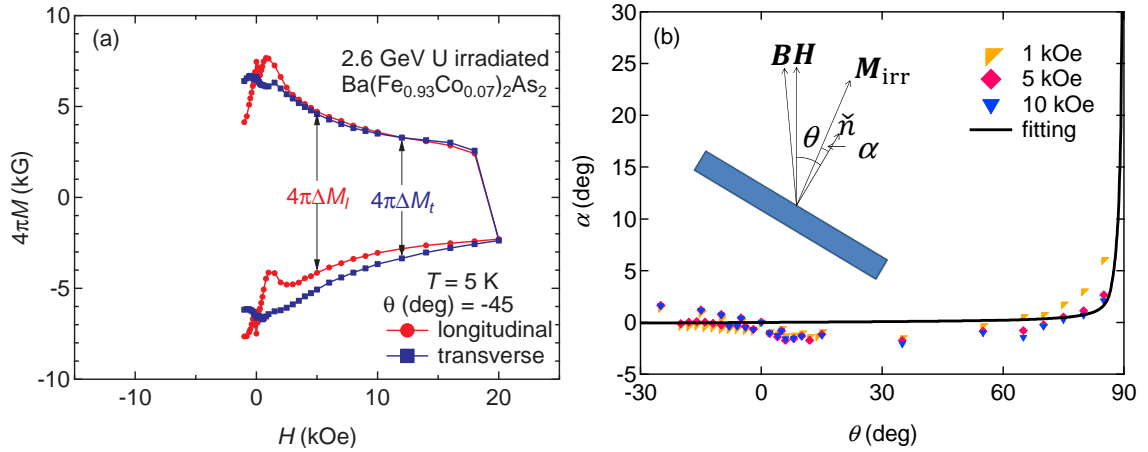


Figure 7.9: (a) Longitudinal and transverse magnetization curves  $4\pi M_l$  and  $4\pi M_t$  at 5 K,  $\theta = 45^\circ$ . (b)  $\theta$  dependence of  $\alpha$  between irreversible magnetization vector  $\mathbf{M}_{\text{irr}}$  and the sample normal  $\tilde{n}$ . Solid line indicates the fit to  $\alpha(\theta)$  according to Ref. [27]. Inset: definition of angles of  $\theta$  and  $\alpha$ .



### 7.3.2 The modulus of irreversible magnetization

Figures 7.10(a) and 7.10(b) show field dependences of  $4\pi M_{l,\text{irr}}$  and  $4\pi M_{t,\text{irr}}$ , respectively. For clarity, only a few of the measured  $\theta$  are included. For both components, the curves for positive and negative  $\theta$  almost coincide, indicating good reproducibility and an accurate determination of  $\theta$ . Figure 7.10(c) shows the modulus  $4\pi M_{\text{irr}} = 4\pi \sqrt{M_{l,\text{irr}}^2 + M_{t,\text{irr}}^2}$ . We can observe dip structures at low fields when  $\mathbf{H}$  is almost parallel to  $\tilde{n}$ , as we reported in Ref. [169, 127]. At  $\theta = 0^\circ$ , this structure extends up to  $H \simeq 3$  kOe, where  $4\pi M_{\text{irr}}$  reaches the maximum. As  $\theta$  increases this characteristic field shifts to lower field, and we cannot observe the dip structure for  $\theta > 35^\circ$ . As we discussed in Ref. [127], this dip structure is caused by the curvature of vortices below the self-field. Namely, the strongly curved magnetic field lines in the sample cannot be effectively pinned by straight CDs at fields lower than the self field, leading to the lower  $J_c$  around  $H = 0$ .

### 7.3.3 Lock-in transition

It is remarkable that  $4\pi M_{\text{irr}}$  at low fields is insensitive to the angle  $\theta$  for orientation close to  $\mathbf{H}||c$ , as we can see in Fig. 7.10(c). This behavior is attributed to the lock-in phenomenon originated from CDs as often observed in YBCO or BSCCO [77, 78, 170, 79, 171, 81, 172], that is, vortices are trapped in their full length by the CDs even when  $\mathbf{H}$  is tilted away from the track direction. This is the central finding of this study.

To explore this feature in detail, in Fig. 7.11(a) we plot the angular dependence of  $4\pi M_{\text{irr}}$  at all measured fields and orientations. We have collected data over a wide angular range ( $\sim 160^\circ$ ) to check that  $M_{\text{irr}}(\theta)$  is symmetric around both  $\mathbf{H}||c$  and  $\mathbf{H}||ab$ , as expected for a single crystal with CDs in the  $c$  axis and indeed observed. For all  $H$  up to the matching field  $M_{\text{irr}}(\theta)$  is maximum for  $\mathbf{H}||c$  and minimum for  $\mathbf{H}||ab$ . At high fields the peak at  $\theta = 0^\circ$  ( $\mathbf{H}||\tilde{n}||\text{CDs}$ ) is cusp-like, but as  $H$  decreases the  $c$ -axis peak becomes broader. Below  $H \simeq 9$  kOe a plateau around  $\theta = 0^\circ$  develops and the plateau width increases as  $H$  decreases, as observed in the blow-up of Fig. 7.11(b). The crossover from the plateau to the angular dependent  $M_{\text{irr}}(\theta)$  signals the transition from the Bose-glass phase (locked-in vortices) to the staircase vortices regime. This transition is rather sharp indicating a fast proliferation of vortex kinks, which in the "transverse Meissner effect" analogy [75] can be visualized as a fast penetration of a large number of weakly

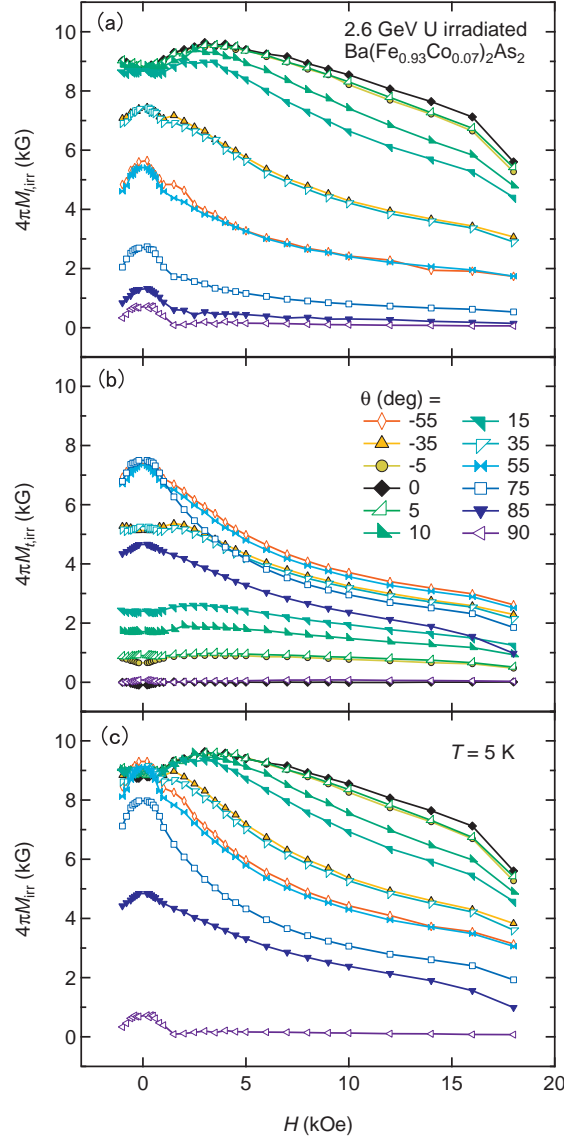


Figure 7.10: Field dependence of (a)  $4\pi M_{l,irr}$ , (b)  $4\pi M_{t,irr}$ , and (c)  $4\pi M_{irr}$  at each angle.

pinned vortices above the "transverse lower critical field."

The quantitative interpretation of these curves in terms of the physically relevant variable  $J_c(H, \theta)$  must be done with care. For  $\mathbf{H} \parallel \mathbf{c} \parallel \hat{n}$ , the Bean critical state model provides the relation  $J_c = 40M_{irr}/[w(1 - w/3l)]$ , and for our almost square crystal this can be simplified to  $J_c = 60M_{irr}/w$ . For  $\theta \neq 0^\circ$  two complications arise. First, the orientation of the vortices, i.e., the angle  $\theta_B$  between the internal field  $\mathbf{B}$  (the vortex direction) and the  $c$ -axis is different from  $\theta$ . This is clearly the case in the lock-in regime, the focus of the present study, as  $\theta_B = 0$  as long as  $\theta < \theta_L$ . But  $\theta_B \neq \theta$  also occurs outside the lock-in phase for staircase vortices [79], and even in the absence of CDs due to anisotropy and geometrical effects [21]. So, the critical state is

determined by  $J_c(\theta_B)$  rather than  $J_c(\theta)$ . This is a low field phenomenon; for large enough  $H$  the free energy cost of a  $\mathbf{B}$  vs.  $\mathbf{H}$  misalignment dominates and  $\theta_B \rightarrow \theta$ .

The second complication is that the current flowing parallel to the sides of the crystal that are perpendicular to the rotation axis are not perpendicular to the vortices (non-maximum Lorentz force configuration), so the effective  $J_c$  in those sides is approximately  $J_c/\cos(\theta_B)$ . We must thus use an anisotropic sand-pile Bean model, which gives  $J_c(\theta_B) = 40M_{\text{irr}}/[w(1 - \cos(\theta_B)/3)]$ . This expression is a good approximation under the same conditions as the  $\mathbf{M}_{\text{irr}}||\tilde{n}$  approximation is, i.e., everywhere except a narrow angular range  $\sim t/w$  around  $\mathbf{H}||ab$  [27]. So it is valid for most of our data according to Fig. 7.9(b). At high fields (e.g. 20 and 40 kOe),  $\theta_B \approx \theta$  and  $J_c(\theta) = 40M_{\text{irr}}/[w(1 - \cos(\theta)/3)]$ , thus the monotonic decrease of  $M_{\text{irr}}$  toward  $\theta = 90^\circ$  confirms that the directional pinning of the CDs dominates in almost the whole range of angles producing staircase vortices. In the lock-in plateau  $\theta_B = 0$  and the simple relation  $J_c = 60M_{\text{irr}}/w$  holds. It must also be noted that  $J_c$  (and thus  $M_{\text{irr}}$ ) should not be strictly constant in the lock-in regime due to the progressive increase of the free energy cost of the misalignment between  $\mathbf{B}$  and  $\mathbf{H}$ , reflected in the term  $\propto -\mathbf{B} \cdot \mathbf{H} \sim -BH \cos \theta$ . However, in the lock-in regime both  $H$  and  $\theta(< \theta_L)$  are small, so the *variations* of this term are small and in practice an almost angular-independent  $J_c$  is observed.

Another possibility for the angular-independent  $M_{\text{irr}}$  that must be considered is the self-field effect. The vortex configuration in a superconductor is determined by the applied field  $\mathbf{H}$  and the self-field ( $\mathbf{H}_{\text{sf}}$ ) generated by the shielding currents. In a plate-like crystal these currents are constrained to be mainly parallel to the  $ab$  planes even for  $\theta \neq 0^\circ$ , producing a non-uniform  $H_{\text{sf}}$  qualitatively similar to that of a dipole parallel to  $\tilde{n}$  and of average intensity  $H_{\text{sf}} \sim J_c t/2$ . For  $H \ll H_{\text{sf}}$  the irreversible magnetization is dominated by this "remnant magnetization" that is independent of  $\theta$ . In particular,  $M_{\text{irr}}$  for  $H = 0$  should be constant over a very broad angular range as we indeed observe [see Fig. 7.10(c)]. Clearly this effect is always present in high aspect ratio samples, so it is difficult to separate it from the lock-in phenomenon. However, several features indicate that the self-field is not the main cause of the plateau in our crystal. First, for  $T = 5$  K and  $\theta = 0^\circ$  our crystal has a self-field  $J_c = 2$  MA/cm<sup>2</sup>, so  $H_{\text{sf}} \sim 1.6$  kOe, but we observe the plateau up to much higher fields ( $\sim 9$  kOe). Second, the crossover from the plateau to the angular dependent  $M_{\text{irr}}$  due to the self-field should be smooth; in contrast we observe sharp drops in  $M_{\text{irr}}(\theta)$  at the ends of the plateaus, consistent with the sudden appearance of

staircase vortices with weakly pinned kinks.

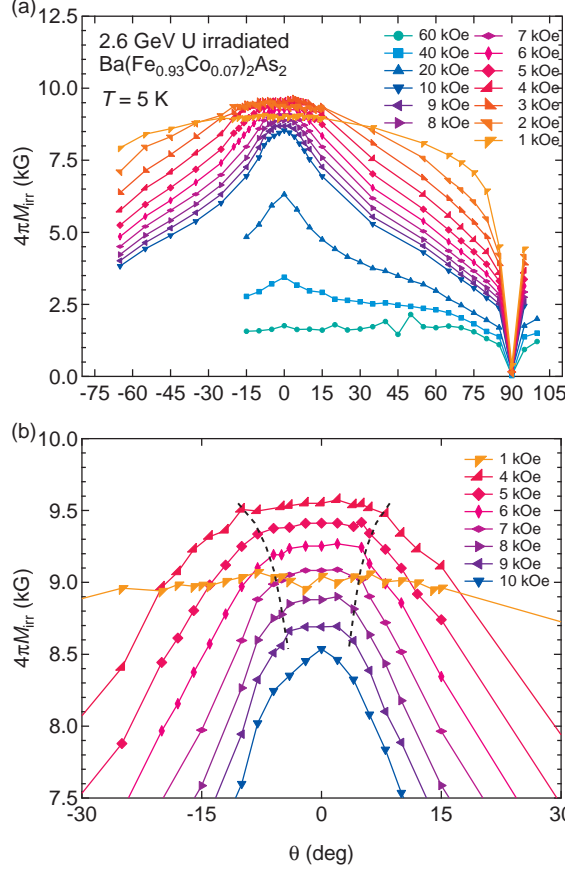


Figure 7.11: (a)  $\theta$  dependence of  $4\pi M_{\text{irr}}$  at each field. All points are taken from Fig. 7.10(c). (b) Blow-up of (a) around  $\theta = 0^\circ$  at selected field. Broken lines are guides to the eye for the lock-in transition.

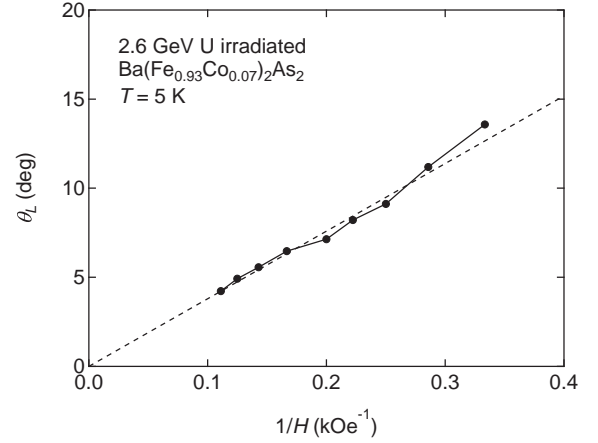


Figure 7.12: Inverse-field dependence of lock-in angle  $\theta_L$ , defined by a half of the width of the plateau in Fig. 7.11. Broken line is the linear fit according to Eq. (7.1).

A third, strong evidence comes from the field dependence of the plateau width, which in the lock-in scenario should be  $2\theta_L$ , with

$$\theta_L = \frac{4\pi\sqrt{2\varepsilon_l\varepsilon_r}}{\phi_0 H} \propto 1/H, \quad (7.1)$$

where  $\varepsilon_l$  is the vortex line tension and  $\varepsilon_r$  is the effective pinning energy per unit length [76, 21]. Figure 7.12 shows inverse-field dependence of  $\theta_L$ , which is defined as a half width of the plateau in Fig. 7.11. The linear variation of  $\theta_L$  as a function of  $1/H$  clearly demonstrates that these plateaus result from the lock-in phenomenon.

It is noteworthy that the linear fit for  $\theta_L(H^{-1})$  extrapolates to the origin, as expected from Eq. (7.1). This is in contrast to previous results for 309 MeV Au irradiated  $\text{ErBa}_2\text{Cu}_3\text{O}_{7-\delta}$ ,

where a positive nonzero extrapolation was observed [26] and attributed in part to natural splay of the CDs in the case of irradiation with lower-energy ions. In this context, the CDs introduced by 2.6 GeV U ions in the present crystal are more ideally parallel to each other.

Finally, we comment on the numerical factor of the slope in Fig. 7.12. Since we measured at low temperature, we set the pinning energy as  $\varepsilon_r = \varepsilon_0$  without temperature smearing factor, and the line tension simplified as  $\varepsilon_l = [\varepsilon^2 \varepsilon_0 \varepsilon(\theta)] \ln \kappa \approx \varepsilon_0 \ln \kappa$ , where the Ginzburg-Landau parameter  $\kappa = \lambda_{ab}/\xi_{ab}$  is estimated from the in-plane penetration depth  $\lambda_{ab}$  and in-plane coherence length  $\xi_{ab}$ . From the upper critical field  $H_{c2}^c = 280$  kOe,  $\xi_{ab} = 3.4$  nm can be obtained [34]. With the experimental value of the slope  $\simeq 660$  G rad, we are able to solve the value of  $\lambda_{ab}$  as  $\simeq 79$  nm. This is far from the accepted value of  $\lambda_{ab} \simeq 200$  nm. Such numerical discrepancy is also found in cuprates [77, 79, 26], regardless of the CD or twin boundary pinning. For example, in Ref. [26]  $\lambda_{ab} \approx 50$  nm is assumed to reproduce the observed lock-in angle, instead of the accepted value of  $\lambda_{ab} \simeq 140$  nm. It is always the case that the lock-in angle is larger than the predicted one both in cuprates and in IBSs. A similar difference is found also in the trapping angle of IBS film [173]. Further studies are required to solve this general quantitative discrepancy.

### 7.3.4 Conclusion

We have observed the lock-in phenomenon of vortices to parallel CDs in a high-quality single crystal of  $\text{Ba}(\text{Fe}_{0.93}\text{Co}_{0.07})_2\text{As}_2$  without twin boundaries irradiated with 2.6 GeV uranium ions. The lock-in regime is identified by a plateau in the angular dependence of the irreversible component of the magnetization. The width of the plateau is proportional to  $1/H$  as expected for the characteristic lock-in angle  $\theta_L$ .

## Chapter 8

# Summary and Conclusions

A summary of the important results of this thesis is presented in this concluding chapter. In this study, we have developed a system to perform *in situ* resistivity measurements during the particle irradiation to investigate the pair-breaking effect. The concomitantly irradiated samples are arranged to study the vortex pinning from point defects. We have grown single crystals of Co-doped and K-doped  $\text{BaFe}_2\text{As}_2$  systems for these studies. We have measured the magnetization in a wide range of temperature and field in the pristine and irradiated samples. In the case of U-irradiated sample, we also investigated the angular dependence of vortex pinning.

In the following, we summarize the results and give concluding remarks.

### Pair-breaking effect in $\text{Ba}_{1-x}\text{K}_x\text{Fe}_2\text{As}_2$

In chapter 5, the robustness of the superconducting transition temperature  $T_c$  for impurity scattering is clearly demonstrated. To take an advantage of successive introduction of point defects in a given sample, we utilized the proton irradiation at low temperatures, rather than chemical substitutions. By using K-doped  $\text{BaFe}_2\text{As}_2$  system, the residual resistivity  $\rho(T = 0)$  in the as-grown sample can be neglected, which allows us a straightforward transformation of impurity scattering rate from resistivity. The suppression rates of  $T_c$  are consistent with that in chemically substituted samples or proton-irradiated  $\text{Ba}(\text{Fe}_{1-x}\text{Co}_x)_2\text{As}_2$  system, and quantitatively discussed with the help of the normalized scattering rate. We finally conclude that the observed small suppression rates cannot be explained by  $s_{\pm}$ -wave state with a sign reversal of the superconducting order parameter between hole and electron FSs.

We can conclude the pairing state with taking other experimental results into account. In

the inelastic neutron scattering experiment, the peak structure in the imaginary part of the spin susceptibility was supposed to be attributable to the resonance peak, which is expected in the  $s_{\pm}$ -wave state. However, the following theoretical study shows that the observed broad peak is reproducible by assuming  $s_{++}$ -wave state. In scanning-tunneling microscopy, the quasiparticle interference under strong magnetic field was able to be interpreted by sign-reversal between hole and electron FSs, using the framework of cuprates (single band model). This interpretation cannot be justified in IBSs since the system is multi band, as suggested by Yamakawa *et al.*. Besides, the angle-resolved photoemission spectroscopy experiment shows the orbital independent gap magnitude, supporting the orbital-fluctuation mediated superconducting scenario. The  $s_{\pm}$ -wave state cannot consistently explain all the results, although the theoretical interpretation is still not clear. On the contrary, our study clearly demonstrates that the  $s_{\pm}$ -wave state is an inadequate assumption to explain the small suppression rate of  $T_c$  as introducing impurity scattering. This strongly supports the  $s_{++}$ -wave state, and gives the evidence of the orbital-fluctuation pairing mechanism.

These findings are greatly helpful to determine the superconducting pairing mechanism in iron-based superconductors. The inadequacy of  $s_{\pm}$ -wave state suggests that a novel pairing glue of the orbital fluctuations plays an important role in IBSs.

### **Weak-collective pinning and collective creep in iron-based superconductors**

In chapter 6, we have investigated the effects of weak-collective-pinning centers in proton irradiated systems. We compared Co-doped and K-doped  $\text{BaFe}_2\text{As}_2$ . The enhancement of the screening current density with proton irradiation is moderate by a factor of 2.5 at low temperatures under zero field. The vortex dynamics are illustrated by collective creep both in the pristine and the proton-irradiated Co-doped  $\text{BaFe}_2\text{As}_2$ . By contrast, 5-fold enlargement of the screening current density is observed in K-doped system in the same condition. Although the picture of collective creep is reasonable in proton-irradiated  $(\text{Ba,K})\text{Fe}_2\text{As}_2$ , it does not work well in the pristine sample. These differences in Co-doped and K-doped systems are originated from the intrinsic pinning of dopant atoms, namely Co atoms work as weak pinning centers, while K atoms do not. Another remarkable result is that the highest screening current density is realized in proton-irradiated  $(\text{Ba,K})\text{Fe}_2\text{As}_2$ , reaching of the order of  $10^7$  A/cm<sup>2</sup>.

The IBS system is a suitable candidate to understand the vortex states in high-temperature

superconductors. In stark contrast to conventional superconductors, the vortices in high-temperature superconductors are not supposed to be a straight line, and we cannot neglect the thermal fluctuation effect. Besides, the elasticity of vortex line lattice should be taken into account in high-temperature superconductors. As a result, the behaviors of vortices are described by the weak-collective pinning theory. Although this theory succeeds in explaining the properties in cuprate superconductors, it is not clear that the theory is appropriate in IBSs. In our study, we demonstrate the universality of vortex behaviors in cuprates and IBSs.

These findings contribute to understanding the role of weak-pinning centers in IBSs, which leads to the general understanding of weak-collective pinning and collective creep in high-temperature superconductors. These are also important in practical point of view when fabricating IBS wires and tapes with high performance.

### **Bose glass phase in iron-based superconductors with columnar defects**

In chapter 7, we have examined the possible realization of the Bose glass state in IBSs, which accompanies the novel feature of vortex pinning and dynamics in the system with CDs. Although the results under  $H||\text{CDs}$  are different from that in cuprates, we have not found the contradiction with theoretical predictions. As another approach to detect the fingerprint of the Bose glass state, we have identified the lock-in transition by means of angular dependence of the magnetization, which is quite similar to cuprates.

The Bose-glass phase is one of the most interesting vortex state, since many novel features, such as pronounced flux relaxation rate, are observed. The cuprates were only the case that the Bose-glass state was observed, but new high-temperature superconductors, IBSs, are another candidate to realize this phase. The identification of the Bose-glass phase testifies the similarity of the vortex states between cuprates and IBSs. However, the characteristic features of the Bose-glass phase under  $H||c$  have not reported in IBSs. In our study, we display the Bose-glass state feature for the first time in the angular dependent magnetization, and propose the similarities of the vortex states in high-temperature superconductors.

These findings will help to solve the contradiction between the theoretical and the experimental results in cuprates. The realistic description of the Bose glass state in the second class of high-temperature superconductors is beneficial for the understanding of ideal pinning.



# List of Publications

## Publications in journals

- [1] T. Taen, Y. Nakajima, T. Tamegai, and H. Kitamura, “Enhancement of critical current density and vortex activation energy in proton-irradiated Co-doped  $\text{BaFe}_2\text{As}_2$ ”, *Phys. Rev. B* **86**, 094527 (2012).
- [2] T. Taen, F. Ohtake, H. Akiyama, H. Inoue, Y. Sun, S. Pyon, T. Tamegai, and H. Kitamura, “Pair-breaking effects induced by 3-MeV proton irradiation in  $\text{Ba}_{1-x}\text{K}_x\text{Fe}_2\text{As}_2$ ”, *Phys. Rev. B* **88**, 224514 (2013).
- [3] T. Taen, H. Yagyuda, Y. Nakajima, T. Tamegai, O. Ayala-Valenzuela, L. Civale, B. Maiorov, T. Kambara, and Y. Kanai, “Observation of lock-in phenomena in heavy-ion-irradiated single crystal of  $\text{Ba}(\text{Fe}_{0.93}\text{Co}_{0.07})_2\text{As}_2$ ”, *Phys. Rev. B* **89**, 024508 (2014).
- [4] Y. Nakajima, T. Taen, and T. Tamegai, “Possible Superconductivity above 25 K in Single-Crystalline Co-Doped  $\text{BaFe}_2\text{As}_2$ ”, *J. Phys. Soc. Jpn.* **78**, 023702 (2009).
- [5] Y. Nakajima, Y. Tsuchiya, T. Taen, T. Tamegai, S. Okayasu, and M. Sasase, “Enhancement of critical current density in Co-doped  $\text{BaFe}_2\text{As}_2$  with columnar defects introduced by heavy-ion irradiation”, *Phys. Rev. B* **80**, 012510 (2009).
- [6] Y. Nakajima, T. Taen, Y. Tsuchiya, T. Tamegai, H. Kitamura, and T. Murakami, “Suppression of the critical temperature of superconducting  $\text{Ba}(\text{Fe}_{1-x}\text{Co}_x)_2\text{As}_2$  by point defects from proton irradiation”, *Phys. Rev. B* **82**, 220504 (2010).
- [7] T. Tamegai, T. Taen, H. Yagyuda, Y. Tsuchiya, S. Mohan, T. Taniguchi, Y. Nakajima, S. Okayasu, M. Sasase, H. Kitamura, T. Murakami, T. Kambara, and Y. Kanai, “Effects

of particle irradiations on vortex states in iron-based superconductors”, *Supercond. Sci. Technol.* **25**, 084008 (2012).

## Publications in conference proceedings

- [1] Y. Nakajima, Y. Tsuchiya, T. Taen, H. Yagyuda, T. Tamegai, S. Okayasu, M. Sasase, H. Kitamura, T. Murakami, “Critical current densities and flux creep rate in Co-doped  $\text{BaFe}_2\text{As}_2$  with columnar defects introduced by heavy-Ion irradiation”, *Physica C* **470**, 1103 (2010).
- [2] T. Tamegai, Y. Tsuchiya, T. Taen, Y. Nakajima, S. Okayasu, M. Sasase, “Effects of heavy-ion irradiation on the vortex state in  $\text{Ba}(\text{Fe}_{1-x}\text{Co}_x)_2\text{As}_2$ ”, *Physica C* **470**, S360 (2010).
- [3] T. Taen, Y. Nakajima, T. Tamegai, H. Kitamura, T. Murakami, “Vortex dynamics in proton irradiated Co-doped  $\text{BaFe}_2\text{As}_2$ ”, *Physica C* **471**, 784 (2011).
- [4] T. Tamegai, T. Taen, H. Yagyuda, Y. Nakajima, S. Okayasu, M. Sasase, H. Kitamura, T. Murakami, T. Kambara, and Y. Kanai, “Low-field anomaly of vortex dynamics in iron-pnictide superconductors”, *Physica C* **471**, 777 (2011).
- [5] Y. Nakajima, Y. Tsuchiya, T. Taen, T. Tamegai, H. Kitamura, T. Murakami, “ $\text{H}^+$  irradiation effect in Co-Doped  $\text{BaFe}_2\text{As}_2$  single crystals”, *Physica C* **471**, 647 (2011).
- [6] T. Tamegai, T. Taniguchi, T. Taen, Y. Nakajima, T. Nishizaki, T. Naito, N. Kobayashi, H. Kitamura T. Murakami, “Vortex phase diagram of pristine and irradiated Co-doped  $\text{BaFe}_2\text{As}_2$ ”, *J. Phys. Conf. Ser.* **400**, 022122 (2012).
- [7] T. Taen, H. Yagyuda, Y. Nakajima, T. Tamegai, S. Okayasu, H. Kitamura, T. Murakami, F. Laviano, and G. Ghigo, “Effects of irradiation-particle energy on critical current density in Co-doped  $\text{BaFe}_2\text{As}_2$ ”, *Physica C* **484**, 62 (2013).
- [8] T. Taen, T. Ohori, F. Ohtake, T. Tamegai, K. Kihou, S. Ishida, H. Eisaki, and H. Kitamura, “Critical current density and vortex dynamics in pristine and proton-irradiated  $(\text{Ba}, \text{K})\text{Fe}_2\text{As}_2$ ”, *Physica C* **494**, 106 (2013).

## Publications (others)

### journals

- [1] T. Taen, Y. Tsuchiya, Y. Nakajima, and T. Tamegai, “Superconductivity at  $T_c \sim 14$  K in single-crystalline  $\text{FeTe}_{0.61}\text{Se}_{0.39}$ ”, *Phys. Rev. B* **80**, 092502 (2009).
- [2] S. Mohan, T. Taen, H. Yagyuda, Y. Nakajima, T. Tamegai, T. Katase, H. Hiramatsu, H. Hosono, “Transport and magnetic properties of Co-doped  $\text{BaFe}_2\text{As}_2$  epitaxial thin films grown on MgO substrate”, *Supercond. Sci. Technol.* **23**, 105016 (2010).
- [3] Q. Ding, S. Mohan, Y. Tsuchiya, T. Taen, Y. Nakajima, T. Tamegai, “Low-temperature synthesis of  $\text{FeTe}_{0.5}\text{Se}_{0.5}$  polycrystals with a high transport critical current density”, *Supercond. Sci. Technol.* **24**, 075025 (2011).
- [4] Q. Ding, S. Mohan, T. Taen, Y. Tsuchiya, Y. Nakajima, T. Tamegai, “Magneto-optical imaging and transport properties of FeSe superconducting tapes prepared by diffusion method”, *Supercond. Sci. Technol.* **25**, 025003 (2012).
- [5] Q. Ding, Y. Tsuchiya, S. Mohan, T. Taen, Y. Nakajima, and T. Tamegai, “Magnetic and transport properties of iron-platinum arsenide  $\text{Ca}_{10}(\text{Pt}_{4-\delta}\text{As}_8)(\text{Fe}_{2-x}\text{Pt}_x\text{As}_2)_5$  single crystal”, *Phys. Rev. B* **85**, 104512 (2012).
- [6] Q. Ding, Y. Tsuchiya, Y. Sun, T. Taen, Y. Nakajima, T. Tamegai, “Anisotropies and homogeneities of superconducting properties in iron-platinum-arsenide  $\text{Ca}_{10}(\text{Pt}_3\text{As}_8)(\text{Fe}_{1.79}\text{Pt}_{0.21}\text{As}_2)_5$ ”, *J. Phys. Soc. Jpn.* **81**, 114723 (2012).
- [7] Y. Sun, T. Taen, Y. Tsuchiya, Z. X. Shi, T. Tamegai, “Annealing, acid, and alcoholic beverage effects on  $\text{Fe}_{1+y}\text{Te}_{0.6}\text{Se}_{0.4}$ ”, *Supercond. Sci. Technol.* **26**, 015015 (2013).
- [8] Y. Sun, T. Taen, Y. Tsuchiya, Q. P. Ding, S. Pyon, Z. X. Shi, T. Tamegai, “Large, homogeneous, and isotropic critical current density in oxygen annealed  $\text{Fe}_{1+y}\text{Te}_{0.6}\text{Se}_{0.4}$  single crystal” *Appl. Phys. Express* **6**, 043101 (2013).
- [9] Y. Sun, Y. Tsuchiya, T. Yamada, T. Taen, S. Pyon, Z. Shi, and T. Tamegai, “Evolution of superconductivity in  $\text{Fe}_{1+y}\text{Te}_{1-x}\text{Se}_x$  annealed in Te vapor”, *J. Phys. Soc. Jpn.* **82**, 093705 (2013).

- [10] Y. Sun, T. Taen, Y. Tsuchiya, S. Pyon, Z. Shi, and T. Tamegai, “Magnetic relaxation and collective vortex creep in FeTe<sub>0.6</sub>Se<sub>0.4</sub> single crystal”, *Europhys Lett.* **103**, 57013 (2013).
- [11] Y. Sun, Y. Tsuchiya, T. Yamada, T. Taen, S. Pyon, Z. Shi, and T. Tamegai, “Bulk superconductivity in Fe<sub>1+y</sub>Te<sub>1-x</sub>Se<sub>x</sub> induced by annealing in Se and S Vapor”, *J. Phys. Soc. Jpn.* **82**, 115002 (2013).
- [12] S. Pyon, T. Taen, F. Ohtake, Y. Tsuchiya, H. Inoue, H. Akiyama, H. Kajitani, N. Koizumi, S. Okayasu, and T. Tamegai, “Enhancement of critical current densities in (Ba,K)Fe<sub>2</sub>As<sub>2</sub> by 320 MeV Au irradiation in single crystals and by high-pressure sintering in PIT wires”, *Appl. Phys. Express* **6**, 123101 (2013).

## proceedings

- [1] T. Tamegai, T. Taen, Y. Tsuchiya, Y. Nakajima, S. Okayasu, M. Sasase, “Critical current densities and vortex dynamics in Ba(Fe<sub>1-x</sub>Co<sub>x</sub>)<sub>2</sub>As<sub>2</sub> single crystals”, *J. Supercond. Novel Mag.* **23**, 605 (2010).
- [2] T. Taen, Y. Tsuchiya, Y. Nakajima, T. Tamegai, “Critical current densities and vortex dynamics in FeTe<sub>x</sub>Se<sub>1-x</sub> single crystals”, *Physica C* **470**, 1106 (2010).
- [3] Y. Nakajima, T. Taen, T. Tamegai, “Doping dependence of magnetic and transport properties in single crystalline Co-doped BaFe<sub>2</sub>As<sub>2</sub>”, *Physica C* **470**, S408 (2010).
- [4] T. Taen, Y. Tsuchiya, Y. Nakajima, T. Tamegai, “Characterization of superconductivity in Fe(Te<sub>1-x</sub>Se<sub>x</sub>) single crystals with  $T_c \sim 14$  K”, *Physica C* **470**, S391 (2010).
- [5] Q. Ding, T. Taen, S. Mohan, Y. Nakajima, T. Tamegai, “Magneto-optical imaging of polycrystalline FeTe<sub>1-x</sub>Se<sub>x</sub> prepared at various conditions”, *Physica C* **471**, 651 (2011).
- [6] S. Mohan, T. Taen, H. Yagyuda, Y. Nakajima, T. Tamegai, T. Katase, H. Hiramatsu, H. Hosono, “Characterization of epitaxial Co-doped BaFe<sub>2</sub>As<sub>2</sub> thin films”, *Physica C* **471**, 1181 (2011).
- [7] Q. Ding, S. Mohan, T. Taen, Y. Tsuchiya, Y. Nakajima, T. Tamegai, “FeSe superconducting tapes with a high critical current density fabricated by diffusion method”, *J. Phys. Conf. Ser.* **400**, 022016 (2012).

- [8] T. Taen, Y. Nakajima, T. Tamegai, S. Okayasu, M. Sasase, “Effects of swift Xe irradiation in  $\text{Ba}(\text{Fe}_{1-x}\text{Co}_x)_2\text{As}_2$  single crystals”, J. Phys. Conf. Ser. **400**, 022119 (2012).
- [9] T. Tamegai, Q. P. Ding, H. Inoue, T. Taen, Y. Tsuchiya, S. Mohan, Y. Sun, T. Prombood, and Y. Nakajima, “Magneto-optical characterization of iron-based superconducting wires and tapes”, IEEE Trans. Appl. Supercond. **23**, 7300304 (2013).
- [10] F. Laviano, R. Gerbaldo, G. Ghigo, L. Gozzelino, T. Taen, Y. Nakajima, T. Tamegai, “Quantitative Magneto-optical imaging of supercurrents in heavy-ion irradiated cuprate and pnictide superconductors”, J. Supercond. Nov. Magn. **26**, 2063 (2013).
- [11] T. Tamegai, Q. P. Ding, T. Taen, F. Ohtake, H. Inoue, Y. Tsuchiya, S. Mohan, Y. Sun, Y. Nakajima, S. Pyon, H. Kitamura, “Superconducting properties of iron-platinum-arsenides  $\text{Ca}_{10}(\text{Pt}_n\text{As}_8)(\text{Fe}_{2-x}\text{Pt}_x\text{As}_2)_5$  ( $n = 3, 4$ )”, Physica C **494**, 69 (2013).
- [12] F. Laviano, R. Gerbaldo, G. Ghigo, L. Gozzelino, G. P. Mikitik, T. Taen, T. Tamegai, “Evidence of anisotropic vortex pinning by intrinsic and irradiation induced defects in  $\text{Ba}(\text{Fe},\text{Co})_2\text{As}_2$  studied by quantitative magneto-optical imaging”, to be published in Supercond. Sci. Technol.

# References

- [1] J. R. Thompson, Y. R. Sun, L. Civale, A. P. Malozemoff, M. W. McElfresh, A. D. Marwick, and F. Holtzberg, *Phys. Rev. B* **47** (1993) 14440.
- [2] J. Paglione and R. L. Greene, *Nat. Phys.* **6** (2010) 645.
- [3] C.-H. Lee, A. Iyo, H. Eisaki, H. Kito, M. T. Fernandez-Diaz, T. Ito, K. Kihou, H. Matsuhata, M. Braden, and K. Yamada, *J. Phys. Soc. Jpn.* **77** (2008) 083704.
- [4] W. Malaeb, T. Yoshida, T. Kataoka, A. Fujimori, M. Kubota, K. Ono, H. Usui, K. Kuroki, R. Arita, H. Aoki, Y. Kamihara, M. Hirano, and H. Hosono, *J. Phys. Soc. Jpn.* **77** (2008) 093714.
- [5] I. Mazin and J. Schmalian, *Physica C* **469** (2009) 614 .
- [6] A. Chubukov, *Annu. Rev. Condens. Matter Phys.* **3** (2012) 57.
- [7] S. Ishida, M. Nakajima, T. Liang, K. Kihou, C.-H. Lee, A. Iyo, H. Eisaki, T. Kakeshita, Y. Tomioka, T. Ito, and S.-i. Uchida, *J. Am. Chem. Soc.* **135** (2013) 3158.
- [8] H. Q. Yuan, J. Singleton, F. F. Balakirev, S. A. Baily, G. F. Chen, J. L. Luo, and N. L. Wang, *Nature* **457** (2009) 565.
- [9] K. Hashimoto, T. Shibauchi, S. Kasahara, K. Ikada, S. Tonegawa, T. Kato, R. Okazaki, C. J. van der Beek, M. Konczykowski, H. Takeya, K. Hirata, T. Terashima, and Y. Matsuda, *Phys. Rev. Lett.* **102** (2009) 207001.
- [10] T. Shibauchi, A. Carrington, and Y. Matsuda, *Annu. Rev. Condens. Matter Phys.* **5** (2014) null.

- [11] T. Shimojima, F. Sakaguchi, K. Ishizaka, Y. Ishida, T. Kiss, M. Okawa, T. Togashi, C.-T. Chen, S. Watanabe, M. Arita, K. Shimada, H. Namatame, M. Taniguchi, K. Ohgushi, S. Kasahara, T. Terashima, T. Shibauchi, Y. Matsuda, A. Chainani, and S. Shin, *Science* **332** (2011) 564.
- [12] D. S. Inosov, J. T. Park, P. Bourges, D. L. Sun, Y. Sidis, A. Schneidewind, K. Hradil, D. Haug, C. T. Lin, B. Keimer, and V. Hinkov, *Nat. Phys.* **6** (2010) 178.
- [13] S. Onari, H. Kontani, and M. Sato, *Phys. Rev. B* **81** (2010) 060504.
- [14] T. Hanaguri, S. Niitaka, K. Kuroki, and H. Takagi, *Science* **328** (2010) 474.
- [15] S. Onari and H. Kontani, *Phys. Rev. Lett.* **103** (2009) 177001.
- [16] J. Li, Y. F. Guo, S. B. Zhang, J. Yuan, Y. Tsujimoto, X. Wang, C. I. Sathish, Y. Sun, S. Yu, W. Yi, K. Yamaura, E. Takayama-Muromachiu, Y. Shirako, M. Akaogi, and H. Kontani, *Phys. Rev. B* **85** (2012) 214509.
- [17] F. Rullier-Albenque, H. Alloul, and R. Tourbot, *Phys. Rev. Lett.* **91** (2003) 047001.
- [18] Y. Nakajima, T. Taen, Y. Tsuchiya, T. Tamegai, H. Kitamura, and T. Murakami, *Phys. Rev. B* **82** (2010) 220504.
- [19] M. Tinkham, *Introuduction to superconductivity* (Dover, New York, 1966).
- [20] Y. Yeshurun, A. P. Malozemoff, and A. Shaulov, *Rev. Mod. Phys.* **68** (1996) 911.
- [21] G. Blatter, M. V. Feigel'man, V. B. Geshkenbein, A. I. Larkin, and V. M. Vinokur, *Rev. Mod. Phys.* **66** (1994) 1125.
- [22] L. Krusin-Elbaum, L. Civale, V. M. Vinokur, and F. Holtzberg, *Phys. Rev. Lett.* **69** (1992) 2280.
- [23] L. Civale, L. Krusin-Elbaum, J. R. Thompson, and F. Holtzberg, *Phys. Rev. B* **50** (1994) 7188.
- [24] B. Shen, P. Cheng, Z. Wang, L. Fang, C. Ren, L. Shan, and H.-H. Wen, *Phys. Rev. B* **81** (2010) 014503.

- [25] L. Krusin-Elbaum, L. Civale, J. R. Thompson, and C. Feild, Phys. Rev. B **53** (1996) 11744.
- [26] M. A. Avila, L. Civale, A. V. Silhanek, R. A. Ribeiro, O. F. d. Lima, and H. Lanza, Phys. Rev. B **64** (2001) 144502.
- [27] A. A. Zhukov, G. K. Perkins, Y. V. Bugoslavsky, and A. D. Caplin, Phys. Rev. B **56** (1997) 2809.
- [28] Y. Kamihara, T. Watanabe, M. Hirano, and H. Hosono, J. Am. Chem. Soc. **130** (2008) 3296.
- [29] Z. A. Ren, W. Lu, J. Yang, W. Yi, X. L. Shen, Z. C. Li, G. C. Che, X. L. Dong, L. L. Sun, F. Zhou, and Z. X. Zhao, Chin. Phys. Lett. **25** (2008) 2215.
- [30] M. Rotter, M. Tegel, and D. Johrendt, Phys. Rev. Lett. **101** (2008) 107006.
- [31] I. I. Mazin, D. J. Singh, M. D. Johannes, and M. H. Du, Phys. Rev. Lett. **101** (2008) 057003.
- [32] K. Kuroki, S. Onari, R. Arita, H. Usui, Y. Tanaka, H. Kontani, and H. Aoki, Phys. Rev. Lett. **101** (2008) 087004.
- [33] H. Kontani and S. Onari, Phys. Rev. Lett. **104** (2010) 157001.
- [34] Y. Nakajima, T. Taen, and T. Tamegai, J. Phys. Soc. Jpn. **78** (2009) 023702.
- [35] S. Chong, S. Hashimoto, and K. Kadowaki, Solid State Commun. **150** (2010) 1178 .
- [36] Y. Ma, Supercond. Sci. Technol. **25** (2012) 113001.
- [37] K. Hashimoto, M. Yamashita, S. Kasahara, Y. Senshu, N. Nakata, S. Tonegawa, K. Ikada, A. Serafin, A. Carrington, T. Terashima, H. Ikeda, T. Shibauchi, and Y. Matsuda, Phys. Rev. B **81** (2010) 220501.
- [38] K. Gofryk, A. S. Sefat, M. A. McGuire, B. C. Sales, D. Mandrus, J. D. Thompson, E. D. Bauer, and F. Ronning, Phys. Rev. B **81** (2010) 184518.
- [39] K. Gofryk, A. B. Vorontsov, I. Vekhter, A. S. Sefat, T. Imai, E. D. Bauer, J. D. Thompson, and F. Ronning, Phys. Rev. B **83** (2011) 064513.



- [40] G. Mu, H. Luo, Z. Wang, L. Shan, C. Ren, and H.-H. Wen, Phys. Rev. B **79** (2009) 174501.
- [41] M. Yamashita, Y. Senshu, T. Shibauchi, S. Kasahara, K. Hashimoto, D. Watanabe, H. Ikeda, T. Terashima, I. Vekhter, A. B. Vorontsov, and Y. Matsuda, Phys. Rev. B **84** (2011) 060507.
- [42] K. Okazaki, Y. Ota, Y. Kotani, W. Malaeb, Y. Ishida, T. Shimojima, T. Kiss, S. Watanabe, C.-T. Chen, K. Kihou, C. H. Lee, A. Iyo, H. Eisaki, T. Saito, H. Fukazawa, Y. Kohori, K. Hashimoto, T. Shibauchi, Y. Matsuda, H. Ikeda, H. Miyahara, R. Arita, A. Chainani, and S. Shin, Science **337** (2012) 1314.
- [43] Y. Mizukami, S. Kasahara, T. Shibauchi, and Y. Matsuda, unpublished .
- [44] H. F. Fong, P. Bourges, Y. Sidis, L. P. Regnault, A. Ivanov, G. D. Gu, N. Koshizuka, and B. Keimer, Nature **398** (1999) 588.
- [45] M. Ito, H. Harashina, Y. Yasui, M. Kanada, S. Iikubo, M. Sato, A. Kobayashi, and K. Kakurai, J. Phys. Soc. Jpn. **71** (2002) 265.
- [46] S. Iikubo, M. Ito, A. Kobayashi, M. Sato, and K. Kakurai, J. Phys. Soc. Jpn. **74** (2005) 275.
- [47] C. Stock, C. Broholm, J. Hudis, H. J. Kang, and C. Petrovic, Phys. Rev. Lett. **100** (2008) 087001.
- [48] N. K. Sato, N. Aso, K. Miyake, R. Shiina, P. Thalmeier, G. Varelogiannis, C. Geibel, F. Steglich, P. Fulde, and T. Komatsubara, Nature **410** (2001) 340.
- [49] H. F. Fong, B. Keimer, D. Reznik, D. L. Milius, and I. A. Aksay, Phys. Rev. B **54** (1996) 6708.
- [50] A. D. Christianson, E. A. Goremychkin, R. Osborn, S. Rosenkranz, M. D. Lumsden, C. D. Malliakas, I. S. Todorov, H. Claus, D. Y. Chung, M. G. Kanatzidis, R. I. Bewley, and T. Guidi, Nature **456** (2008) 930.
- [51] Y. Qiu, W. Bao, Y. Zhao, C. Broholm, V. Stanev, Z. Tesanovic, Y. C. Gasparovic, S. Chang, J. Hu, B. Qian, M. Fang, and Z. Mao, Phys. Rev. Lett. **103** (2009) 067008.

- [52] K. McElroy, R. W. Simmonds, J. E. Hoffman, D.-H. Lee, J. Orenstein, H. Eisaki, S. Uchida, and J. C. Davis, *Nature* **422** (2003) 592.
- [53] T. Hanaguri, Y. Kohsaka, M. Ono, M. Maltseva, P. Coleman, I. Yamada, M. Azuma, M. Takano, K. Ohishi, and H. Takagi, *Science* **323** (2009) 923.
- [54] Y. Yamakawa and H. Kontani, *BUSSEI KENKYU* **96** (2011) 579.
- [55] H. Kontani, Y. Inoue, T. Saito, Y. Yamakawa, and S. Onari, *Solid State Communications* **152** (2012) 718 . *Special Issue on Iron-based Superconductors*.
- [56] Y. Yamakawa, S. Onari, and H. Kontani, *Phys. Rev. B* **87** (2013) 195121.
- [57] M. Sato, Y. Kobayashi, S. C. Lee, H. Takahashi, E. Satomi, and Y. Miura, *J. Phys. Soc. Jpn.* **79** (2010) 014710.
- [58] J. Li, Y. Guo, S. Zhang, S. Yu, Y. Tsujimoto, H. Kontani, K. Yamaura, and E. Takayama-Muromachi, *Phys. Rev. B* **84** (2011) 020513.
- [59] F. Rullier-Albenque, P. A. Vieillefond, H. Alloul, A. W. Tyler, P. Lejay, and J. F. Marucco, *Europhys. Lett.* **50** (2000) 81.
- [60] F. Rullier-Albenque, H. Alloul, and R. Tourbot, *Phys. Rev. Lett.* **87** (2001) 157001.
- [61] F. Rullier-Albenque, H. Alloul, F. Balakirev, and C. Proust, *Europhys. Lett.* **81** (2008) 37008.
- [62] C. Tarantini, M. Putti, A. Gurevich, Y. Shen, R. K. Singh, J. M. Rowell, N. Newman, D. C. Larbalestier, P. Cheng, Y. Jia, and H.-H. Wen, *Phys. Rev. Lett.* **104** (2010) 087002.
- [63] C. P. Bean, *Phys. Rev. Lett.* **8** (1962) 250.
- [64] C. P. Bean, *Rev. Mod. Phys.* **36** (1964) 31.
- [65] M. V. Feigel'man, V. B. Geshkenbein, A. I. Larkin, and V. M. Vinokur, *Phys. Rev. Lett.* **63** (1989) 2303.
- [66] C. J. van der Beek, M. Konczykowski, A. Abal'oshev, I. Abal'osheva, P. Gierlowski, S. J. Lewandowski, M. V. Indenbom, and S. Barbanera, *Phys. Rev. B* **66** (2002) 024523.

- [67] C. J. van der Beek, G. Rizza, M. Konczykowski, P. Fertey, I. Monnet, T. Klein, R. Okazaki, M. Ishikado, H. Kito, A. Iyo, H. Eisaki, S. Shamoto, M. E. Tillman, S. L. Bud'ko, P. C. Canfield, T. Shibauchi, and Y. Matsuda, *Phys. Rev. B* **81** (2010) 174517.
- [68] R. Griessen, W. Hai-hu, A. J. J. van Dalen, B. Dam, J. Rector, H. G. Schnack, S. Libbrecht, E. Osquiguil, and Y. Bruynseraede, *Phys. Rev. Lett.* **72** (1994) 1910.
- [69] R. Prozorov, N. Ni, M. A. Tanatar, V. G. Kogan, R. T. Gordon, C. Martin, E. C. Blomberg, P. Prommapan, J. Q. Yan, S. L. Bud'ko, and P. C. Canfield, *Phys. Rev. B* **78** (2008) 224506.
- [70] S. Salem-Sugui, L. Ghivelder, A. D. Alvarenga, L. F. Cohen, K. A. Yates, K. Morrison, J. L. Pimentel, H. Luo, Z. Wang, and H.-H. Wen, *Phys. Rev. B* **82** (2010) 054513.
- [71] A. I. Larkin and Y. N. Ovchinnikov, *J. Low Temp. Phys.* **34** (1979) 409.
- [72] Q.-P. Ding, Y. Tsuchiya, S. Mohan, T. Taen, Y. Nakajima, and T. Tamegai, *Phys. Rev. B* **85** (2012) 104512.
- [73] M. P. Maley, J. O. Willis, H. Lessure, and M. E. McHenry, *Phys. Rev. B* **42** (1990) 2639.
- [74] Y. Abulafia, A. Shaulov, Y. Wolfus, R. Prozorov, L. Burlachkov, Y. Yeshurun, D. Majer, E. Zeldov, H. Wühl, V. B. Geshkenbein, and V. M. Vinokur, *Phys. Rev. Lett.* **77** (1996) 1596.
- [75] D. R. Nelson and V. M. Vinokur, *Phys. Rev. Lett.* **68** (1992) 2398.
- [76] D. R. Nelson and V. M. Vinokur, *Phys. Rev. B* **48** (1993) 13060.
- [77] A. A. Zhukov, G. K. Perkins, J. V. Thomas, A. D. Caplin, H. Küpfer, and T. Wolf, *Phys. Rev. B* **56** (1997) 3481.
- [78] Y. V. Bugoslavsky, A. A. Zhukov, G. K. Perkins, A. D. Caplin, H. Kojima, and I. Tanaka, *Phys. Rev. B* **56** (1997) 5610.
- [79] A. Silhanek, L. Civale, S. Candia, G. Nieva, G. Pasquini, and H. Lanza, *Phys. Rev. B* **59** (1999) 13620.

- [80] F. Steinmeyer, R. Kleiner, P. M 端 ller, H. M 端 ller, and K. Winzer, *Europhys. Lett.* **25** (1994) 459.
- [81] S. Koleśnik, T. Skośkiewicz, J. Igalson, and Z. Tarnawski, *Phys. Rev. B* **54** (1996) 13319.
- [82] W. K. Kwok, U. Welp, V. M. Vinokur, S. Fleshler, J. Downey, and G. W. Crabtree, *Phys. Rev. Lett.* **67** (1991) 390.
- [83] V. Ta Phuoc, E. Olive, R. De Sousa, A. Ruyter, L. Ammor, and J. C. Soret, *Phys. Rev. Lett.* **88** (2002) 187002.
- [84] L. Ammor, B. Pignon, N. H. Hong, and A. Ruyter, *Phys. Rev. B* **69** (2004) 224511.
- [85] K. Kihou, T. Saito, S. Ishida, M. Nakajima, Y. Tomioka, H. Fukazawa, Y. Kohori, T. Ito, S. ichi Uchida, A. Iyo, C.-H. Lee, and H. Eisaki, *J. Phys. Soc. Jpn.* **79** (2010) 124713.
- [86] J.-P. Reid, M. A. Tanatar, A. Juneau-Fecteau, R. T. Gordon, S. R. de Cotret, N. Doiron-Leyraud, T. Saito, H. Fukazawa, Y. Kohori, K. Kihou, C. H. Lee, A. Iyo, H. Eisaki, R. Prozorov, and L. Taillefer, *Phys. Rev. Lett.* **109** (2012) 087001.
- [87] J.-P. Reid, A. Juneau-Fecteau, R. T. Gordon, S. R. de Cotret, N. Doiron-Leyraud, X. G. Luo, H. Shakeripour, J. Chang, M. A. Tanatar, H. Kim, R. Prozorov, T. Saito, H. Fukazawa, Y. Kohori, K. Kihou, C. H. Lee, A. Iyo, H. Eisaki, B. Shen, H.-H. Wen, and L. Taillefer, *Supercond. Sci. Technol.* **25** (2012) 084013.
- [88] Y. Liu, M. A. Tanatar, V. G. Kogan, H. Kim, T. A. Lograsso, and R. Prozorov, *Phys. Rev. B* **87** (2013) 134513.
- [89] H. Luo, Z. Wang, H. Yang, P. Cheng, X. Zhu, and H.-H. Wen, *Supercond. Sci. Technol.* **21** (2008) 125014.
- [90] J. Ziegler, J. Biersack, and U. Littmark, *The Stopping and Range of Ions in Solids* (Pergamon Press, New York, 1985), p. 202.
- [91] D. X. Huang, Y. Sasaki, S. Okayasu, T. Aruga, K. Hojou, and Y. Ikuhara, *Phys. Rev. B* **57** (1998) 13907.
- [92] A. D. Marwick, G. J. Clark, D. S. Yee, R. B. Laibowitz, G. Coleman, and J. J. Cuomo, *Phys. Rev. B* **39** (1989) 9061.

- [93] N. Haberkorn, B. Maierov, I. O. Usov, M. Weigand, W. Hirata, S. Miyasaka, S. Tajima, N. Chikumoto, K. Tanabe, and L. Civale, *Phys. Rev. B* **85** (2012) 014522.
- [94] T. Goto, R. Kurihara, K. Araki, K. Mitsumoto, M. Akatsu, Y. Nemoto, S. Tatematsu, and M. Sato, *J. Phys. Soc. Jpn.* **80** (2011) 073702.
- [95] M. Yoshizawa, D. Kimura, T. Chiba, S. Simayi, Y. Nakanishi, K. Kihou, C.-H. Lee, A. Iyo, H. Eisaki, M. Nakajima, and S. ichi Uchida, *J. Phys. Soc. Jpn.* **81** (2012) 024604.
- [96] H. Alloul, J. Bobroff, M. Gabay, and P. J. Hirschfeld, *Rev. Mod. Phys.* **81** (2009) 45.
- [97] A. Kawabata, S. C. Lee, T. Moyoshi, Y. Kobayashi, and M. Sato, *J. Phys. Soc. Jpn.* **77** (2008) 103704.
- [98] A. E. Karkin, J. Werner, G. Behr, and B. N. Goshchitskii, *Phys. Rev. B* **80** (2009) 174512.
- [99] S. C. Lee, E. Satomi, Y. Kobayashi, and M. Sato, *J. Phys. Soc. Jpn.* **79** (2010) 023702.
- [100] K. Kirshenbaum, S. R. Saha, S. Ziemak, T. Drye, and J. Paglione, *Phys. Rev. B* **86** (2012) 140505.
- [101] K. Ohgushi and Y. Kiuchi, *Phys. Rev. B* **85** (2012) 064522.
- [102] L. Fang, Y. Jia, C. Chaparro, G. Sheet, H. Claus, M. A. Kirk, A. E. Koshelev, U. Welp, G. W. Crabtree, W. K. Kwok, S. Zhu, H. F. Hu, J. M. Zuo, H.-H. Wen, and B. Shen, *Appl. Phys. Lett.* **101** (2012) 012601.
- [103] H. Kontani and M. Sato, arXiv:1005.0942 (2010).
- [104] D. V. Evtushinsky, D. S. Inosov, V. B. Zabolotnyy, M. S. Viazovska, R. Khasanov, A. Amato, H.-H. Klauss, H. Luetkens, C. Niedermayer, G. L. Sun, V. Hinkov, C. T. Lin, A. Varykhalov, A. Koitzsch, M. Knupfer, B. B 端 chner, A. A. Kordyuk, and S. V. Borisenko, *New J. Phys.* **11** (2009) 055069.
- [105] H. Ding, K. Nakayama, P. Richard, S. Souma, T. Sato, T. Takahashi, M. Neupane, Y.-M. Xu, Z.-H. Pan, A. V. Fedorov, Z. Wang, X. Dai, Z. Fang, G. F. Chen, J. L. Luo, and N. L. Wang, *J. Phys.: Condens. Matter* **23** (2011) 135701.

- [106] G. Li, W. Z. Hu, J. Dong, Z. Li, P. Zheng, G. F. Chen, J. L. Luo, and N. L. Wang, Phys. Rev. Lett. **101** (2008) 107004.
- [107] B. Shen, H. Yang, Z.-S. Wang, F. Han, B. Zeng, L. Shan, C. Ren, and H.-H. Wen, Phys. Rev. B **84** (2011) 184512.
- [108] D. V. Evtushinsky, A. A. Kordyuk, V. B. Zabolotnyy, D. S. Inosov, T. K. Kim, B. Büchner, H. Luo, Z. Wang, H.-H. Wen, G. Sun, C. Lin, and S. V. Borisenko, J. Phys. Soc. Jpn. **80** (2011) 023710.
- [109] D. V. Efremov, M. M. Korshunov, O. V. Dolgov, A. A. Golubov, and P. J. Hirschfeld, Phys. Rev. B **84** (2011) 180512.
- [110] Y. Wang, A. Kreisel, P. J. Hirschfeld, and V. Mishra, Phys. Rev. B **87** (2013) 094504.
- [111] K. Nakamura, R. Arita, and H. Ikeda, Phys. Rev. B **83** (2011) 144512.
- [112] A. V. Chubukov, D. V. Efremov, and I. Eremin, Phys. Rev. B **78** (2008) 134512.
- [113] Y. Senga and H. Kontani, J. Phys. Soc. Jpn. **77** (2008) 113710.
- [114] Y. Bang, H.-Y. Choi, and H. Won, Phys. Rev. B **79** (2009) 054529.
- [115] Y. Senga and H. Kontani, New J. Phys. **11** (2009) 035005.
- [116] Z.-J. Yao, W.-Q. Chen, Y.-k. Li, G.-h. Cao, H.-M. Jiang, Q.-E. Wang, Z.-a. Xu, and F.-C. Zhang, Phys. Rev. B **86** (2012) 184515.
- [117] T. Terashima, N. Kurita, M. Kimata, M. Tomita, S. Tsuchiya, M. Imai, A. Sato, K. Kihou, C.-H. Lee, H. Kito, H. Eisaki, A. Iyo, T. Saito, H. Fukazawa, Y. Kohori, H. Harima, and S. Uji, Phys. Rev. B **87** (2013) 224512.
- [118] H. Ikeda, R. Arita, and J. Kuneš, Phys. Rev. B **82** (2010) 024508.
- [119] W. Malaeb, T. Shimojima, Y. Ishida, K. Okazaki, Y. Ota, K. Ohgushi, K. Kihou, T. Saito, C. H. Lee, S. Ishida, M. Nakajima, S. Uchida, H. Fukazawa, Y. Kohori, A. Iyo, H. Eisaki, C.-T. Chen, S. Watanabe, H. Ikeda, and S. Shin, Phys. Rev. B **86** (2012) 165117.

- [120] D. Watanabe, T. Yamashita, Y. Kawamoto, S. Kurata, Y. Mizukami, T. Ohta, S. Kasahara, M. Yamashita, T. Saito, H. Fukazawa, Y. Kohori, S. Ishida, K. Kihou, C. H. Lee, A. Iyo, H. Eisaki, A. B. Vorontsov, T. Shibauchi, and Y. Matsuda, arXiv: 1307.3408 (2013).
- [121] J. D. Weiss, C. Tarantini, J. Jiang, F. Kametani, A. A. Polyanskii, D. C. Larbalestier, and E. E. Hellstrom, *Nat. Mater.* **11** (2012) 682.
- [122] Q.-P. Ding, S. Mohan, Y. Tsuchiya, T. Taen, Y. Nakajima, and T. Tamegai, *Supercond. Sci. Technol.* **25** (2012) 025003.
- [123] Q.-P. Ding, T. Prombood, Y. Tsuchiya, Y. Nakajima, and T. Tamegai, *Supercond. Sci. Technol.* **25** (2012) 035019.
- [124] S. Pyon, T. Taen, F. Ohtake, Y. Tsuchiya, H. Inoue, H. Akiyama, H. Kajitani, N. Koizumi, S. Okayasu, and T. Tamegai, *Appl. Phys. Express* **6** (2013) 123101.
- [125] A. P. Malozemoff and M. P. A. Fisher, *Phys. Rev. B* **42** (1990) 6784.
- [126] L. Civale, *Supercond. Sci. Technol.* **10** (1997) A11.
- [127] T. Tamegai, T. Taen, H. Yagyuda, Y. Tsuchiya, S. Mohan, T. Taniguchi, Y. Nakajima, S. Okayasu, M. Sasase, H. Kitamura, T. Murakami, T. Kambara, and Y. Kanai, *Supercond. Sci. Technol.* **25** (2012) 084008.
- [128] A. S. Sefat, R. Jin, M. A. McGuire, B. C. Sales, D. J. Singh, and D. Mandrus, *Phys. Rev. Lett.* **101** (2008) 117004.
- [129] Y. Nakajima, Y. Tsuchiya, T. Taen, T. Tamegai, S. Okayasu, and M. Sasase, *Phys. Rev. B* **80** (2009) 012510.
- [130] N. Haberkorn, M. Miura, B. Maiorov, G. F. Chen, W. Yu, and L. Civale, *Phys. Rev. B* **84** (2011) 094522.
- [131] L. Miu and D. Miu, *Supercond. Sci. Technol.* **23** (2010) 025033.
- [132] H. G. Schnack, R. Griessen, J. G. Lensink, and W. Hai-Hu, *Phys. Rev. B* **48** (1993) 13178.
- [133] H.-H. Wen, H. Schnack, R. Griessen, B. Dam, and J. Rector, *Physica C* **241** (1995) 353 .

- [134] R. Prozorov, M. Tanatar, R. Gordon, C. Martin, H. Kim, V. Kogan, N. Ni, M. Tillman, S. Budko, and P. Canfield, *Physica C* **469** (2009) 582 .
- [135] S. Mohan, Y. Tsuchiya, Y. Nakajima, and T. Tamegai, *Phys. Rev. B* **84** (2011) 180504.
- [136] T. Taen, Y. Nakajima, T. Tamegai, and H. Kitamura, *Phys. Rev. B* **86** (2012) 094527.
- [137] Y. Yeshurun and A. P. Malozemoff, *Phys. Rev. Lett.* **60** (1988) 2202.
- [138] L. Civale, A. D. Marwick, M. W. McElfresh, T. K. Worthington, A. P. Malozemoff, F. H. Holtzberg, J. R. Thompson, and M. A. Kirk, *Phys. Rev. Lett.* **65** (1990) 1164.
- [139] C. J. van der Beek, M. Konczykowski, S. Kasahara, T. Terashima, R. Okazaki, T. Shibauchi, and Y. Matsuda, *Phys. Rev. Lett.* **105** (2010) 267002.
- [140] T. Tamegai, T. Taen, H. Yagyuda, Y. Nakajima, S. Okayasu, M. Sasase, H. Kitamura, T. Murakami, T. Kambara, and Y. Kanai, *Physica C: Superconductivity* **471** (2011) 777 .
- [141] T. Taen, Y. Tsuchiya, Y. Nakajima, and T. Tamegai, *Physica C* **470** (2010) 1106 .
- [142] Y. Sun, T. Taen, Y. Tsuchiya, S. Pyon, Z. Shi, and T. Tamegai, *Europhys. Lett.* **103** (2013) 57013.
- [143] M. Konczykowski, C. J. van der Beek, M. A. Tanatar, H. Luo, Z. Wang, B. Shen, H. H. Wen, and R. Prozorov, *Phys. Rev. B* **86** (2012) 024515.
- [144] V. K. Vlasko-Vlasov, U. Welp, G. W. Crabtree, D. Gunter, V. Kabanov, and V. I. Nikitenko, *Phys. Rev. B* **56** (1997) 5622.
- [145] T. Taen, Y. Nakajima, T. Tamegai, H. Kitamura, and T. Murakami, *Physica C* **471** (2011) 784 .
- [146] Y. N. Ovchinnikov and B. I. Ivlev, *Phys. Rev. B* **43** (1991) 8024.
- [147] H. Yang, H. Luo, Z. Wang, and H.-H. Wen, *Appl. Phys. Lett.* **93** (2008) 142506.
- [148] T. Taen, T. Otori, F. Ohtake, T. Tamegai, K. Kihou, S. Ishida, H. Eisaki, and H. Kitamura, *Physica C* **494** (2013) 106 .



- [149] S. Demirdiř, Y. Fasano, S. Kasahara, T. Terashima, T. Shibauchi, Y. Matsuda, M. Konczykowski, H. Pastoriza, and C. J. van der Beek, *Phys. Rev. B* **87** (2013) 094506.
- [150] C. J. van der Beek, S. Demirdiř, D. Colson, F. Rullier-Albenque, Y. Fasano, T. Shibauchi, Y. Matsuda, S. Kasahara, P. Gierlowski, and M. Konczykowski, *J. Phys.: Conf. Ser.* **449** (2013) 012023.
- [151] T. Taen, Y. Tsuchiya, Y. Nakajima, and T. Tamegai, *Phys. Rev. B* **80** (2009) 092502.
- [152] Y. Sun, T. Taen, Y. Tsuchiya, Q. Ding, S. Pyon, Z. Shi, and T. Tamegai, *Appl. Phys. Express* **6** (2013) 043101.
- [153] W. K. Kwok, L. M. Paulius, V. M. Vinokur, A. M. Petrean, R. M. Ronningen, and G. W. Crabtree, *Phys. Rev. Lett.* **80** (1998) 600.
- [154] L. Civale, L. Krusin-Elbaum, J. R. Thompson, R. Wheeler, A. D. Marwick, M. A. Kirk, Y. R. Sun, F. Holtzberg, and C. Feild, *Phys. Rev. B* **50** (1994) 4102.
- [155] L. Civale, A. D. Marwick, T. K. Worthington, M. A. Kirk, J. R. Thompson, L. Krusin-Elbaum, Y. Sun, J. R. Clem, and F. Holtzberg, *Phys. Rev. Lett.* **67** (1991) 648.
- [156] J. L. MacManus-Driscoll, S. R. Foltyn, Q. X. Jia, A. Wang, H. and Serquis, L. Civale, B. Maiorov, M. E. Hawley, M. P. Maley, and D. E. Peterson, *Nat. Mater.* **3** (2004) 439.
- [157] B. Maiorov, S. A. Baily, H. Zhou, O. Ugurlu, J. A. Kennison, P. C. Dowden, T. G. Holesinger, S. R. Foltyn, and L. Civale, *Nat. Mater.* **8** (2009) 398.
- [158] Y. Yamada, K. Takahashi, H. Kobayashi, M. Konishi, T. Watanabe, A. Ibi, T. Muroga, S. Miyata, T. Kato, T. Hirayama, and Y. Shiohara, *Appl. Phys. Lett.* **87** (2005) 132502.
- [159] A. Goyal, S. Kang, K. J. Leonard, P. M. Martin, A. A. Gapud, M. Varela, M. Paranthaman, A. O. Ijaduola, E. D. Specht, J. R. Thompson, D. K. Christen, S. J. Pennycook, and F. A. List, *Supercond. Sci. Technol.* **18** (2005) 1533.
- [160] B. Maiorov, T. Katase, I. O. Usov, M. Weigand, L. Civale, H. Hiramatsu, and H. Hosono, *Phys. Rev. B* **86** (2012) 094513.
- [161] H. Lei, D. Graf, R. Hu, H. Ryu, E. S. Choi, S. W. Tozer, and C. Petrovic, *Phys. Rev. B* **85** (2012) 094515.

- [162] S. Kasahara, T. Shibauchi, K. Hashimoto, K. Ikada, S. Tonegawa, R. Okazaki, H. Shishido, H. Ikeda, H. Takeya, K. Hirata, T. Terashima, and Y. Matsuda, *Phys. Rev. B* **81** (2010) 184519.
- [163] L. Lyard, P. Samuely, P. Szab<sup>†</sup>, C. Marcenat, T. Klein, K. H. P. Kim, C. U. Jung, H.-S. Lee, B. Kang, S. Choi, S.-I. Lee, L. Paulius, J. Marcus, S. Blanchard, A. G. M. Jansen, U. Welp, G. Karapetrov, and W. K. Kwok, *Supercond. Sci. Technol.* **16** (2003) 193.
- [164] F. Bouquet, Y. Wang, I. Sheikin, T. Plackowski, A. Junod, S. Lee, and S. Tajima, *Phys. Rev. Lett.* **89** (2002) 257001.
- [165] M. R. Eskildsen, M. Kugler, S. Tanaka, J. Jun, S. M. Kazakov, J. Karpinski, and O. Fischer, *Phys. Rev. Lett.* **89** (2002) 187003.
- [166] C. J. van der Beek, M. Konczykowski, and R. Prozorov, *Supercond. Sci. Technol.* **25** (2012) 084010.
- [167] S. Khim, B. Lee, J. W. Kim, E. S. Choi, G. R. Stewart, and K. H. Kim, *Phys. Rev. B* **84** (2011) 104502.
- [168] S. Yeninas, M. A. Tanatar, J. Murphy, C. P. Strehlow, O. E. Ayala-Valenzuela, R. D. McDonald, U. Welp, W. K. Kwok, T. Kobayashi, S. Miyasaka, S. Tajima, and R. Prozorov, *Phys. Rev. B* **87** (2013) 094503.
- [169] H. Yagyuda, Y. Nakajima, T. Tamegai, Y. Kanai, and T. Kambara, *Physica C* **471** (2011) 790 .
- [170] M. Oussena, P. A. J. de Groot, K. Deligiannis, A. V. Volkov, R. Gagnon, and L. Taillefer, *Phys. Rev. Lett.* **76** (1996) 2559.
- [171] A. A. Zhukov, H. K  pfer, P. A. J. de Groot, and T. Wolf, *Phys. Rev. Lett.* **83** (1999) 5110.
- [172] N. Kameda, T. Shibauchi, M. Tokunaga, S. Ooi, T. Tamegai, and M. Konczykowski, *Phys. Rev. B* **72** (2005) 064501.
- [173] B. Maierov, T. Katase, S. A. Baily, H. Hiramatsu, T. G. Holesinger, H. Hosono, and L. Civale, *Supercond. Sci. Technol.* **24** (2011) 055007.